Alma Mater Studiorum · Università di Bologna

School of Science
Department of Physics and Astronomy
Master Degree Programme in Astrophysics and Cosmology

Timing the Expansion of the Universe: Improving the Cosmic Chronometers method with Full Spectral Fitting

Graduation Thesis

Presented by:
Giulia Ruggeri

Supervisor:
Prof. Michele Ennio Maria Moresco

Co-supervisors:
Chiar.mo Prof. Andrea Cimatti
Dr.ssa Elena Tomasetti

Academic Year 2024-2025
Graduation date III

"Si sta aggrappati al tempo, questa è la verità.
Avvinghiati al tempo perché ci sia un ordine nell'elettrizzante disfatta quotidiana, un prima e un dopo ogni shock avvinghiati con feroce paura, e determinazione, con isterica pignoleria e disumana forza."

A. Baricco, *Castelli di rabbia*

Abstract

Modern cosmology has demonstrated that, to uncover the nature of the Universe and shed light on its dark components, it is essential to go beyond standard cosmological probes. This need has become even more pressing due to recent tensions in the measurements of cosmological parameters obtained through different observational techniques. Progress in the field, therefore, requires the development of independent and complementary methods capable of offering robust constraints on the expansion history of the Universe.

This thesis focuses on the cosmic chronometers (CC) method, an innovative technique designed to directly measure the Hubble parameter by estimating the differential age evolution of the most massive, passively evolving galaxies as a function of redshift. The primary goal is to establish a more robust and reliable framework for deriving differential ages using full spectral fitting (FSF), and to provide, for the first time, a comprehensive assessment of the systematic uncertainties affecting the FSF approach. The analysis is based on a carefully selected sample of CC from the SDSS BOSS survey in the redshift range $0.15 < z < 0.5$, exploiting both the high signal-to-noise ratio of the spectroscopic data and the available photometry. Extensive validation tests are performed to derive accurate and robust galaxy age estimates, which are then used to constrain the differential ages.

A key component of this work is the development of a modified version of the `Bagpipes` code, used for the FSF. This extended version introduces the possibility to vary the choice of stellar population synthesis models, initial mass functions, and stellar libraries, enabling a systematic exploration of model-dependent uncertainties. This analysis leads to a new, robust determination of the Hubble parameter:

$$H(z = 0.34) = 79.3^{+16.8}_{-13.0}\,(\text{stat} + \text{syst})\ \text{km}\,\text{s}^{-1}\,\text{Mpc}^{-1},$$

opening a new avenue for CC as a cosmological probe.

Contents

Nomenclature

BAO	Baryon Acoustic Oscillations
CC	Cosmic Chronometers
CDM	Cold Dark Matter
CMB	Cosmic Microwave Background
CSP	Composite Stellar Population
ETGs	Early-Type Galaxies
EW	Equivalent Width
FSF	Full Spectral Fitting
IMF	Initial Mass Function
MCMC	Markov Chain Monte Carlo
SDSS	Sloan Digital Sky Survey
SED	Spectral Energy Distribution
SFGs	Star-Forming Galaxies
SFH	Star Formation History
SFR	Star Formation Rate
SNIa	Type Ia Supernovae
SNR	Signal-to-Noise Ratio
SPS	Stellar Population Synthesis
SSP	Simple Stellar Population

Introduction

The Universe, along with the many questions it raises, has always been a central theme in human thought. Nowdays, understanding its nature and evolution lies at the heart of modern cosmology.

A century ago, Edwin Hubble's observations of extragalactic nebulae (Hubble, 1929) revealed that their recession velocities are proportional to their distances, expressed by the relation

$$v = H_0 \cdot d \, . \tag{1}$$

This discovery led to the revolutionary evidence that the Universe is expanding, with the proportionality constant H_0 (named the Hubble constant) representing the local rate of this expansion.

This empirical breakthrough provided the first major confirmation of the predictions of General Relativity when applied to a homogeneous and isotropic spacetime, marking the beginning of observational cosmology as a quantitative physical science. In the decades that followed, the cosmological model was shaped by the interplay between theoretical predictions and the ever-increasing precision of astronomical measurements.

A second major milestone came at the end of the 20th century with the discovery that cosmic expansion is not slowing down under the effect of gravity, as naively expected from a matter-dominated Universe, but is instead accelerating. This result, inferred from Type Ia supernova observations (Riess et al., 1998; Perlmutter et al., 1999), implied the existence of a previously unknown component of the Universe with negative pressure, now generically called *dark energy*. Alongside dark matter, required to explain galaxy rotation curves and gravitational clustering at large scales, dark energy reshaped our conception of cosmic energy content. Together, these two "dark" components dominate the cosmic energy budget, yet their fundamental nature remains one of the deepest mysteries in physics.

Following these findings, over the last three decades cosmology has rapidly evolved into a precision science. A wide range of observational probes has been developed and refined to test the dynamics, geometry, and composition of the Universe with increasing accuracy. These include primary and secondary anisotropies in the cosmic microwave background (CMB), galaxy clustering measurements, and Type Ia supernovae, among others. Thanks

to improved observational strategies, larger surveys, and advanced statistical techniques, many of these probes have achieved percent-level precision in constraining key cosmological parameters. Their success culminated in the so-called *concordance model* of cosmology, the Λ-Cold Dark Matter (ΛCDM) paradigm, which has proven remarkably effective in explaining a wide variety of cosmological observations, from the CMB to the large-scale structure of the Universe.

Despite its empirical success, ΛCDM is not a complete theory but rather an effective model. Its main components, dark energy (modeled as a cosmological constant Λ) and cold dark matter, lack a fundamental physical explanation. More importantly, the increasing precision of different cosmological probes over the last decade has revealed limitations of the standard model and highlighted internal tensions that cannot be ignored. A fundamental point that has emerged is that no single cosmological probe can fully and independently constrain all cosmological parameters, since each observable is sensitive to a particular set of components, and, at the same time, affected by different systematics. As a result, robust constraints rely on the combination of multiple, complementary probes to break degeneracies and provide cross-validation of results.

As observational precision continued to improve, a new issue has recently emerged. Some probes started showing significant discrepancies in their inferred values of key cosmological parameters. The most striking case is the so-called *Hubble tension* (Verde et al., 2019; Abdalla et al., 2022): local measurements of the Hubble constant using the distance ladder (Riess et al., 2019) consistently yield higher values of H_0 than those inferred by extrapolating early-Universe CMB-based measurement under the assumption of ΛCDM (Aghanim et al., 2020). The discrepancy currently exceeds the threshold for statistical compatibility and is widely regarded as one of the most significant challenges to the standard cosmological paradigm. This growing inconsistency has sparked an intense debate over whether it arises from unknown systematic errors in current data or instead points toward new physics beyond ΛCDM.

To address all these questions and make a step forward in our understanding of the Universe, it is crucial to go beyond the standard cosmological probes and develop and improve new methods to further understand the expansion of the Universe.

Scientific Problem. This thesis addresses the previously introduced questions by exploring and improving a novel cosmological probe, known as *Cosmic Chronometers* (CC, for a review see Moresco, 2024). This method, introduced at the beginning of the 2000s (Jimenez & Loeb, 2002), provides an innovative and independent path to derive cosmology-independent constraints on the expansion rate of the Universe through the analysis of the differential age evolution of massive and passively evolving galaxies, used as tracers of the cosmic evolution of the Universe. Different approaches have been proposed to derive robust differential ages for CC, each one

dealing differently with the well-known degeneracies between the stellar ages and other physical parameters of a galaxy.

One of the most promising avenues is full spectral fitting, which derives information on physical parameters (such as stellar age, metallicity, mass, and star formation history) by comparing observed spectroscopic and photometric information with theoretical models. However, a significant limitation of this approach is that the development of statistical tools to properly perform this analysis is rather recent, and it currently lacks the possibility of varying the ingredients in the theoretical stellar models to provide a robust assessment of the systematic effects involved in the method. It is therefore crucial to explore these uncertainties in greater depth to understand how they propagate into the derived values of $H(z)$. By addressing this issue at the intersection of cosmology and galaxy evolution, this work aims to enhance the robustness of the Cosmic Chronometers method and strengthen its role as a competitive tool for investigating the expansion of the Universe.

Methods. The analysis is based on high-quality spectroscopic data from the SDSS-III BOSS survey, which provides broad redshift coverage, high spectral resolution, and strong statistical power. The galaxy sample is refined step by step to select the most reliable passive systems, combining emission-line diagnostics, signal-to-noise cuts, and age-sensitive spectral indices. From this process, a sample of galaxies suitable for CC analysis is obtained and initially studied through classical spectral features, such as the D4000 break and Lick indices. The selection is then further refined to isolate a smaller subset of the best CCs, to which we apply full spectral fitting using the Bayesian code `Bagpipes` (Carnall et al., 2018). A key feature of the method is the removal of cosmological priors on galaxy ages. In addition, we implement a procedure that allows the variation of key components, such as the stellar population synthesis (SPS) model, stellar library, and IMF, in order to evaluate how the choice of stellar templates influences both the age estimates and the derived values of $H(z)$.

Objectives. The main objective of this thesis is to build a more reliable framework for the CC method by directly assessing and mitigating the impact of stellar population systematics when using a full spectral fitting approach. In this context, the work aims to: (i) define clear and reproducible criteria for selecting passive galaxies and provide a thorough characterization of these objects; (ii) obtain a new, independent measurement of $H(z)$ from the CC method using, for the first time, full spectral fitting on SDSS BOSS data, and perform a cosmological analysis with the resulting $H(z)$ to constrain cosmological parameters; (iii) test the sensitivity of the outcomes to different SPS models. Such measurements can contribute to the ongoing debate on the Hubble tension and underscore the value of Cosmic Chronometers as a com-

plementary cosmological probe.

Outline. We provide here below a brief overview of the chapters that structure this thesis:

- **Chapter 1** introduces the theoretical and astrophysical framework in which this thesis is placed. It begins with a review of the standard ΛCDM model, which successfully accounts for the majority of current observations and therefore represents the concordance cosmological scenario.
  Building on this foundation, the chapter then turns to galaxies, with particular attention to early-type systems, their stellar populations, and the tools employed to study them, such as SPS models and spectral indices. Finally, the Cosmic Chronometers method is introduced, together with the main criteria for selecting suitable galaxies, the techniques for measuring relative ages, and the systematic uncertainties that affect the robustness of this probe. Together, these elements provide the context and motivation for the analyses developed in the following chapters.

- **Chapter 2** describes the dataset used for this work and the procedure adopted to build a robust sample of galaxies for the cosmic chronometers analysis. The chapter begins with an overview of the SDSS-III BOSS spectroscopic survey, from which the parent galaxy sample was extracted. A detailed selection pipeline is then presented, aimed at identifying early-type galaxies with minimal contamination from outliers and with spectra of sufficiently high signal-to-noise ratio. The selection culminates in the definition and characterization of a *golden sample* of galaxies, whose quality and homogeneity are essential to ensure the reliability and success of the CC method.

- **Chapter 3** presents the main data analysis and results of this thesis. Building on the golden sample of galaxies, the analysis moves from index-based measurements to full spectral fitting using the code `Bagpipes`. The method is first validated on the golden sample to find the optimal configuration and then on an extended galaxy sample, yielding age estimates that are used to derive $H(z)$, with particular attention to binning effects. These measurements are then incorporated into a cosmological analysis to constrain fundamental parameters within the ΛCDM framework and to provide a direct comparison with previous BOSS studies using the CC approach.

- **Chapter 4** focuses on the evaluation and quantification of systematic uncertainties related to full spectral fitting. We explore this issue in depth by analyzing how variations in key modeling assumptions influence the results of full spectral fitting performed with the `Bagpipes` code.
  To this end, we developed modified versions of `Bagpipes` that incorporate alternative stellar population synthesis models based on the `FSPS` package (Conroy et al., 2009; Conroy & Gunn, 2010). The chapter presents a systematic comparison of the derived galaxy ages under different assumptions (models, IMF, stellar libraries) and evaluates the resulting impact on the measurement of $H(z)$. These results provide a quantitative assessment of systematic uncertainties, offering new insights into the reliability and robustness of the CC approach.

- **Chapter 5** summarizes the work presented in this thesis, highlighting the main results and conclusions. It also discusses potential future developments and perspectives, outlining possible directions for further research, building on the findings of this study.

Chapter 1

Galaxies in the Cosmological context

The present work develops in a context where it is possible to appreciate the deep connection that exists between the study of galaxy formation and evolution and cosmology. In this Chapter, we present an overview of the so-called ΛCDM cosmological model, currently able to justify the vast majority of observations at the largest scales, making it the most accepted by the astronomical community nowdays. In addition to this, we also describe the main models of galaxy formation, followed by a presentation of the CC method, which is employed in this thesis to provide a new estimate of the expansion rate of the Universe.

1.1 Cosmological framework

The ΛCDM model is based on two fundamental pillars. The first is the cosmological principle, which states that, on sufficiently large scales, the Universe is homogeneous and isotropic, meaning that it has a uniform composition and appearance in all directions. This assumption can be tested, for instance, by examining the large-scale distribution of galaxies or by mapping the temperature anisotropies of the CMB. The second pillar is the theory of gravity, described by General Relativity.
Building on these assumptions, we can proceed to describe the Universe from a cosmological perspective, presenting the main principles and the fundamental relations that govern its evolution.

1.1.1 Cosmological distances

At the basis of General Relativity, there is the idea that space and time are linked by a common metric. In this case, distances in space-time are defined by adopting the so called Friedmann-Lemaître-Robertson-Walker metric (FLRW), which means assuming

homogeneity and isotropy:

$$\mathrm{d}s^2 = -c^2\mathrm{d}t^2 + a^2(t)\left[\frac{\mathrm{d}r^2}{1-kr^2} + r^2(\mathrm{d}\theta^2 + sin^2(\theta)\mathrm{d}\phi^2)\right] . \tag{1.1}$$

The quantities (r, θ, ϕ) represent a system of polar comoving coordinates, c is the speed of light, a is the scale factor, and k refers to the geometry of the Universe: flat if $k = 0$, spherical if $k = 1$, hyperbolic if $k = -1$. The scale factor a relates physical coordinates (R) to comoving coordinates (r) as $R(t) = a(t)r$.

Starting from the FLRW metric, it is possible to define the distance between two objects located at different points of space-time. In particular, *proper distance* is defined as the one measured at the same instant ($dt = 0$). Without losing generality, we can choose $\mathrm{d}t = \mathrm{d}\theta = \mathrm{d}\phi = 0$ and the proper distance is given by

$$d_{PR} = \int_0^r \frac{a(t)dr'}{\sqrt{1-Kr'^2}} = a(t)F(r), \qquad F(r) = \int_0^r \frac{dr'}{\sqrt{1-Kr'^2}}, \tag{1.2}$$

where $a(t)$ does not depend on r, but since it is a time-dependent quantity, this distance will vary with the passage of cosmic time.
In addition, in cosmology it is usually defined as *comoving distance* the proper distance computed at the present time (t_0):

$$d_C = a(t_0)F(r) = \frac{a(t_0)}{a(t)}d_{PR}. \tag{1.3}$$

From this point on, each quantity computed at t_0 will be indicated with a subscript zero. Moreover, the concept of *luminosity distance*, d_L, is frequently encountered. It is defined as the distance at which a source with luminosity L produces an observed flux $f = L/(4\pi d_L^2)$.

1.1.2 Cosmological Redshift

When we consider a homogeneous and isotropic Universe, a fundamental quantity is the cosmological redshift. The redshift, z, quantifies the difference between the wavelength, λ_{em}, of a photon emitted from a distant source and the wavelength, λ_0, received today by an observer: $z \equiv (\lambda_0 - \lambda_{em})/\lambda_{em}$. In a cosmological context, this difference depends on the expansion of the Universe. Assuming the usual convention in cosmology that the scale factor at the present time is normalized to unity, $a(t_0) = 1$, we can write:

$$1 + z = \frac{\lambda_0}{\lambda_{em}} = \frac{1}{a(t_{em})}. \tag{1.4}$$

Then, we can think of the redshift as the measure of how much the scale factor varied from the time at which the photon was emitted. Therefore, the cosmological redshift of a distant galaxy can be determined by measuring, in its observed spectrum, the wavelengths of emission or absorption lines of known restframe wavelengths. Galaxies with a higher cosmological redshift are more distant and have emitted the photons that we observe today a longer time ago.

Having introduced the concept of redshift, we note that in a spatially flat Universe the luminosity distance is simply given by

$$d_L(z) = (1+z)\, x, \tag{1.5}$$

where $x = x(z)$ denotes the comoving distance to the source. Assuming to know the intrinsic size l of an extended cosmological source at redshift z and to measure an angular size θ for this source, we define the *angular diameter distance* d_A such that $\theta = l/d_A$. It can be shown that d_A and d_L are related by:

$$d_A = \frac{d_L}{(1+z)^2}\ , \tag{1.6}$$

so for a spatially flat Universe

$$d_A = \frac{x}{1+z}\ . \tag{1.7}$$

This relation, known as *duality relation*, is fundamental since it contains the assumption of the FLRW metric.

1.1.3 Hubble law

The proper distance between two separated objects is a quantity that changes with time, so by deriving it, we can compute at which relative velocity v_R they are approaching or receding from each other.

$$v_R = \frac{\mathrm{d}}{\mathrm{d}t} d_{PR} = \frac{\mathrm{d}}{\mathrm{d}t}[a(t)F(r)] = \dot{a}(t)F(r). \tag{1.8}$$

From Eq. (1.2) we obtain $F(r) = d_{PR}/a(t)$, and the previous relation becomes:

$$v_R = \frac{\dot{a}(t)}{a(t)} d_{PR} = H(t) d_{PR}, \tag{1.9}$$

where $H(t) \equiv \dot{a}/a$ is the *Hubble parameter*, historically measured in km s^{-1}Mpc^{-1}. The value of this parameter at the present time, $H_0 \equiv H(t_0)$, is known as the *Hubble constant*. The reciprocal of the Hubble constant, $t_H = H_0^{-1}$, is the *Hubble time*, an estimate of the present-day age of the Universe, whose exact value depends on the cosmological model.

Eq. (1.9) evaluated at the present time is the *Hubble-Lemaître law* (Lemaître, 1927; Hubble, 1929), originally discovered using measurements of distances and velocities of relatively nearby galaxies.

The Hubble constant is empirically found to be positive, which means that, on sufficiently large scales, galaxies are receding from each other at speeds proportional to their separations. This recession trend, known as the *Hubble flow*, can be interpreted as a signature of the fact that the Universe is currently expanding. In other words, galaxies follow the Hubble flow because they are dragged along as the space expands. The fact that, in some cases, neighboring galaxies are approaching each other is related to peculiar velocities due to local dynamics and not to the cosmological expansion. The value of the Hubble constant is, nowadays, very debated since measurements obtained using different probes give different results. A reference value commonly adopted is $H_0 = 70$ km s^{-1} Mpc^{-1}. Often, in literature, it is found in the form $h \equiv H_0/100$ km s^{-1} Mpc^{-1}.

To conclude the outline on the kinematics related to the FLRW metric, we can introduce the *deceleration parameter*, which quantifies the time variation of the expansion rate of the Universe:

$$q(t) \equiv -\frac{\ddot{a}a}{\dot{a}^2} \,. \tag{1.10}$$

It is an adimensional quantity, defined to be negative since historically the model seemed to support the idea that the Universe was expanding in a decelerated way. As mentioned before, since the 2000s, the idea of the accelerated expansion has become stronger, and it is still one of the biggest issues of modern cosmology.

1.1.4 Friedmann Equations

For a given cosmological model and in the context of general relativity, the expansion of the Universe can be described by the function $a(t)$. We model the Universe as a perfect fluid, generally treated as a mixture of several components, characterized by different properties. These assumptions, together with the consideration that the Universe is homogeneous and isotropic, lead to two equations, computed by Friedmann for the first time and then labeled as the Friedmann equations (Friedmann, 1922):

$$\left(\frac{\dot{a}}{a}\right)^2 + \frac{kc^2}{a^2} = \frac{8\pi G}{3}\rho; \tag{1.11}$$

$$\frac{\ddot{a}}{a} = -\frac{4\pi G}{3}\left(\rho + \frac{3p}{c^2}\right); \tag{1.12}$$

They are complemented by a third equation, which can be derived assuming the Universe as a closed system in adiabatic equilibrium:

$$\mathrm{d}(\rho c^2 a^3) = -p\mathrm{d}a^3 \tag{1.13}$$

Deriving Eq. (1.12) as a function of time and setting $c = 1$, we obtain:

$$\dot{\rho} + 3\frac{\dot{a}}{a}(\rho + p) = 0. \tag{1.14}$$

It is known as *fluid equation* and describes how the pressure and density are related in an expanding Universe. When $k = 0$ (spatially flat Universe), the Friedmann equation, Eq. (1.11), becomes:

$$H^2 = \frac{8\pi G\rho}{3} \ . \tag{1.15}$$

It follows that the Universe is spatially flat when $\rho = \rho_{crit}$, where:

$$\rho_{crit}(t) = \frac{3H^2(t)}{8\pi G} \tag{1.16}$$

is the *critical density of the Universe*. It is also useful to define the dimensionless *density parameter*

$$\Omega(t) \equiv \frac{\rho(t)}{\rho_{crit}(t)}. \tag{1.17}$$

So, in terms of the density parameter, the first Friedmann equation (1.11) can be written as:

$$H^2(1 - \Omega)a^2 = -kc^2 \ , \tag{1.18}$$

which means $H_0^2(1 - \Omega_0) = -kc^2$, at the present time. Therefore, the present-day value of the density parameter Ω_0 determines the sign of k (and then the spatial geometry of the Universe) at all times.

1.1.5 A multi-component Universe

We know that in the Universe different components coexist. For a given component of the cosmic fluid, the relation between p and ρ is provided by the *cosmological equation of state*:

$$p = w\rho c^2 \ . \tag{1.19}$$

The value of the dimensionless parameter w is different for each component. Combining the equation of state (1.19) with the fluid equation (1.14), it is possible to obtain the

equation for the evolution of the density ρ with redshift:

$$\rho = \rho_0 \; exp\left\{3\int_0^z [1+w(z')]\mathrm{d}\ln(1+z')\right\} \; . \tag{1.20}$$

When w is a constant, the above equation reduces to:

$$\rho = \rho_0(1+z)^{3(1+w)} = \rho_0 a^{-3(1+w)} \; . \tag{1.21}$$

A fundamental distinction must be drawn between relativistic and non-relativistic components. For a non-relativistic component $p \ll \rho c^2$, this is the case of ordinary baryonic matter and non-baryonic cold dark matter. So, for what is commonly referred to as *matter*, it can be effectively assumed that $w = 0$, so $p = 0$ and

$$\rho_m = \rho_{m,0}(1+z)^3 \; . \tag{1.22}$$

The relativistic components are labelled as *radiation*. Among them, photons and neutrinos (at sufficiently high redshift) are included, for which $w = 1/3$, so

$$\rho_{rad} = \rho_{rad,0}(1+z)^4. \tag{1.23}$$

Another constituent of the Universe is the so-called *dark energy*, which is needed to justify the accelerated expansion ($\ddot{a}$) that we observe. It is evident from Eq. (1.11) and (1.18) that, to be classified as dark energy, a component must have $w < -1/3$. A special case of dark energy is the energy associated with the vacuum, characterized by constant $w = -1$. The cosmological constant Λ, first introduced by Einstein to cover the problem of a non-static Universe, now plays the role of this vacuum energy. The corresponding density is, then, given by:

$$\rho_\Lambda = \rho_{\Lambda,0} = const \; . \tag{1.24}$$

For all the components described so far, we define the corresponding density parameters $\Omega_m \equiv \rho_m/\rho_{crit}$, $\Omega_{rad} \equiv \rho_{rad}/\rho_{crit}$ and $\Omega_\Lambda = \rho_\Lambda/\rho_{crit}$, which are all time-dependent, except ρ_Λ which is assumed to be constant.
The behaviour of the different constituents as a function of cosmic time, together with the evidence that we have from the observations of the present Universe, allows us to derive the evolution of the density parameters: Ω_r, Ω_m, Ω_Λ.

1.1.6 Standard Cosmological Model

The currently favoured cosmological model is known as the *standard* or *concordance* model. According to this scenario, the cosmic fluid consists of three components: matter, radiation, and dark energy (Λ), introduced in the previous Section. To explain structure

formation, most of the matter present in the Universe must be in the form of *cold dark matter* (CDM). The picture of the present Universe seems to suggest that CDM and dark energy are largely dominant, representing roughly the 25% and the 70% of the total mass-energy balance of the Universe, respectively. Therefore, this model is often referred to with the acronym ΛCDM.

Cosmological parameters can be measured from different sets of observations, including the analysis and modelling of the CMB, observations of distant supernovae, measurements of the mass of galaxy clusters, weak gravitational lensing, and the galaxy large-scale structure. All these different cosmological probes seem to agree on the fact that in the local Universe, the density parameter Ω_0 has a value close to unity. The Planck collaboration (Aghanim et al., 2020) found $\Omega_0 = 0.999 \pm 0.002$. From what was discussed above, this means that the present-day total density $\rho_0 = \rho_{m,0} + \rho_{rad,0} + \rho_{\Lambda,0}$ is indistinguishable from the critical density, and consequently that the geometry of the space-time is constrained to be flat ($k = 0$). For this reason, it is common to denote the model as $f\Lambda CDM$, where the f stands for $flat$. Starting from these considerations, it is possible to simplify the equations presented in the previous Section. In particular, for a flat Universe we found an expression for H^2 given by Eq. (1.15), which can be rewritten as a function of redshift and separating the contributions of the different components, given by Eq. (1.21). Finally, reminding the definitions for the critical density and for the density parameters shown in Eqs. (1.16) and (1.17), the evolution of the Hubble parameter $H(z)$ is given by

$$H(z) = H_0 \sqrt{\Omega_{\Lambda,0} + \Omega_{m,0}(1+z)^3 + \Omega_{r,0}(1+z)^4} \tag{1.25}$$

From these considerations, assuming a homogeneous Universe, isotropic, spatially flat ($\Omega = 1$ at all times), and characterized by a dark energy with ($w = -1$), we can derive the present-day density parameters as: $\Omega_{m,0} = \rho_{m,0}/\rho_{crit,0} \approx 0.315 \pm 0.007$ (from Aghanim et al., 2020), $\Omega_{\Lambda,0} = \rho_{\Lambda,0}/\rho_{crit,0} = 1 - \Omega_{m,0}$ and $\Omega_{rad,0} = \rho_{rad,0}/\rho_{crit,0} \approx 9 \times 10^{-5}$. These values are usually indicated as *standard cosmological parameters*.

Hubble tension. So far, we described the $f\Lambda$CDM model as the one that best justifies the vast majority of the phenomena observed in our Universe [1]. Despite that, there are still some open issues to be solved, suggesting to further explore the nature of the Universe and leaving room for possible alternative models. As briefly mentioned before, currently, one of the main problems, also directly related to the purpose of this work, is what is currently knows as the *Hubble tension* (Verde et al., 2019). Specifically, independent measurements of the Hubble constant computed with different methods produce results that are discrepant on the order of $4 - 5\sigma$. This mismatch is particularly evident when

[1] see the latest results by DESI (Adame et al., 2025), that seem to indicate a time-evolving dark energy equation of state.

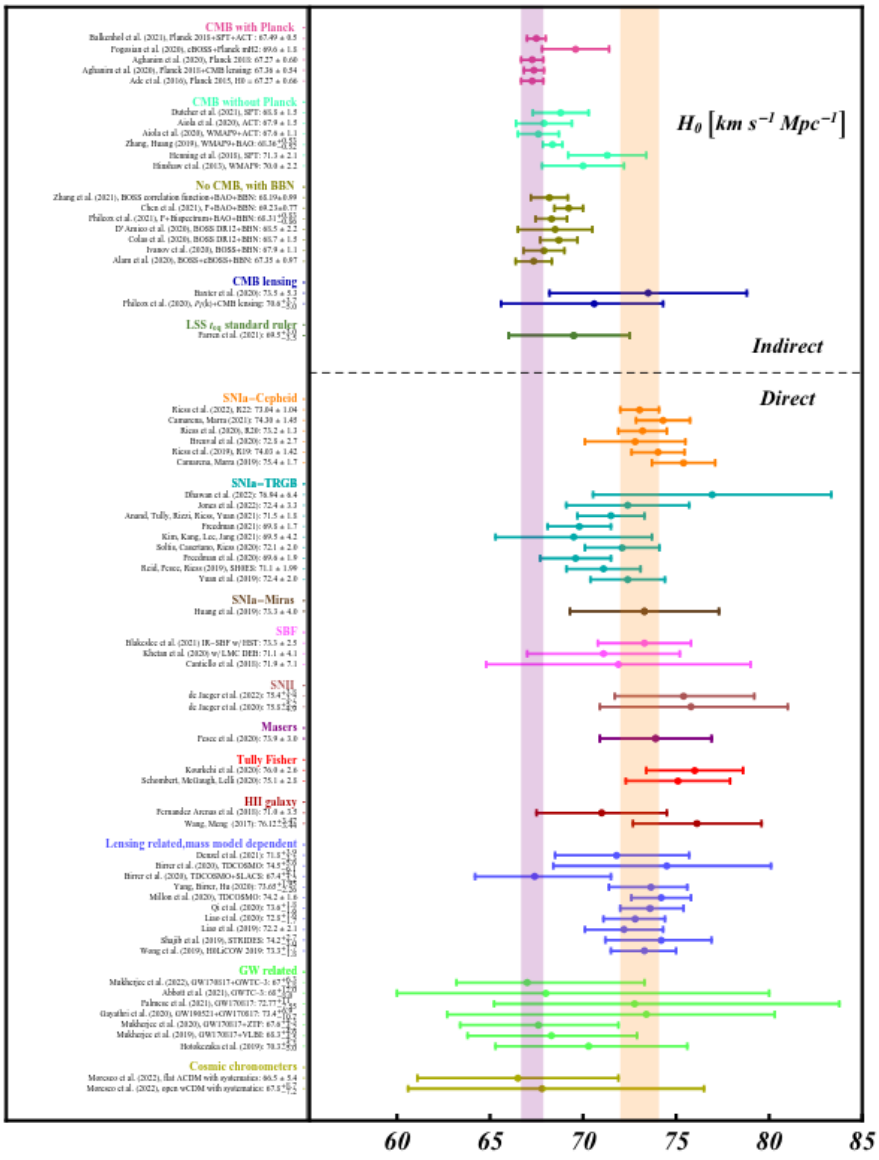

Figure 1.1: Measurements of H_0 obtained from different cosmological probes. *Early* type probes are shown at the top, while *late* type probes are shown at the bottom. (from Abdalla et al., 2022).

comparing the estimates of H_0 for the *early* Universe with those computed for the *late* times. Indeed, the observations of the CMB carried out by the Planck Collaboration (Aghanim et al., 2020) produce

$$H_0 = 67.44 \pm 0.58 \ \ \text{km s}^{-1}\ \text{Mpc}^{-1}, \tag{1.26}$$

while estimates resulting from using Supernovae Ia as standard candles and calibrated

using Cepheids in the Large Magellanic Cloud (Riess et al., 2019) give

$$H_0 = 74.03 \pm 1.42 \ \ \mathrm{km\ s^{-1}\ Mpc^{-1}}. \tag{1.27}$$

A few years ago, this discrepancy was still compatible with the uncertainties associated with the measurements, but now, each of these methods has reached an accuracy of the order of percent or sub-percent, and the difference remains around 6 km s^{-1} Mpc^{-1}, of the order of 4–5 σ. The existence of this tension provides powerful hints that something may be missing from the current best model of the cosmos, suggesting, perhaps, the need for a "missing" new physics (see, e.g., Verde et al., 2019; Abdalla et al., 2022)

Before engaging in speculations, the exploration of new independent probes is fundamental to better understand the nature of the problem. Fig. 1.1 presents a summary of the cosmological probes studied to date. One possibility is the study of the so-called *Cosmic Chronometers*, which will be discussed in detail in the following sections. This method, based on the analysis of massive and passive galaxies, appears very promising.

1.2 Galaxies: the current picture

Once the cosmological framework has been established, we can focus on present-day galaxies, representing the endpoints that enclose crucial information on how baryonic and dark matter evolved as a function of cosmic time. From this point of view, galaxies are also useful to test the ΛCDM cosmology. For instance, a key role is played by the methods that try to estimate the current ages of the oldest stars in galaxies, providing an observational lower limit the age of the Universe itself.

Since the discovery of the first galaxy, or *nebula*, in the mid-1970s, much progress has been made, so that today we know that galaxies display a variety of properties and span a very broad range of luminosities, sizes, and masses. The first systematic study dates back to 1926, when E. Hubble suggested a classification of galaxies based on their morphology: ellipticals and lenticulars (*early-type*), spirals and irregulars (*late-type*). With time, this classification remained valid, even revealing much deeper foundations, since it could be extended to other important physical properties such as the color and the star formation rate. In this Section, we describe what in literature is referred to as *early-type* galaxies in *passive evolution* and how these are distinguished and selected, since they represent the object of study of this work.

1.2.1 Properties of the early-type galaxies

Early-type galaxies (ETGs) are among the most massive, red, and old galaxies in the Universe, and have been historically classified as those with an elliptical shape. Despite

the term *passive* denotes the fact that these systems are, in general, not forming stars anymore, it is worth to underline that many studies have demonstrated that selecting elliptical galaxies does not guarantee that they are also red, nor that they are passive (Moresco et al., 2013), meaning that these properies are not perfectly associated.

To understand the true nature of the observed objects, it is necessary to consider a combination of different aspects, including their photometric, morphological and evolutionary properties, in order to extract as much information as possible. The challenge is that, clearly, having all this data available is not trivial.

Surface Brightness Profile

The shape and morphology of galaxies can be described through a more quantitative approach by looking at how the surface brightness, I_Λ, varies as a function of the radial distance from the galaxy centre. The curves connecting points of equal surface brightness are called *isophotes*, fundamental to understanding the distribution of the luminosity within the galaxy and to try to constrain its dimensions. For elliptical galaxies, these curves are approximated by ellipses and their flattening is related to the *ellipticity* $\epsilon \equiv (a-b)/a$, where a and b are the observed semi-major and semi-minor axes. To avoid misunderstandings it became crucial to introduce a quantity, known as *effective radius* R_e, which represents the radius of the isophote containing 50% of the total flux.

The luminosity profile of elliptical galaxies was first characterized in the seminal work by Gérard and Antoinette de Vaucouleurs in 1948. Analyzing a sample of galaxies of this type, they noticed that observing the brightness profile as a function of radius, the trend was always the same for each object of the sample. This resulted in the conclusion that independently of shape and dimensions, every galaxy classified as elliptical always appears in the same way, and follows what is known as the de Vaucouleurs profile, which was afterwards generalized for all types of galaxies by the *Sèrsic profile* (Sersic, 1968):

$$I_\Lambda(R) = I_{\Lambda,e} \exp\left\{-b(n)\left[\left(\frac{R}{R_e}\right)^{\frac{1}{n}} - 1\right]\right\}, \tag{1.28}$$

where $I_{\lambda,e}$ is the surface brightness at a given wavelength λ at the effective radius R_e, n is the *Sèrsic index*, and b is a quantity well approximated by $b(n) = 2n - 1/3 + 4/(405n)$.

Galaxies show a broad distribution of Sèrsic index n with a dependence on the different types of galaxies, which reflects intrinsic differences in the internal distribution of luminous matter. Usually, $n \approx 2.5$ is taken as the value separating early-type galaxies from those with later morphological types.

The surface brightness profile can also be used to quantify the size of a galaxy within a given limiting threshold of surface brightness. However, it is also customary to use the effective radius R_e to indicate galaxy size. In general, the galaxy size increases with

luminosity and stellar mass (M_*) as $R_e \propto M_*^{\alpha}$, where typically $\alpha \approx 0.4$ for Star Forming galaxies (SFGs). In the case of ETGs, the relation is steeper ($\alpha \approx 0.5 - 0.6$).

Spectral Energy Distributions

The spectral energy distribution (SED) of a galaxy represents a measure of its flux density across the electromagnetic spectrum, and it is one of the most powerful tools we have for understanding the Universe beyond our own galaxy. A galaxy's SED encodes information about both its current physical state and past star formation activity, and contains contributions from various sources. Understanding these components and their contributions across different parts of the electromagnetic spectrum is crucial for interpreting galaxy SEDs and extracting meaningful physical properties. A more extended discussion is available in the review by Iyer et al. (2025).

The primary elements that make up a galaxy SED are: the stellar continuum, the dust attenuation and re-emission, and the emission from diffuse matter.

The *gas content* of galaxies, both atomic and molecular, contributes to their SEDs through several processes depending on their temperature, density, and ionization. At $T < 1000$ K, vibrational and rotational lines are emitted from molecules in the infrared to millimeter spectral range. Neutral atomic hydrogen with temperatures between tens to 8000 K is responsible for the line emission at 21 cm in the radio. Warm (T $\sim 10^4$ K) gas photoionized by massive stars (HII regions) emits strong recombination lines in the optical-UV. In addition, HII regions also emit bremsstrahlung continuum in the radio. Hot (T $\sim 10^{6-7}$ K) gas, produced by shock in supernova remnants, emits bremsstrahlung continuum in X-rays and highly ionized lines in the X-ray to optical.

Interstellar dust consists of solid particles (or grains), typically ranging in size from 5 to 250 nm, diffused in the ISM by stellar winds or explosions which form in the atmospheres of evolved stars. Dust affects the SED of galaxies primarily in two ways: by attenuating the light at UV-to-NIR wavelengths and by re-emitting light as a so-called gray-body continuum in the far infrared (FIR). Dust emission is stronger in SFGs, but a contribution can also be present in ETGs due to the grains produced by mass loss in evolving red giant stars.

The *stellar continuum* is the combined emission from the galaxy's stellar populations, covering from the UV to the NIR of the electromagnetic spectrum; its shape depends on the properties of these stars, particularly their age and metallicity. Stellar population synthesis models, described in the next Section, can be used to generate the spectrum of a Simple Stellar Population (SSP); when weighted by the star formation history (SFH), which describes the star formation rate at a given age, these models can be used to predict the composite stellar continuum of an entire galaxy.

1.2.2 Stellar Population Synthesis models

The first step in modeling the stellar continuum is to get the spectrum of a population of stars at a single epoch or age, referred to as a simple stellar population. The monochromatic flux of an SSP with metallicity Z is given by the following integral:

$$F_{\lambda,SSP}(t,Z) = \int_{m_1}^{m_2} F_{\lambda,star}(m,t,Z)\phi(m)\mathrm{d}m, \tag{1.29}$$

where m_1 and m_2 are the masses of the lowest- and highest-mass star in the SSP, $F_{\lambda,star}(m,t,Z)$ is the monochromatic flux of a single star, and $\phi(m)$ is the IMF. These models are based on the adoption of the following main ingredients:

- *Isochrones.* Defined as the tracks in the Hertzsprung-Russell (HR) diagram of a stellar population with common age and metallicity, they allow us to describe the evolution of an SSP. In literature, several isochrone libraries are available, fully sampling the different combinations of ages, metallicities, and evolutionary phases. Possible choices of stellar isochrone models include `PARSEC` (Bressan et al., 2012), `MIST` (Choi et al., 2016), `BaSTI` (Pietrinferni et al., 2009), `Padova isochrones` (Girardi et al., 2000).

- *Library of stellar spectra.* They are collections of stellar spectra, either observational or synthetic, covering a wide range of effective temperatures, surface gravities, and metallicities. They are essential for constructing the integrated spectrum of a stellar population by combining the spectra of individual stars. Some libraries are based entirely on theoretical stellar spectra. Examples of stellar libraries are `MILES` (Sanchez-Blazquez et al., 2006; Falcón-Barroso et al., 2011a), `STELIB` (Le Borgne et al., 2003), `BaSeL` (Lejeune et al., 1998; Westera et al., 2002).

- *Initial mass function.* It describes the distribution of stellar masses for a newly formed stellar population. Since this is not known beyond the Milky Way, it is always necessary to adopt an IMF and a range of stellar masses. Common choices for the IMF are Salpeter (Salpeter, 1955), Chabrier (Chabrier, 2003), and Kroupa (Kroupa, 2001).

Beyond the uncertainties affecting each of these elements, it is important to recall that SSPs are simplistic approximations of real galaxies that form during an extended time interval. A collection of stars formed at different times and with different initial chemical compositions is known as a composite stellar population (CSP), and it is often computed as the sum of individual SSPs weighted by the star formation history, which needs to be assumed. A clear picture of the different ingredients needed to build these spectral models is provided in Fig. 1.2.

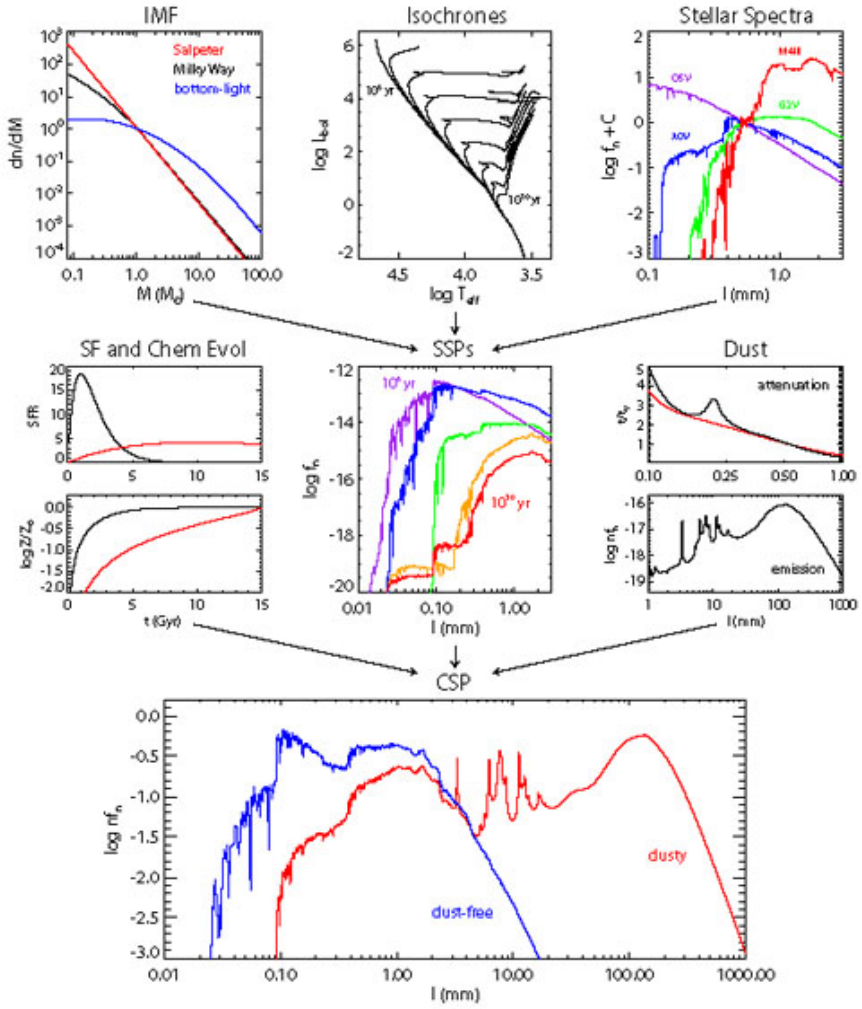

Figure 1.2: Overview of the stellar population synthesis technique. The upper panels highlight the ingredients necessary for constructing simple stellar populations (SSPs): an IMF, isochrones for a range of ages and metallicities, and stellar spectra spanning a range of T_{eff}, L_{bol}, and metallicity. The middle panels highlight the ingredients necessary for constructing Composite Stellar Populations (CSPs): star formation histories and chemical evolution, SSPs, and a model for dust attenuation and emission. The bottom row shows the final CSPs both before and after a dust model is applied. (from Conroy, 2013)

SPS models combine information from isochrones, stellar libraries, and the IMF to simulate the integrated light of a stellar population (such as a galaxy or a star cluster). Among the SPS models available in the literature are `BC03` (Bruzual & Charlot, 2003) and `FSPS` (Conroy et al., 2009), `M11` (Maraston & Strömbäck, 2011), `BPASS` (Eldridge et al., 2017), which provide templates for the spectral energy distributions of SSPs with different ages and metallicities. SPS models are considered fundamental tools in galaxy formation studies, as they allow us to predict galaxy properties and interpret observations. In particular, they play a crucial role in this work, where we will explore some of them to better constrain the properties of massive and passive galaxies used as cosmic chronometers.

1.2.3 Spectral indices

The optical spectra of passive galaxies exhibit prominent absorption features that reflect the underlying distribution of stellar ages, metallicities, and elemental abundance patterns. Since the pioneering work of Faber (1973), dedicated spectral analysis tools have been developed to investigate these characteristics. When coupled with SPS models, these tools enable astronomers to derive key physical properties of galaxies, such as the mean age of their stellar populations, overall metallicity, and even the relative enhancement of α-elements. This approach provides crucial insights into the star formation histories of passive galaxies.

In this context, a crucial role is played by a standard system for the measurement and calibration of the main absorption features of galaxy spectra, known as the Lick/IDS system. The Lick indices are the result of an effort using observation data from Lick Observatory (Faber, 1973; Burstein et al., 1984; Worthey, 1994; Worthey & Ottaviani, 1997; Trager et al., 1998) to relate characteristics of stars with their spectral features by creating a catalog of stars of known characteristics (e.g., age, metallicity, spectral class) and the values of the corresponding Lick indices. With this library, spectra of populations such as the stars of distant (possibly unresolvable) galaxies and stellar clusters can be compared to mixes of known types of stars to derive their characteristics. This system consists of 25 indices, defined over the spectral range $\sim 4000-6000$ Å (restframe) produced by several absorbers, both atomic and molecular (e.g. Fe, Mg, Ca, CN, NaD).

Each Lick index corresponds to a spectral line, consisting of a comparison of the strength of a narrow spectral band centered on the line to that of the surrounding continuum, expressed in terms of magnitudes, I_m (molecular indices), or in Å, I_a (atomic indices). The following definition are provided by (Trager et al., 1998):

$$I_a = \int_{\lambda_{c_1}}^{\lambda_{c2}} \left(1 - \frac{F_I(\lambda)}{F_C(\lambda)}\right) \mathrm{d}\lambda \qquad [\mathring{A}] \tag{1.30}$$

$$I_m = -2.5 \log \left(\frac{1}{\lambda_{c_1} - \lambda_{c_2}} \int_{\lambda_{c_1}}^{\lambda_{c2}} \frac{F_I(\lambda)}{F_C(\lambda)} \mathrm{d}\lambda \right) \qquad [mag] \tag{1.31}$$

where the interval $(\lambda_{c_1}, \lambda_{c_2})$ defines the central band, $F_I(\lambda)$ and $F_C(\lambda)$ are the flux of the index and of the pseudo-continuum, respectively. The flux $F_C(\lambda)$ can be estimated from linear interpolation as:

$$F_C(\lambda) = F_b \frac{\lambda_r - \lambda}{\lambda_r - \lambda_b} + F_r \frac{\lambda - \lambda_b}{\lambda_r - \lambda_b} \tag{1.32}$$

Here λ_b and F_b are the central points and the flux mean values for the two side regions of pseudo-continuum (in red and blue). For each index, the central band and the two sidebands in the red and blue continuum are reported in Table A.1 for each index.

A key property characterizing the spectra of passive galaxies is the presence of a discontinuity at ~ 4000 Å restframe. The strong break occurs in older stellar populations owing to a sudden accumulation of absorption features blueward of 4000 Å that appear in stars cooler than G0 (6000 K) as a result of ionized metals. In hotter stars, elements are multiply ionized, and the opacity decreases, so the break is less prominent. Since hot stars are short-lived, the D4000 index increases monotonically with stellar age. The strength of this spectral feature is measured as the ratio of the average flux densities between two spectral regions close to the break. In the literature, two definitions of the D4000 index are commonly found. The classical one, introduced by Bruzual A. (1983), uses wide continuum bands on either side of the break, defined by $(\lambda_{1b} - \lambda_{2b})$ and $(\lambda_{1r} - \lambda_{2r})$:

$$\mathrm{D4000} = \frac{\lambda_{2b} - \lambda_{1b}}{\lambda_{2r} - \lambda_{1r}} \frac{\int_{\lambda_{1r}}^{\lambda_{2r}} F_\nu \mathrm{d}\lambda}{\int_{\lambda_{1b}}^{\lambda_{2b}} F_\nu \mathrm{d}\lambda} \tag{1.33}$$

A revised version, proposed by Balogh et al. (2004), adopts narrower sidebands to reduce the sensitivity of the measurement to dust extinction. To distinguish between the two, the latter is referred to as D_n4000. The sideband intervals used in both definitions are listed in Table A.2.

1.2.4 Basics of Galaxy Formation and Evolution

The central aim of galaxy formation theory is to explain how relatively simple physical principles can lead to the wide range of complex phenomena observed in galaxies. A full description is available in Benson (2010).

Modern theories of galaxy formation have their roots in the early developments of cosmology and the study of structure formation. These theories are framed within the context of the ΛCDM model and follow a primarily hierarchical structure formation scenario, where small systems gradually merge to form larger ones. The linear theory of cosmological perturbations is well understood and provides an accurate description of the early evolution of small perturbations seeding the formation of structures in the Universe. In this context, a characteristic length scale, known as the *Jeans length* (λ_J), can be defined. This scale depends on the density (ρ) and velocity dispersion (v) of the system, following the relation $\lambda_J \propto v/\sqrt{\rho}$. It represents the minimum size that a structure must have to undergo gravitational collapse under the given environmental conditions.

The behaviour of baryonic matter is more complex to describe than that of dark matter due to the various types of interactions it undergoes. However, it is generally thought that the collapse of baryonic structures essentially follows that of CDM structures, which, once formed, create gravitational potential wells where baryonic matter can accumulate.

In the case of early-type galaxies, which are the target of this work, this process is currently described by a two-phase model (Oser et al., 2010). This model proposes

an initial rapid phase of *in situ* mass accretion and star formation, during which the progenitor of the present-day galaxy is built, followed by a second phase, more extended in time, involving the acquisition of mass from external sources through mergers (*ex situ growth*). Interestingly, observational studies of early-type galaxies have revealed a trend that contrasts with the predictions of the classical hierarchical assembly scenario. Specifically, stellar mass appears to play a crucial role in their formation and evolution. There is substantial evidence suggesting that the most massive systems formed earlier, during short but intense episodes of star formation, while less massive systems formed later (at lower redshifts) and exhibit a more extended SFH. It is worth emphasizing that the very short star formation timescales provide a natural explanation for why these galaxies typically exhibit super-solar [α/Fe] ratios. This, in turn, highlights the importance of employing α-enhanced models in the study of cosmic chronometers. Incorporating such models represents a promising direction for future work and could serve as a natural continuation of this thesis.

This alternative formation scenario, known as *mass-downsizing* (Cowie et al., 1996; Cimatti et al., 2006; Thomas et al., 2010), becomes evident in Fig. 1.3, which presents the results from Thomas et al. (2010) showing how the specific star formation rate (defined as the SFR per unit mass, (sSFR) varies with look-back time across different stellar mass ranges. On the vertical axis, the sSFR is shown. On the horizontal axis, the *lookback time* is reported, representing the difference between the age of the Universe today and the one it had when the photons we receive from the galaxy were emitted. The Gaussian profiles are meant to model the SFH of galaxies with different masses: the centroid corresponds to the age of formation; the broadening indicates the duration of the star formation activity. We can notice that going back in time, we find galaxies with an enhanced and brief star formation rate.

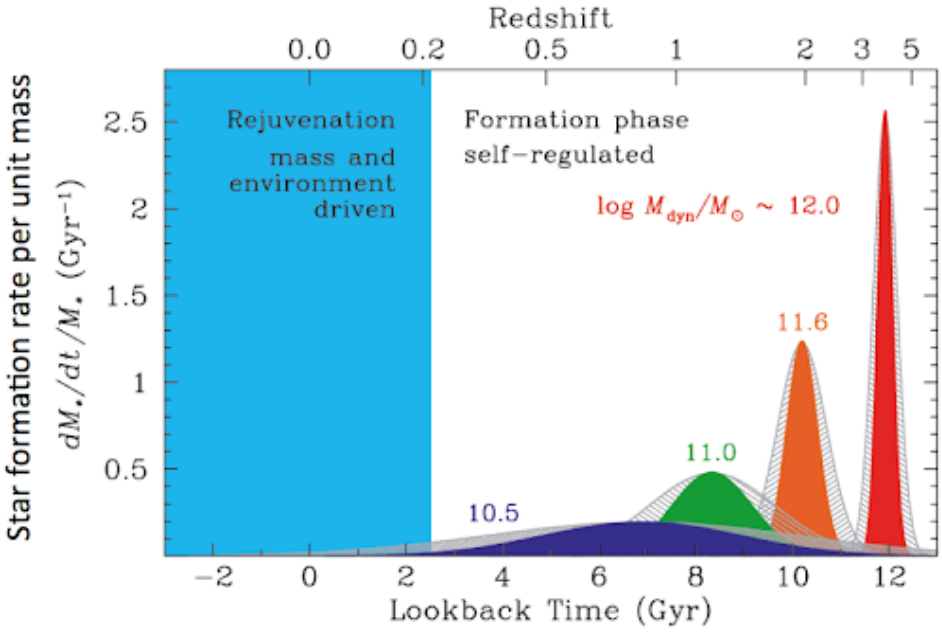

Figure 1.3: Evolution of the specific star formation rate as a function of time and redshift for a sample of massive galaxies with different masses, flagged by different colors. It is evident that the most massive galaxies are characterized by an earlier and shorter star formation activity. (from Thomas et al., 2010)

.

1.3 Cosmic Chronometers as cosmological probes

In the previous sections, we discussed the issue concerning the determination of the local value of the Universe's expansion rate, with particular emphasis on the crucial need to introduce new cosmological probes. This is essential to understand whether the observed tension arises from unaccounted systematic effects or if it provides hints of new physics.

In this context, very massive and passively evolving galaxies can be used to directly measure the Hubble parameter $H(z)$ with the minimal assumption of an FLRW metric, by measuring their aging $\mathrm{d}t(z)$:

$$H(z) = \frac{\dot{a}}{a} = -\frac{1}{(1+z)}\frac{\mathrm{d}z}{\mathrm{d}t}. \tag{1.34}$$

This method, known as the Cosmic Chronometers approach (CC Jimenez & Loeb, 2002), was first suggested with the idea that, provided accurate differential timing measurements, independent of absolute time, the expansion of the Universe can be tracked exactly as with a chronometer.

The great asset of this alternative cosmological probe is also evident from Eq. 1.34, where, apart from the FLRW metric, no further cosmological assumption is considered, providing a cosmology-independent estimate of the Hubble parameter. If the redshift

interval considered is sufficiently small, one can approximate $\mathrm{d}z/\mathrm{d}t \sim \Delta z/\Delta t$ and therefore, through CC, directly measure $H(z)$. A key step in this approach is to robustly constrain the differential age evolution of the Universe, which is done by taking advantage of massive and passive galaxies, which are excellent candidates to trace its aging (see Moresco et al., 2022; Moresco, 2024, for comprehensive reviews). Indeed, to properly apply the method, it is crucial to find a population of astrophysical sources with a homogeneous and synchronized formation time, that assembled most of their mass at very high redshift and that evolved without major further episodes of star formation so that they could be used to accurately map the *ticking* of cosmic time. This is exactly what we expect for the very massive and passive galaxies according to their scenario of formation and evolution, described in Sect. 1.2.4. There is extensive support in the literature for the scenario in which this type of galaxy formed at high redshift ($z > 2$–3; Citro et al., 2017; Carnall et al., 2018; Estrada-Carpenter et al., 2019; Carnall et al., 2019) and very rapidly ($t < 0.3\,\mathrm{Gyr}$; Thomas et al., 2010; Carnall et al., 2018). In this way, such galaxies would have quickly exhausted their gas reservoir and then evolved passively, making this population of objects very homogeneous both in terms of mass and metallicity.

The main aspects to pay attention to when using this method are primarily two: selecting a reliable sample of chronometers and accurately estimating their ages.

1.3.1 Selecting a sample of Cosmic Chronometers

As previously introduced, the first criterion for selecting a sample of cosmic chronometers is to focus on quiescent galaxies. Identifying such population is not a trivial task, since to ensure a proper selection it requires a thorough analysis of various features, including their color, the shape of the SED and spectrum, the presence of absorption and emission lines, and the strength of those lines (Moresco et al., 2013). Each of these properties contributes to characterize the galaxy type, yet none is sufficient on its own to reliably isolate a sample with the typical features of cosmic chronometers. In recent years, works by Moresco et al. (2018), Borghi et al. (2022b) and Tomasetti et al. (2023) have demonstrated that obtaining the purest possible CC sample requires combining multiple selection criteria:

- *Photometric selection.* The typical spectrum of a passive galaxy has a red continuum. Different color-color selections have been suggested in the literature, typically based on magnitude spanning a wide range of wavelengths (based on the availability) to better capture the slope of the spectrum. The most commonly used are the NUVrJ diagram (Ilbert et al., 2013), the UVJ diagram (Williams et al., 2009), and the NUVrK (Arnouts et al., 2013).

- *Spectroscopic selection.* Emission lines are known to be important tracers of potential ongoing star formation. It is fundamental to consider one or more spectroscopic

criteria aimed at removing possible contamination from galaxies with ongoing star formation. In this context, the most relevant emission lines are those corresponding to the Balmer sequence or to oxygen emission, namely [OII]λ3727, Hβ ($\lambda = 4861$ Å), [OIII]λ5007, and Hα ($\lambda = 6563$ Å). Different criteria can be implemented, based on the integrated flux of the line, on its equivalent width (EW), or on the measured SNR ratio. Moreover, a recently proposed spectral indicator is the Ca II H/K line ratio, which can reveal contamination from young stellar components. The presence of the Hϵ line at 3970 Å, blending with Ca II H, can invert the typical depth ratio, where Ca II K is normally stronger than Ca II H. The addition of this diagnostic can help to improve the quality of the selected sample (e.g. Borghi et al., 2022b; Tomasetti et al., 2023).

- *High mass (or velocity dispersion) selection.* Following the discussion in Sect. 1.2.4, objects with higher masses are also the oldest ones, most coeval, and with the most synchronized SFH. To exclude less massive galaxies, which may not satisfy these properties, a good point could be to apply a cut in stellar mass or, equivalently, in velocity dispersion σ (that correlates with the stellar mass in early-type galaxies).

In the end, the combination of photometric, spectroscopic, and mass selection has been proven, by several works (e.g. Moresco et al., 2016; Borghi et al., 2022b; Tomasetti et al., 2023), to be the most effective in obtaining the purest possible sample of CC.

1.3.2 Measuring relative ages

To apply the CC method, once the sample has been selected accurately, we need to estimate the two unknown quantities $\mathrm{d}z$ and $\mathrm{d}t$, which appear in Eq. 1.34. If, on the one hand, the redshift can be determined with very high accuracy ($\sigma_z \lesssim 0.001$), thanks to the advent of large spectroscopic surveys, measuring the ages of a stellar population is not trivial at all. The main problem is that different physical parameters of galaxies affect the shape of their spectrum in degenerate ways, so that a change of one parameter can be compensated by the variation of the other one to produce a very similar spectrum. This issue of degeneracy will be explored in more detail in the following Chapter, as it proved to be a critical factor in the analysis of the data used in this study.

To date, various methods have been investigated to estimate the ages of CCs. Some approaches make use of the full available spectral information, while others focus specifically on the analysis of spectral lines that are particularly sensitive to age:

- *Lick indices.* This approach is based solely on the absorption features of the spectrum, since they hold significant information about the properties of the galaxy. Different absorption lines trace distinct physical properties of stellar populations, as extensively discussed in Sect. 1.2.3. By comparing observed indices with model grids

as those developed by Bruzual & Charlot (2003), one can break the age-metallicity degeneracy. Tools like `indexf` (Cardiel, 2010) and `pyLick` (Borghi et al., 2022b) offer public resources for index measurement and analysis.

- *D4000 break.* A different method was introduced by Moresco et al. (2011), who proposed to use as an age indicator a common spectral feature in early-type galaxies, the 4000 $\mathring{A}$ break (D4000). Assuming a linear relation of the form:

$$\mathrm{D4000} \propto A(Z, \mathrm{SFH}) \cdot t_{\mathrm{Age}} \tag{1.35}$$

where the coefficient A accounts for variations in the stellar population parameters (such as metallicity Z and SFH). When we combine this equation with Eq. 1.34, we get:

$$H(z) = -\frac{A(Z, SFH)}{(1+z)} \frac{\mathrm{d}z}{\mathrm{dD4000}}. \tag{1.36}$$

This new equation has the advantage that statistical and systematic errors have been decoupled, since $\mathrm{d}z/\mathrm{dD4000}$ is a purely observational quantity to be estimated from the data and $A(Z, SFH)$ is a parameter that encompasses all systematic effects and model dependencies.

- *Full spectral fitting.* This method is a statistical approach that compares the observed spectrum and/or photometry of a galaxy with a grid of SPS templates, finding the one that better reproduces the observation and hence deriving the properties of the source. Typically, a combination of spectroscopic and photometric data is considered. Taking advantage of the full spectral information, the benefit of this approach is that it can provide a joint constraint on all properties, and the larger the wavelength coverage, SNR, and resolution, the more information can be retrieved and degeneracies between parametersthat broken. To date, several codes are available to perform FSF, including: `MOPED` (Heavens et al., 2000, 2004), `STARLIGHT` (Cid Fernandes et al., 2005), `VESPA` (Tojeiro et al., 2007), `ULySS` (Koleva et al., 2009), `BEAGLE` (Chevallard & Charlot, 2016), `FIREFLY` (Wilkinson et al., 2017), `pPXF` (Cappellari, 2016), `BAGPIPES` (Carnall et al., 2018), and `FSPS` (Conroy et al., 2009).

  However, only few measurements of $H(z)$ have been obtained so far with this approach (namely Ratsimbazafy et al., 2017; Jiao et al., 2023; Tomasetti et al., 2023).

1.3.3 Systematic uncertainties

The key idea of the CC method is to analyze an homogeneous galaxy population across different redshifts, enabling a sensible comparison of their ages to serve as reliable tracers of the Universe's age. However, several factors may challenge this assumption and must

therefore be carefully monitored and controlled. Some of the effects which may contribute to the total error budget are listed below:

Contamination of young star-forming outliers

Even after the selection process for cosmic chronometers is completed, the sample may still be contaminated by galaxies with residual star formation or that have experienced a recent burst of star formation. Although these young stellar populations may not dominate the galaxy mass, they can significantly affect the overall SED, compromising the accuracy of age estimates.

Adopting a careful selection process based on multiple, complementary criteria is, in most cases, sufficient to eliminate contamination from SFGs. However, the presence of residual star formation in passive galaxies may require a more detailed analysis involving various indicators, such as the UV flux (Kennicutt, 1998) or the presence of emission lines (Magris C. et al., 2003).

Progenitor bias

Another relevant effect is the *progenitor bias* (van Dokkum et al., 2000). This arises from the fact that, within a given redshift range, a selection criterion may become more stringent at higher redshifts, simply because the galaxies observed are, on average, younger than those at lower redshifts, as they are their progenitors. When this occurs, the resulting age–redshift relation may appear artificially flatter, introducing a bias in the measurement of $H(z)$. This effect is generally minimized in the application of the CC method, since the redshift intervals over which Δt is computed are kept very small.

Effect of the adopted SPS models

All the age estimates rely on the adopted SPS models, which allows us to interpret some observational features in terms of physical parameters (see. Sect. 1.2.2). As discussed in Moresco et al. (2020) the choice of the SPS models, can significantly affect age estimates and, consequently, the measurement of $H(z)$. Currently, this represents the largest source of systematic uncertainty not related to the Δt estimation process, and it has been shown to contribute, on average, at the level of approximately 4.5%. This highlights the importance of exploring new SPS models to better understand and mitigate systematics affecting the CC method.

1.4 Open questions in cosmology

In recent years, the CC technique has been further developed and explored, proving to be a powerful tool for constraining the Hubble parameter in a cosmology-independent

way. Nevertheless, the method is still relatively young and requires further refinement before it can be fully and reliably applied, as current measurements remain dominated by systematic uncertainties.

Among the possible future developments, one of the most promising directions is the FSF technique, which allows one to exploit the full information contained in both spectroscopic and photometric data, while helping to break degeneracies among model parameters. In fact, a comprehensive treatment of the systematic effects associated with this approach is still lacking, since systematics have been investigated primarily through the D4000 method to date (Moresco et al., 2020).

This is one of the aspects investigated in this thesis. We apply the CC method through the FSF approach by analyzing a sample of high-quality spectra from the SDSS BOSS survey. Our goal is to improve the treatment of systematics in the application of the FSF method providing a complete framework to address them, and at the same time to explore possible refinements in their modeling by assessing their impact on the estimation of $H(z)$. In particular, we investigate the influence of the adopted SPS models, the choice of the IMF and the stellar libraries. This analysis also opens the path toward the inclusion, in the future, of models accounting for α-enhancement, which may be more suitable when dealing with passive and massive galaxies.

Chapter 2

An optimal sample of Cosmic Chronometers

In this Chapter, we provide a description of the data used to carry out this work. First, we present an overview of the spectroscopic survey from which galaxies have been extracted. Starting from the original parent sample, several criteria have been applied to select a sample of massive and passive galaxies that are as little contaminated as possible by outliers and have spectra with the highest signal-to-noise ratio available. We provide a first characterization of the sample by measuring its absorption features, and studying their behaviour as a function of redshift and stellar mass. All the measurements contribute to the creation of a *bona-fide* sample of cosmic chronometers. This selection procedure, which will be illustrated in detail, is fundamental to ensuring the reliability and success of the method.

2.1 The SDSS BOSS survey

The Sloan Digital Sky Survey (SDSS) is one of the most ambitious and successful projects in the history of astronomy (York et al., 2000). The survey has created the most detailed three-dimensional maps of the Universe ever made, with deep, multi-color images of one-third of the sky and spectra for more than three million astronomical objects. A distinctive trait of the SDSS family of surveys is the regular release of high-quality, well-documented, and readily usable data to the global scientific community, enabling broad scientific reach and impact. The current data release, DR19, represents the second release of the fifth phase of the SDSS, continuing the operations that began with the Early Data Release (Stoughton et al., 2002). Since then, each successive release has brought substantial advancements in both scientific scope and instrumentation.

The SDSS uses a dedicated wide-field 2.5 m telescope located at Apache Point Observatory (APO), in South-East New Mexico at an elevation of 2800 m. The telescope,

built to accommodate the requirements for both imaging and spectroscopy, is shared by the camera and spectrographs, which mount at the Cassegrain focus. The imaging survey was carried out on clear, dark nights with good seeing using the 120 mega-pixel camera, which operates in drift-scanning mode using a 5×6 array of 2048×2048 pixel detectors to obtain *ugriz* (Fukugita et al., 1996) photometry. The camera slowly reads the CCDs as the data is being collected, while the telescope moves along great circles on the sky so that images of objects move along the columns of the CCDs at the same rate the CCDs are being read. The SDSS imaging survey provides the two-dimensional locations of nearly one billion celestial objects; then, spectroscopy of a selected subset of targets is used to determine redshifts and thus distances.

The original SDSS initiative targeted spectroscopy for one million galaxies and 100,000 quasars across approximately 10,000 $\deg^2$ of sky. To efficiently obtain such a vast number of spectra with moderate resolution, sufficient for accurate redshift estimation, SDSS employed fiber-fed, multi-object spectrographs capable of observing hundreds of targets simultaneously across a wide field of view. These spectrographs were later improved for the Baryon Oscillation Spectroscopic Survey (BOSS; Schlegel et al. 2009). Each spectrograph has two cameras, one red and one blue which allow a wavelength coverage of about 3600 - 10400 Å, with a dichroic splitting the light at roughly 6000 Å. The adopted design has a resolution R = 1560 - 2270 in the blue channel and R = 1850 - 2650 in the red channel.

BOSS, from which the data used in this work are derived, represents the central component of the third-generation Sloan Digital Sky Survey (SDSS-III). It was designed to map an extensive cosmic volume and to trace the large-scale distribution of galaxies and quasars. The primary objective of BOSS was to measure the expansion history of the Universe with percent-level precision by detecting the BAO signature imprinted in the early Universe.

In addition to constraining cosmological models, BOSS has delivered an outstanding sample of galaxies and quasars that is ideally suited to probing the formation and evolution of galaxies in the Universe, thanks to the high level of spectral detail. By studying the various key absorption features in the spectra, we can estimate the age and metallicity of the stars in these galaxies and thus determine how and when they formed. As evident from Fig. 2.1, the limited overlap between the BOSS wavelength coverage and the photometric bands available in the SDSS implies that photometry alone offers limited utility for a detailed analysis of these spectra. Overall, the large sample size of BOSS, combined with the spectral resolution of its spectrographs, motivated the use of data from this survey for the application of the Cosmic Chronometers method.

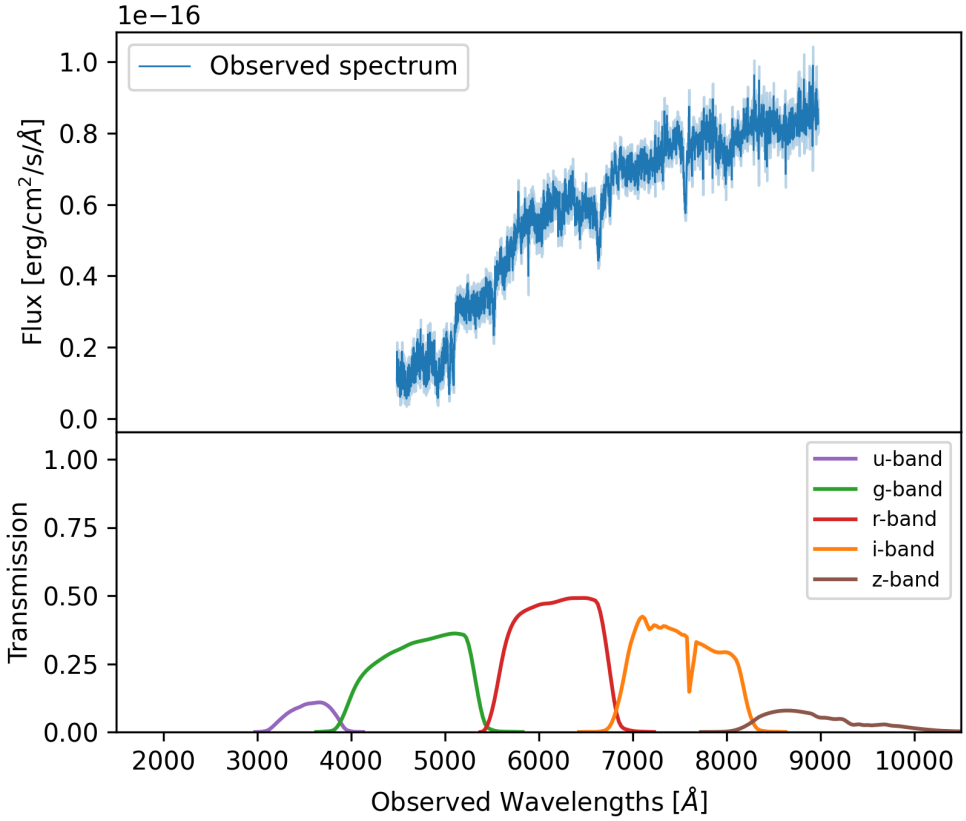

Figure 2.1: Example of a galaxy spectrum from the SDSS BOSS survey. The *upper* panel shows the observed spectrum of one of the analyzed galaxies, while the *lower* panel displays the transmission curves of the photometric bands (u, g, r, i, and z).

2.2 Data analysis

In Sect. 1.3.1, it was highlighted that, to properly apply the CC method, it is essential to select a sample of massive and passively evolving galaxies that is as pure as possible. This requires selecting galaxies excluding any potential contamination from star-forming objects, since different levels of contamination at various redshifts can affect the slope of the age–redshift relation, and consequently the determination of the Hubble parameter.

Previous works (Moresco et al., 2013; Borghi et al., 2022b; Tomasetti et al., 2023) have shown that adopting a single selection criterion is not sufficient in this context. Therefore, in the present work, several criteria – photometric, spectroscopic, and stellar mass cuts – have been combined to ensure the purity of the final sample.

2.2.1 Exploring a combination of selection criteria

The parent sample was constructed by combining different SDSS tables to extract both the spectroscopic and photometric information of passive galaxies from BOSS, resulting in an initial dataset of 1,302,569 galaxies. Starting from this sample, the following selection criteria were applied:

- **color cut**. According to the description of early-type galaxies provided in Sect.1.2.1, a first distinction can be made in terms of colors, as these galaxies are expected to be the reddest ones. Unfortunately, as shown in Fig. 2.1, the photometric data available for BOSS are limited. Therefore, to select passive galaxies from a photometric point of view, we applied a cut of $g - i > 2.35$, which has been proven to efficiently select passive galaxies (Masters et al., 2011; Moresco et al., 2016).
  This reduced the sample to 751,693 galaxies.

- **emission-lines cut**. It is also important to select galaxies without detectable emission lines. In particular, the sample was further cleaned by applying a cut on the equivalent width of the [OII] line, which is an indicator of ongoing star formation as it traces photoionized gas. In this context, as done in various works (e.g., see Mignoli et al., 2009; Moresco et al., 2016; Tomasetti et al., 2023), star-forming objects exhibiting an equivalent width EW([OII]) > 5 Å were discarded to ensure the exclusion of systems with significant recent star formation.
  After this cut, the sample was reduced to 343,227 galaxies.

- **velocity-dispersion cut**. There is evidence that the oldest, most coeval, and synchronized star formation history objects are those with higher mass, and hence, higher velocity dispersion σ, which correlates with stellar mass in early-type galaxies (e.g., see Thomas et al., 2010).
  A cut of $\sigma > 250$ km/s was applied to decrease contamination from star-forming outliers.
  After this cut, the sample consisted of 150,199 galaxies.

- **signal-to-noise ratio cut**. Since we were dealing with very high statistics, we decided to maximize the signal-to-noise ratio in the r band by selecting objects with $SNR[r] > 10$. The trade-off was that, as a result, only galaxies in the low-redshift range were considered ($z < 0.5$) .
  At the end of this preliminary selection, the final sample consisted of 3,216 galaxies.

Figure 2.2 reports the histograms of several properties of the sample, showing how the different adopted cuts impact their distribution. By inspecting the distributions of the final sample, it becomes evident that the applied cuts effectively isolate the galaxies

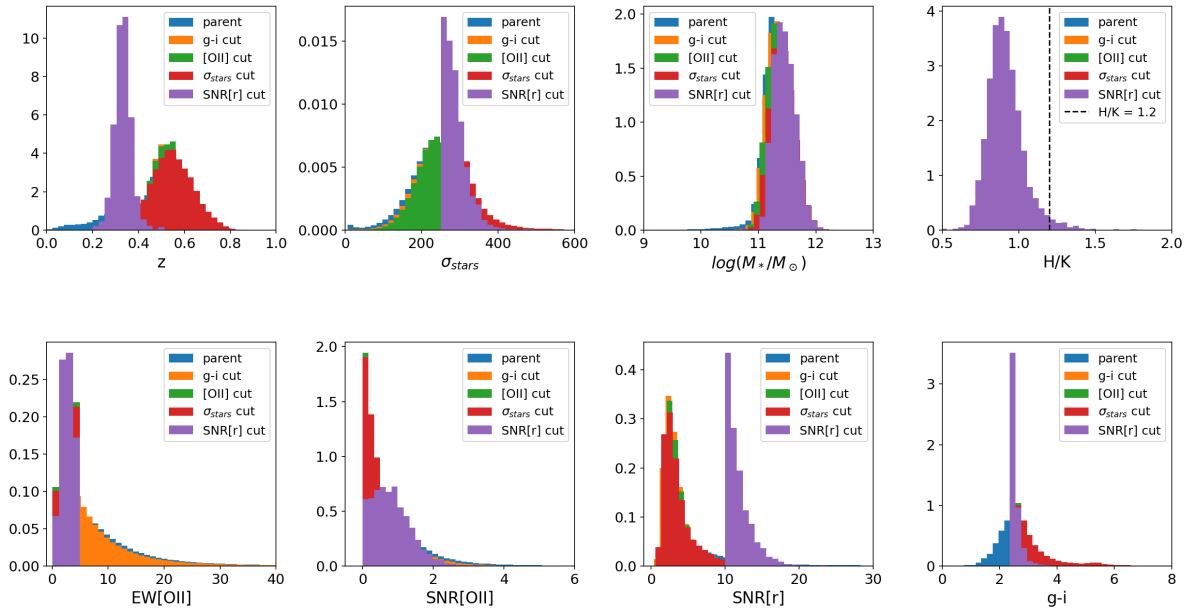

Figure 2.2: Histograms showing the distributions of the physical and spectral properties of the samples at each selection step, as indicated in the legend and described in Sect. 2.2.1. It can be observed that the application of the H/K cut, which was the final criterion, did not significantly alter the sample. This is justified by the robustness of the previous selection steps, which were already sufficient to isolate this class of objects.

with the desired properties. Specifically, the velocity dispersion distribution shifts toward higher values, as does the stellar mass distribution, indicating a preference for more massive systems. Conversely, the EW[OII] distribution moves toward lower values, consistent with the exclusion of galaxies showing signs of ongoing star formation. The SNR of the continuum in the r band shifts toward higher values, as expected from the selection of spectra with higher quality. However, this improvement in spectral quality comes at the expense of redshift coverage, as the remaining galaxies are mostly confined to $z < 0.5$.

2.2.2 Conversion of wavelengths from vacuum to air

Before describing the methods used to analyze and measure the properties of the spectra, it is important to remember that the BOSS catalog provides wavelengths measured in vacuum. However, the analysis codes used in this work operate with wavelengths in air. To avoid inconsistencies, it is therefore necessary to convert the vacuum wavelengths to air wavelengths.

Since Data Release 9 (DR9) in 2012, SDSS has applied a standard conversion based on the refractive index of air to transform vacuum wavelengths (expressed in Angströms) to air wavelengths. The refractive index n is calculated using the following empirical

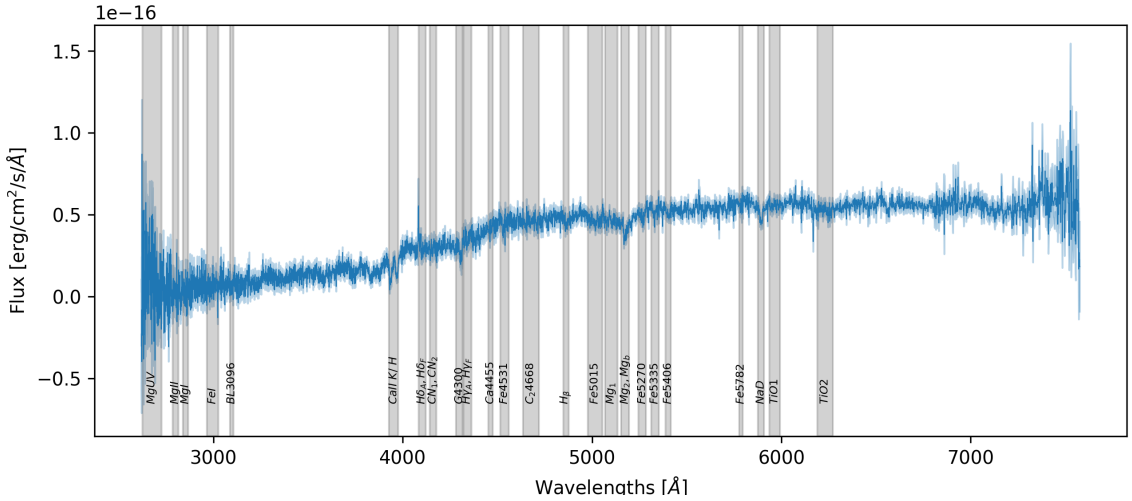

Figure 2.3: Example of a rest-frame galaxy spectrum used in this study. The shaded regions highlight the passbands of selected Lick indices, as measured by the `pyLick` code.

formula, derived from (Ciddor, 1996):

$$n = 1 + \frac{5.792105 \times 10^{-2}}{238.0185 - \left(\frac{10^4}{\lambda_{\rm vac}}\right)^2} + \frac{1.67917 \times 10^{-3}}{57.362 - \left(\frac{10^4}{\lambda_{\rm vac}}\right)^2} \tag{2.1}$$

where $\lambda_{\rm vac}$ is the vacuum wavelength in Angströms. The two terms represent the dispersion of air as a function of wavelength based on laboratory measurements. The conversion to air wavelength is then performed using:

$$\lambda_{\rm air} = \frac{\lambda_{\rm vac}}{n}, \tag{2.2}$$

where $\lambda_{\rm air}$ is the wavelength as it would be measured in air. This correction ensures consistency with calibration standards and with the spectral line databases that provide rest-frame wavelengths in air.

2.2.3 Measuring absorption features

The selection described so far allowed us to identify a sample of cosmic chronometers for which we investigated spectroscopic properties from a quantitative perspective. To carry out this analysis, we adopted the Python code `pyLick` (Borghi et al., 2022a), developed to measure Lick indices (as fully described in Sect. 1.2.3), along with other spectral features relevant for passive galaxies, such as the D4000 break. The main Lick indices used in this study are listed in Table A.1 and illustrated in Fig. 2.3.

The analysis of these indices enables a preliminary quantitative assessment of the sample's properties and their evolution with redshift. Among the measured features,

particular attention is devoted to the following indices:

- **Hδ_A** and **Hδ_F**: these indices sample the Hδ region and differ mainly in the width of their central bandpass: approximately ∼40 Å for Hδ_A and ∼20 Å for Hδ_F, to better sample the absorption features of type A and F stars (Worthey & Ottaviani, 1997). They are widely used as age indicators but also exhibit sensitivity to variations in α-element abundances, which become significant at super-solar metallicities (Thomas et al., 2004; Lee & Worthey, 2005). This latter effect is primarily due to Fe absorption bands falling within the pseudo-continuum regions, and it is less pronounced for Hδ_F, making this index less sensitive to [α/Fe] variations.

- **Hγ_A and Hγ_F**: apart from a stronger sensitivity to carbon abundance, these indices behave very similarly to the Hδ_A and Hδ_F indices. As in the previous case, the index defined over a narrower wavelength range, Hγ_F, is less sensitive to abundance variations and can therefore serve as a more robust age indicator.

- **Hβ**: this index shows a strong sensitivity to age (Worthey, 1994). However, weak emission lines in this region may contaminate the spectrum and affect the age estimation.

- **Mg_1, Mg_2, Mg b**: main indicators of α-element enrichment but they are sensitive also to [Z/H], C, Fe. The central bands of Mg_2 and Mg b sample the same spectral region where it is also present the triplet of MgI (5167, 5173, 5184 Å), while that of Mg_1 is defined in a bluer region.

- **MgI, MgII, FeI**: as described by (Maraston et al., 2008), these indices show a peak in the presence of type F and G stars, while they are not present in hotter stars of type O and B. All have a partial dependence on the metallicity, but for FeI this is very weak, making it a suitable tool to separate the effects on the age and metallicity (Chavez et al., 2007).

- **Fe5270, Fe5335**: they present a similar behaviour and they are very sensitive to the abundances of Fe, [Z/H], and Mg (Tripicco & Bell, 1995; Thomas et al., 2004).

- **D4000 and D_n4000** Discontinuities which are proven to probe very well the ages of passive galaxies. It has been verified that the dependence on [α/Fe] is reduced (Moresco et al., 2012).

To avoid the analysis to be biased, we also masked the wavelength regions of the main night-sky emission lines (namely $\lambda = 5577$ Å), as shown in Fig. 2.4.

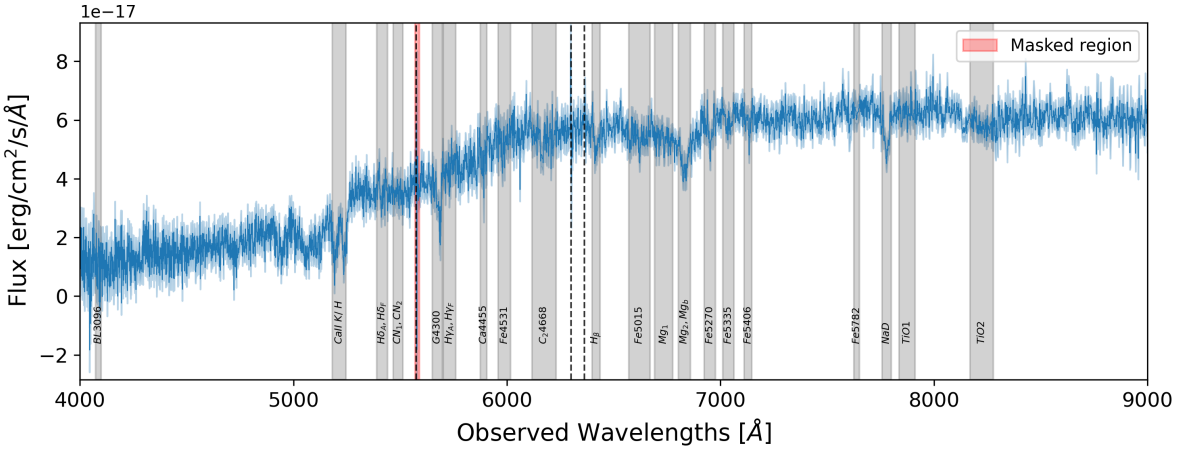

Figure 2.4: Observed spectrum of one the analyzed galaxies. Grey shaded bands mark the regions corresponding to the Lick spectral indices. The dashed vertical lines denote sky emission lines at 5577 Å 6300 Å, and 6363 Å . The red shaded region highlights the wavelength interval 5570–5585 Å, which has been masked to avoid contamination when measuring Lick indices.

2.2.4 Analysis of the observational properties

To be compared with theoretical models, the index measurements obtained have to be corrected for the effects of the galaxy's velocity dispersion on the observed spectrum. It is well-known that velocity dispersion along the line of sight broadens absorption lines, while models are typically provided at $\sigma = 0$.

The Lick/IDS system is based on an empirical stellar library. To accurately compare galaxy index measurements with single stellar population model predictions, the raw indices must be corrected to a reference value of zero velocity dispersion. Following the prescription in Carson & Nichol (2010), each measured index can be expressed as the product of the intrinsic index and a correction factor C_l, which is modeled as a third-order polynomial in velocity dispersion σ:

$$C_l = \sum_{i=0}^{3} b_i \sigma^i. \tag{2.3}$$

Here, the coefficients b_i, which vary for each spectral index, are taken from Carson & Nichol (2010). The corrected measurements are then used to study the evolution of the corresponding spectral features with redshift, as shown in Fig. 2.5.

The measurements of these features were carried out on a galaxy-by-galaxy basis, since, as described above, we chose to select the highest-SNR spectra available, which allow for this type of analysis. To investigate the redshift evolution of the indices and their dependence on galaxy mass, the sample was first divided into seven redshift bins and subsequently into four σ bins, corresponding to the quartiles of the velocity dispersion

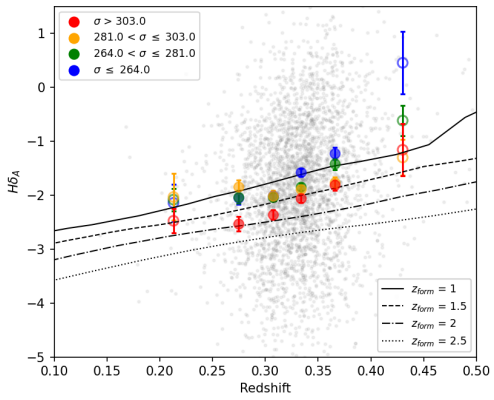

(a) Hδ_A vs. z

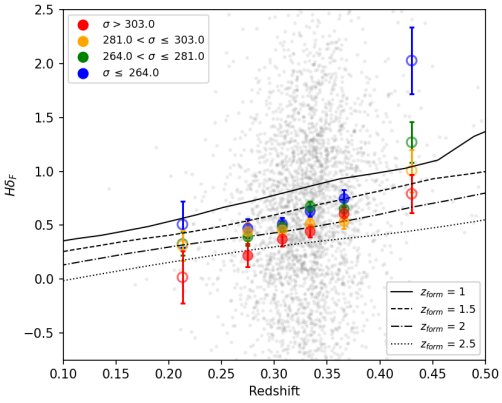

(b) Hδ_F vs. z

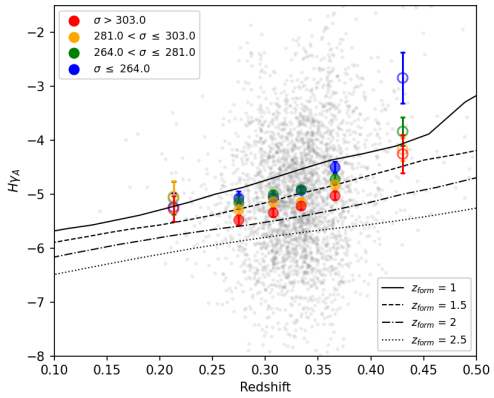

(c) Hγ_A vs. z

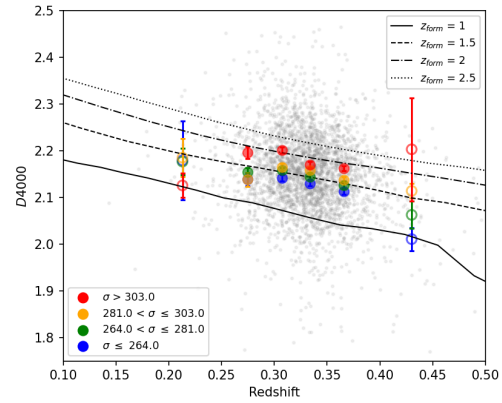

(d) D4000 vs. z

Figure 2.5: Redshift evolution of spectral indices for different features. Each colored point represents the mean value in each bin of z and σ: in grey the full sample. For bins where the statistics was insufficient the points are empty. Models from (Bruzual & Charlot, 2003) and (Le Cras et al., 2016).

distribution. From a preliminary analysis, we found that the central redshift bins yield the most statistically reliable measurements. Consequently, we adopted a finer sampling around these central values, while merging the two outermost bins to enhance statistical robustness. This procedure ultimately resulted in six bins in redshift and four bins in σ. In the following, bins with low statistical significance are indicated by empty markers.

Some of the measured indices are reported in Fig. 2.5, where individual measurements for each spectrum are colored gray, while the mean values within each redshift and velocity dispersion bin are colored. The error bars represent $\pm\,\mathrm{std}/\sqrt{N}$. The observed trends are compared with theoretical model predictions assuming different formation redshifts, represented by distinct lines. For the D4000 and Hδ indices, models from Bruzual & Charlot (2003) are employed, whereas the remaining spectral features are compared with

the models from Le Cras et al. (2016).

Even at this preliminary stage of spectral feature analysis, we found strong evidence for a mass-downsizing effect (see Sect. 1.2.4): more massive galaxies exhibit stronger age-sensitive indices. As shown in Fig. 2.5d, the data points corresponding to high-σ bins are systematically higher than those of the low-σ bins, indicating that high-mass galaxies are, on average, older than their low-mass counterparts.

In the specific case of the D4000 index, this behavior reflects both the increasing metallicity and the cooler average stellar temperatures in older stellar populations (Gallazzi et al., 2005), which enhance absorption features at wavelengths below 4000 Å. This trend provides an important first confirmation of the working hypothesis of this study: at higher redshifts, the galaxy population is, on average, younger and thus exhibits smaller D4000 values.

In addition to analyzing individual spectral features, index-index diagrams provide a powerful method for constraining the stellar population parameters of unresolved systems by combining absorption-line indices with different sensitivities to age, total metallicity, and α-element abundance. This technique involves selecting specific pairs of indices, typically one predominantly age-sensitive, such as a Balmer lines (e.g., Hβ, Hγ), and one more sensitive to metallicity or α-enhancement, such as Fe5270, Fe5335, or Mg b, and comparing their measured values with predictions from stellar population synthesis models. In this work, we used the models by Thomas et al. (2011) (hereafter TMJ), which are designed to account for variations in both overall metallicity and α-element enhancement, and are computed at MILES resolution, 2.50 Å (FWHM), for the standard set of Lick indices. By strategically pairing indices with complementary parameter sensitivities, this method allows us to break degeneracies, such as the well-known age-metallicity degeneracy, and obtain more robust estimates of age, metallicity, and chemical abundance patterns. In Fig. 2.6 we present some examples of these diagrams, Hβ-Mgb, Hβ-MgFe, Hβ-[MgFe]' and Hγ_F-[MgFe]'[1].

Among them, we also measured the pseudo-indices Ca II H and Ca II K, as the ratio between these two lines provides an additional criterion that has been demonstrated to effectively identify passive galaxies (Moresco et al., 2018; Borghi et al., 2022a; Tomasetti et al., 2023), due to its sensitivity to the presence of young stellar populations. In star-forming galaxies, the H/K ratio is typically higher, as the H line appears more prominent than the K line. This is because, in the presence of young type A and B stars, the Ca II H line overlaps with the Balmer Hϵ line at 3970 Å, resulting in a deepening of the H feature relative to the K line, which remains unaffected.

In this study, however, applying a cut on the H/K ratio does not exclude a significant number of objects, as it is possible to notice in Fig. 2.2. This indicates that the selection

[1]The definition of these indices are $[\mathrm{MgFe}]' = \mathrm{Mg}b \cdot \sqrt{0.72 \cdot \mathrm{Fe5270} + 0.28 \cdot \mathrm{Fe5335}}$ and $[\mathrm{MgFe}] = \mathrm{Mg}b + \langle \mathrm{Fe} \rangle$, and $\langle \mathrm{Fe} \rangle = 0.5 \cdot (\mathrm{Fe5270} + \mathrm{Fe5335})$

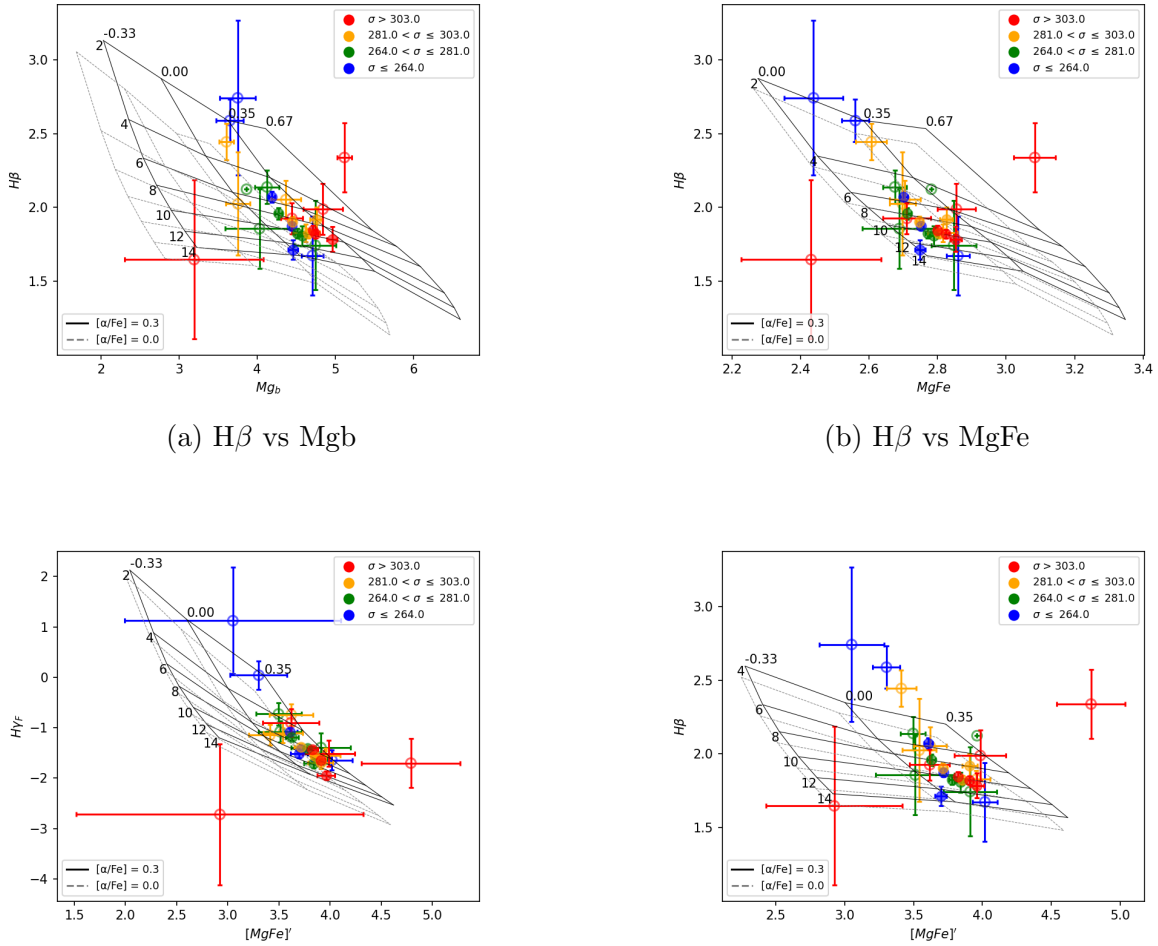

(a) Hβ vs Mgb

(b) Hβ vs MgFe

(c) Hγ_F vs [MgFe]'

(d) Hβ vs [MgFe]'

Figure 2.6: Index-index diagrams after applying the velocity dispersion correction. Each pair of panels shows a different combination of spectral indices, selected to help break the age-metallicity degeneracy and constrain the stellar population parameters. The background grids represent TMJ model predictions, with solid black lines corresponding to $[\alpha/\mathrm{Fe}] = 0.3$ and dashed grey lines to $[\alpha/\mathrm{Fe}] = 0.0$.

criteria adopted so far are highly effective in isolating a sample of cosmic chronometers with the purity required for our analysis.

2.2.5 Selection of a *golden* sample of cosmic chornometers

The goal of the final selection is to construct a set of CC that are as reliable and homogeneous as possible. To achieve this, we began by applying additional selection criteria to the previously defined sample, with a particular focus on the D4000 spectral index. This index is known to be a strong indicator of the stellar population age, especially in passive galaxies, making it an essential tool for selecting suitable CC.

Specifically, for all the bins of velocity dispersion and redshift previously defined, we

analyzed the distribution of the D4000 index. Since we aimed to isolate the most massive and passively evolving galaxies (those least affected by ongoing star formation), we applied a stricter selection. We retained only the galaxies belonging to the two highest σ bins, as these systems are statistically more likely to be the oldest passive galaxies in the sample, and we further required that each galaxy has a signal-to-noise ratio on the D4000 index greater than 60 (i.e., SNR(D4000) $>$ 60). This threshold ensures high confidence in the D4000 measurements and helps minimize the influence of noise on our age estimates.

After applying these criteria, the sample was reduced to 900 galaxies. This intermediate sample represents a critical subset for the following analysis. As we will discuss in subsequent sections, full spectral fitting will also be performed on this *extended* sample, as it provides a sample size still large enough to ensure meaningful statistical significance. This allowed us to investigate the stellar population properties in greater detail without compromising the robustness of the results.

To enhance the quality of the sample, we applied an additional selection within each bin. For every redshift and velocity dispersion bin, we considered only those galaxies with D4000 values above the 50th percentile of that bin's distribution. This percentile-based cut isolates the older portion of the galaxy population within each bin, ensuring consistency with the passive evolution scenario. Importantly, this procedure was implemented while maintaining uniform redshift coverage, thereby preserving our ability to probe the redshift evolution of the Universe. The final sample obtained through this multi-step selection process comprised 446 galaxies, as shown in Fig. 2.7a. This dataset serves as the foundation for our most stringent cosmic chronometers analysis, optimized to include only the most reliable tracers of differential aging across cosmic time.

To obtain a smaller and even more robust subsample, we next applied a stricter criterion based on the D4000 index. Specifically, within each redshift and σ bin, we selected galaxies with D4000 values above the 75th percentile of the distribution. This approach isolates the oldest galaxies in each bin, which are the most suitable for use as cosmic chronometers. After this cut, the sample was reduced to 226 galaxies, shown in Fig. 2.7b.

As a final step, we selected an even smaller sample by applying the most stringent constraints. First, we increased the threshold on the D4000 signal-to-noise ratio, requiring SNR(D4000) $>$ 70, to ensure maximum measurement accuracy. Then, following the same percentile-based approach, we again selected galaxies with D4000 values above the 75th percentile in each bin. This rigorous two-stage filtering resulted in a final sample of 84 galaxies, shown in Fig. 2.7c.

This smallest and most selective dataset represents the most robust group of CC in our analysis. While the reduced number of galaxies limits the statistical power, it maximizes the reliability of the age indicators and minimizes contamination from galaxies with younger stellar populations or uncertain spectral measurements.

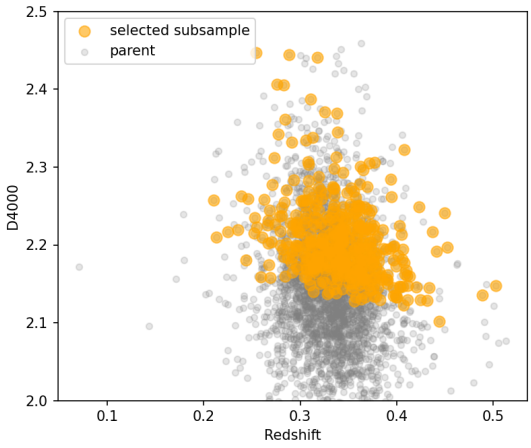

(a) D4000 50th percentile — 446 objects.

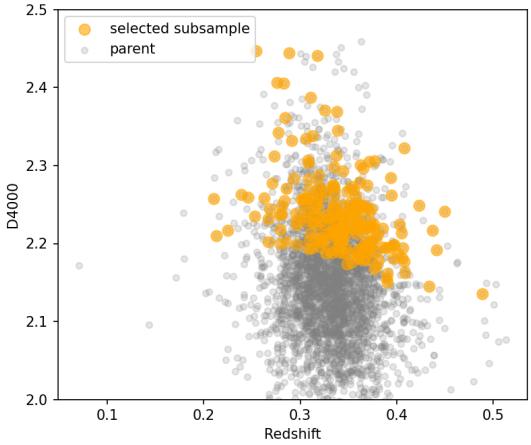

(b) D4000 75th percentile — 226 objects.

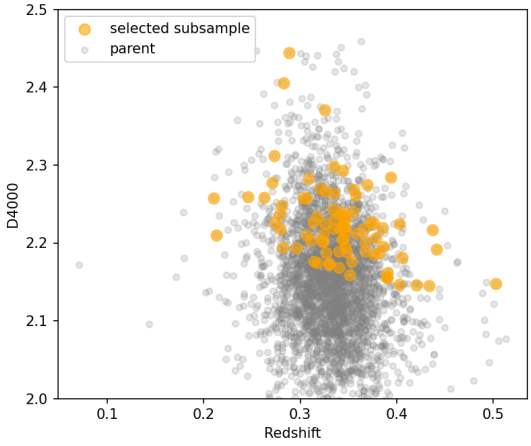

(c) Fig. 2.7b with SNR(D4000) > 70 — 84 objects.

Figure 2.7: Evolution of the sample selection based on D4000, described in Sect. 2.2.5

Chapter 3

Measuring the expansion rate of the Universe

In this Chapter, the analysis moves beyond index measurements to achieve tighter constraints on the physical parameters of massive and passive galaxies through full spectral fitting. This approach, based on a statistical framework and already introduced in Sect. 1.3.2, allows a more comprehensive characterization of stellar populations by exploiting the entire observed spectrum rather than a limited set of absorption features.
The analysis presented in the Chapter applies this method to the SDSS BOSS spectra of both the *golden* and *extended* galaxy samples, deriving age estimates that are subsequently used to derive a new measurement of the expansion rate of the Universe, the Hubble parameter $H(z)$. Particular attention is devoted to the impact of binning effects on the results. Finally, the derived measurements are incorporated into a cosmological analysis to constrain fundamental parameters within the ΛCDM framework and to provide a direct comparison with previous BOSS studies using the Cosmic Chronometers approach.

3.1 The Full Spectral Fitting method

Since the beginning of this century, an expanded methodology to derive stellar population parameters from spectra has been introduced and is now widely adopted: the full spectral fitting technique. FSF is a statistical approach that compares the observed spectrum of a galaxy with a grid of SPS templates to identify the model that best reproduces the observation, thereby inferring the physical properties of the source. When available, both spectroscopic and photometric data are jointly analyzed, taking full advantage of the information contained across the entire wavelength range.
Unlike classical index-based methods, FSF does not rely on specific spectral features but instead uses every reliable pixel in the observed spectrum to contribute to the fit. Since

spectra generally contain thousands of data points, this approach allows for the inclusion of a large number of free parameters, enabling the simultaneous determination of key stellar population properties such as age, metallicity, and elemental abundances. A crucial point, that will be further discussed later, is that the broader the wavelength coverage and the higher the spectral resolution and SNR, the more robustly FSF can constrain these properties and mitigate degeneracies between them.
Over the past two decades, several software packages have been developed to perform FSF, which have been listed in Sect. 1.3.2. These tools differ in their adopted optimization strategies, model libraries, and treatment of dust attenuation or star formation history, but all share the common goal of extracting the maximum physical information from galaxy spectra.
More recently, the development of advanced Bayesian statistical techniques has enabled a new generation of spectral modelling and fitting tools capable of efficiently exploring high-dimensional parameter spaces and providing posterior probability distributions for complex models. One such tool is the *Bayesian Analysis of Galaxies for Physical Inference and Parameter Estimation* (`Bagpipes`), developed by Carnall et al. (2018) to model the emission from galaxies across a broad wavelength range, from the ultraviolet to the microwave regime. In particular, this code has already been tested and optimized for fitting massive, passive galaxies used as cosmic chronometers (e.g. Tomasetti et al., 2023). In this work, we employ `Bagpipes` to perform, for the first time, full spectral fitting on SDSS BOSS data.

`Bagpipes` is a Python-based tool designed for the rapid generation of complex model galaxy spectra and for fitting these models to a wide range of observational data. The code enables the user to fit arbitrary combinations of spectroscopic and photometric datasets simultaneously, allowing for the robust derivation of galaxy physical properties through a fully Bayesian framework. Its flexible architecture permits the construction of detailed star formation histories and the inclusion of various physical components such as stellar populations, nebular emission, and dust attenuation, making it particularly well-suited for the analysis of both individual galaxies and large samples.

3.1.1 Bayesian inference

The Bayesian approach adopted in the code employs Bayes' theorem to update prior beliefs about a model or hypothesis given new data. This can be applied for parameter estimation, where constraints on the parameters of a given model are updated, or for model selection, where the relative probabilities of two or more different models are assessed.

Bayes' theorem states that given a set of data D and a hypothesis H with parameter vector θ:

$$P(\theta|D,H) = \frac{P(D|\theta,H)P(\theta|H)}{P(D|H)}. \tag{3.1}$$

Here, $P(\theta|H)$ is the *prior probability distribution* for the model parameters, representing what is known before considering the new data. $P(D|\theta,H)$ is the *likelihood*, i.e., the probability of obtaining the observed data given a particular set of parameter values under the hypothesis H. $P(\theta|D,H)$ is the *posterior probability distribution*, expressing what is known about the parameters after considering the data. Finally, $P(D|H)$ is the *Bayesian evidence* or marginal likelihood, representing how well the hypothesis explains the data overall.
This means that, given a model $\mathcal{M}$ which depends on a set of parameters θ, which are believed to describe the physics of the system, the observed spectrum f_λ is modelled by maximizing the probability of the parameters θ, given the model and the data. Then, in this specific context, Eq. 3.1 becomes:

$$\mathcal{P}(\theta|f_\lambda,\mathcal{M}) = \frac{\mathcal{L}(f_\lambda|\theta,\mathcal{M})\,\mathcal{P}(\theta|\mathcal{M})}{\mathcal{P}(f_\lambda,\mathcal{M})} = \frac{\mathcal{L}(f_\lambda|\theta,\mathcal{M})\,\mathcal{P}(\theta|\mathcal{M})}{\sum_\theta \mathcal{L}(f_\lambda|\theta,\mathcal{M})\,\mathcal{P}(\theta|\mathcal{M})}. \tag{3.2}$$

In our analysis, the hypothesis consists of a specific model parametrization within `Bagpipes`, such as the choice of dust model, the number and type of star formation history components, or whether nebular emission is included. Once the model is defined, prior probability distributions are specified for its parameters, and observational data f_i with associated uncertainties σ_i are provided to constrain those parameters.

The observational data are incorporated through the likelihood function, which, under the assumption that uncertainties are Gaussian and independent, assumes the following form:

$$\ln(\mathcal{L}) = -0.5\sum_i \ln\left(2\pi\sigma_i^2\right) - 0.5\sum_i \frac{(f_{\lambda,i} - \mathcal{M}_i(\theta))^2}{\sigma_i^2}, \tag{3.3}$$

If we have both spectroscopic and photometric data, the likelihood is computed for both components, with the difference that in the case of $\mathcal{L}_{spec}$ the summation on Eq. 3.3 will take into account N_{pix} elements, corresponding on the number of pixels of the spectrum, while in the case of $\mathcal{L}_{phot}$ will include the N_{phot} photometric data.
The total likelihood, then, is given by the product of the two likelihood or, equivalently, by the sum of the logarithms:

$$ln(\mathcal{L}_{tot}) = ln(\mathcal{L}_{spec}) + ln(\mathcal{L}_{phot}). \tag{3.4}$$

Two correction components need to be considered to avoid introducing biases into the analysis. The first concerns the fact that, during the spectrum extraction process,

certain effects related to extraction and calibration may occur, potentially affecting both the shape and the normalization of the spectrum. The most significant of these is due to *extraction loss*, which arises because the spectrum is obtained through a slit that does not encompass the entire galaxy. Consequently, the measured flux is smaller than the intrinsic one. Furthermore, absolute flux calibration and other data reduction processed may lead to possible modifications of the spectral shape. For this reason, we introduce a *Chebyshev polynomial*, which allows us to adjust the shape and normalization of the spectroscopy so that it matches the photometry, which in turn accounts for the total flux of the galaxy.
The second factor relates to the fact that the uncertainties associated with the spectroscopic and photometric data may be either overestimated or underestimated. To address this, a scaling factor is often introduced to ensure that the model yields χ^2 values that are not systematically too large or too small.

3.1.2 Generating the theoretical models

To reproduce the spectrum f_λ, the model must include the following main components:

- a model of *simple stellar population* SSP(λ, a_i, Z), which depends on the wavelength λ, the age (a_i) of the stellar population, the metallicity Z, and the adopted IMF. A SSP represents the fundamental building block used to construct more realistic star formation histories. Different models and prescriptions exist for generating synthetic spectral models based on SSPs, as it will be described across this work;

- *star formation history*, SFR(t), which is composed of a sum over one or more SFH components;

- the *transmission function of the ionized ISM*, T^+(age, λ), as described in (Charlot & Longhetti, 2001). It includes absorption, line emission, ionized continuum emission, and emission from warm dust within H II regions. For the purpose of this work, we decided not to consider this component since we are fitting massive and passive galaxies that have been carefully selected to ensure the absence of any ongoing star formation (see Sect. 2.2.1);

- the *transmission function of the neutral ISM* T^0(age, λ), due both to the emission and absorption of the dust. In the code, several models are implemented, including Calzetti et al. (2000a), Cardelli et al. (1989), and Charlot & Fall (2000). This component is the one we will refer to as *dust*.

These four ingredients are then combined to derive the galaxy luminosity according to the following relation:

$$L_\lambda(\lambda) = \sum_{j=1}^{N_c} \sum_{i=1}^{N_a} \mathrm{SFR}_j(t_i)\ \mathrm{SSP}(a_i, \lambda, Z_j)\ T^+(a_i, \lambda)\ T^0(a_i, \lambda)\ \Delta a_i, \tag{3.5}$$

where N_c is the number of components, and N_a is the number of age bins (a_i) into which the star formation history of the galaxy is decomposed. Here, t_i is defined as $t_i = t(z_{obs}) - a_i$, where z_{obs} is the redshift at which the object is observed, representing the age of the Universe at the time of observation.

Once the rest-frame luminosity is known, `Bagpipes` converts it into an observed flux through the following equation:

$$f_\lambda^{obs}(\lambda_{obs}) = \frac{L_\lambda(\lambda)}{4\pi D_L(z_{obs})^2(1+z_{obs})} T_{IGM}(\lambda, z_{obs}). \tag{3.6}$$

Here $D_L(z_{obs})$ is the luminosity distance at redshift z_{obs}, while $T_{IGM}(\lambda, z_{obs})$ is the transmission curve of the intergalactic medium.

In particular, to better understand the methods used in this work, we will describe each of these components in more depth.

Stellar population synthesis models

`Bagpipes` does not implement SPS models internally. Instead, it is designed to utilize pre-computed models, which are provided in the form of grids of SSP spectra spanning a range of ages and metallicities.

In its original implementation, `Bagpipes` adopts the 2016 version of the Bruzual & Charlot (2003) models (hereafter `BC16`). These updated models incorporate the Medium-resolution Isaac Newton Telescope Library of Empirical Spectra (`MILES`; Falcón-Barroso et al., 2011b) for the UV-optical wavelength range, representing a significant improvement over earlier versions. The SSP models are constructed assuming a Kroupa (2001) IMF. At present, `Bagpipes` assumes scaled solar abundances for all models and does not allow for variations in elemental abundance patterns (e.g., α-enhancement), which is one of the goals of future FSF analysis.

When a given set of SPS models is loaded into `Bagpipes`, the spectra are resampled in age using a weighted summation technique to produce a uniform grid of ages, a_i, ranging from $\log_{10}(a_i/\mathrm{Gyr}) = 6.0$ to 10.2. The default spacing of this grid is 0.1 dex in logarithmic age, resulting in a total of $N_a = 43$ age bins.

Star formation histories

Another key choice when constructing the model is the functional form of the SFH. In `Bagpipes`, star formation histories are constructed from one or more components, denoted

as j, each of which defines a specific functional form for the star formation rate as a function of time, $\mathrm{SFR}_j(t)$. The total star formation rate at any given time is calculated by summing over all components:

$$\mathrm{SFR}(t) = \sum_{j=1}^{N_c} \mathrm{SFR}_j(t). \tag{3.7}$$

`Bagpipes` allows the user to specify an arbitrary number of SFH components, each with its own functional form. The currently implemented options are:

- ⋆ Delta function;
- ⋆ Constant;
- ⋆ Exponentially declining;
- ⋆ Delayed exponentially declining;
- ⋆ Log-normal;
- ⋆ Double power-law;
- ⋆ Custom (user-provided array of SFR values).

In this project, we always assumed a delayed exponentially declining SFH, described by the following equation:

$$\mathrm{SFR}(t) \propto \begin{cases} (t - T_0)e^{-\frac{t-T_0}{\tau}}, & t > T_0 \\ 0, & t < T_0 \end{cases} \tag{3.8}$$

where T_0 is the age of the Universe at the onset of star formation activity, and τ is the characteristic timescale of star formation.
We decided to adopt this type of SFH (as done by several works, see, e.g., Citro et al., 2017; Carnall et al., 2018; Tomasetti et al., 2023) because it provides an appropriate description for passive galaxies, which are characterized by a short and intense period of star formation followed by rapid quenching. Such a functional form is in particular well-suited to reproduce the evolutionary history of the galaxies selected as CC, because, as shown in Sect. 2.2.1, they have been specifically selected to show no sign of ongoing star formation. Indeed, there is a large literature supporting the scenario in which these systems have built up their mass very rapidly ($\Delta t < 0.3$ Gyr Thomas et al., 2010; McDermid et al., 2015; Citro et al., 2017; Carnall et al., 2018) and at high redshifts ($z > 2-3$ Daddi et al., 2005; Choi et al., 2014; McDermid et al., 2015; Pacifici et al., 2016; Carnall et al., 2018,

2019), having quickly exhausted their gas reservoir and being evolving passively since then.

Dust attenuation and emission

Dust attenuation in `Bagpipes` is designed in a modular fashion such that different dust curves may be easily implemented. Each dust attenuation curve takes the overall functional form:

$$\log_{10} T_0(a_i, \lambda) = \begin{cases} -\dfrac{0.4\,\epsilon\,A_V\,k(\lambda)}{R_V}, & a_i < a_{BC} \\ -\dfrac{0.4\,A_V\,k(\lambda)}{R_V}, & a_i > a_{BC} \end{cases} \tag{3.9}$$

where a_{BC} is the lifetime of stellar birth-clouds, A_V is the attenuation in the V band (~ 5500Å) in magnitudes, ϵ is a constant which can be used to control the extra attenuation towards H II regions and $k(\lambda)$ and R_V are specific to the dust model being used. Among the models implemented and listed in Table 3.1 particular emphasis will be given to the one suggested by (Calzetti et al., 2000a), where it is possible to find the form $k(\lambda)$ and the value of R_V.

Velocity dispersion and spectral sampling

`Bagpipes` is designed to fit both spectroscopic and photometric data, requiring that the effects of velocity dispersion ($\sigma_{\rm vel}$) are incorporated into its modelling to accurately reproduce observed spectral features. To achieve this, the code converts the wavelength sampling of all input SPS models to a constant spectral resolution defined as $R = \lambda/\Delta\lambda$. Then by default, `Bagpipes` applies a low resolution of $R = 100$ in wavelength regions used solely for calculating photometric outputs, while a higher resolution of $R = 1000$ is adopted in regions generating the output spectrum. The high-resolution spectral region is subsequently convolved with a Gaussian kernel in velocity space to simulate the broadening effects of velocity dispersion within the galaxy, which is assumed to affect the stellar and gas components equally.

In the modelling of the spectrum, along with the physical components describing the emission of the galaxy, `Bagpipes` allows the inclusion of two additional components that account for possible effects arising from non-physical, primarily observational or instrumental, reasons. As already discussed above, in general, they perturb the spectrum either additively, referred to here as *offset noise*, or multiplicatively, included as a *calibration offset*. In the first case, the inclusion of a noise parameter allows the model to modify the error on the spectrum, relaxing the assumption that the uncertainties on the observational data are independent, perfectly known, and Gaussian-distributed. There are, indeed, several reasons why this assumption might not hold, such as imperfect sky subtraction. In the second case, the spectrum is perturbed through a polynomial function of wavelength,

specifically defined by second-order *Chebyshev polynomials*. The introduction of this parameter allows the model to correct for potential issues related to spectral calibration, such as misalignments between the spectroscopic and photometric data.

In Table 3.1 we provide a description of all the components that can be set in `Bagpipes` and their physical interpretation. Each of the components listed is optional, except for the SFH; this means that we can choose whether or not to include them in the model.

Component	Description	Options
SFH	Star Formation History: variation of the SFR as a function of cosmic time.	single burst, delayed, double-power-law...
dust *	Emission and absorption by dust in the neutral ISM.	(Calzetti et al., 2000a), (Cardelli et al., 1989)
nebular *	Absorption, line emission, and continuum emission from the ionized ISM.	(Charlot & Longhetti, 2001)
noise *	Modifies the error on the spectrum to account for possible underestimation.	White or correlated noise; (Carnall et al., 2019)
calib *	Perturbs the spectrum with a wavelength-dependent function to account for possible calibration issues.	Chebyshev polynomials

Table 3.1: Summary of the components used to build the spectrum model in `Bagpipes`. Optional components are indicated with *.

3.1.3 Assessing the degeneracies between parameters

One of the main challenges in determining the physical properties of a galaxy from its SED arises from the presence of strong degeneracies among the parameters that shape the observed spectrum. Different combinations of stellar age, metallicity, SFH, and dust content can produce remarkably similar spectral features, thereby complicating the interpretation of observational data. Among the primary sources of degeneracy, the most prominent is the well-known age–metallicity degeneracy (Worthey, 1994; Ferreras et al., 1999). Additional sources of degeneracy include the coupling between a galaxy's age and its SFH (Gavazzi et al., 2002), as well as the effects of dust attenuation. The latter, however, is generally negligible for carefully selected passive galaxies, where dust contamination is minimal (Calzetti et al., 2000b).

To explore the impact of these parameters, we generated a set of theoretical models, varying one parameter at a time while keeping the others fixed. Fig. 3.1 illustrates how the main physical parameters that define a galaxy's SED, e.g., stellar age, metallicity, dust attenuation, and the star formation timescale τ, affect the shape of model spectra.

One of the most evident effects arises when varying the stellar age while keeping all other parameters fixed. As the stellar population becomes older, the continuum progressively reddens, and the strength of certain absorption features increases, whereas the hydrogen lines become less prominent. This behaviour reflects the growing dominance of cooler and more evolved stars. Varying the metallicity produces a similar reddening of the spectrum, since a higher metal content enhances line blanketing in the blue and ultraviolet regions. The similarity between the spectral responses to age and metallicity variations gives rise to the well-known age–metallicity degeneracy. Regarding the role of dust attenuation, increasing the dust content suppresses the blue part of the spectrum, mimicking the reddening produced by either higher age or metallicity. This introduces an additional source of degeneracy in SED fitting. Finally, varying the characteristic star formation timescale (τ) shows that shorter τ values, corresponding to more rapid star formation episodes, lead to spectra dominated by redderer continuum (older stellar populations), whereas longer τ values preserve a stronger contribution from young, blue stars.

These examples highlight how different physical mechanisms can produce comparable spectral signatures, making it difficult to uniquely constrain galaxy properties from photometric or low-resolution spectral data alone. Breaking these degeneracies requires high-quality spectra and diagnostics specifically sensitive to individual parameters. As shown by Tomasetti et al. (2023), a wide spectral coverage can significantly reduce these degeneracies. However, such coverage was not available for the BOSS data used in this work, as is evident in Fig. 2.1.

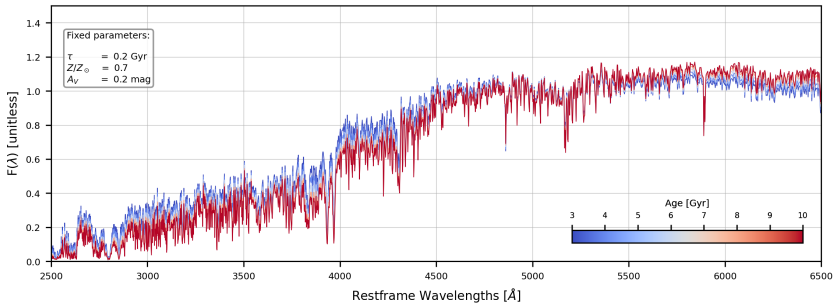

(a) Spectra models varying age

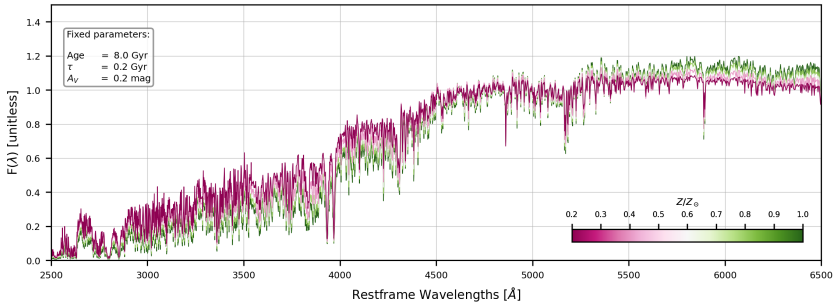

(b) Spectra models varying metallicity

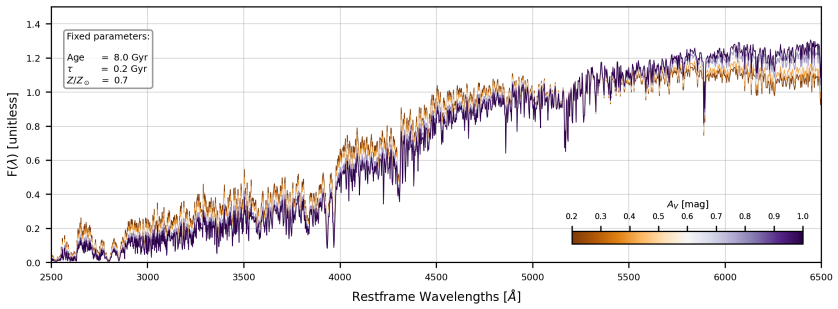

(c) Spectra models varying dust

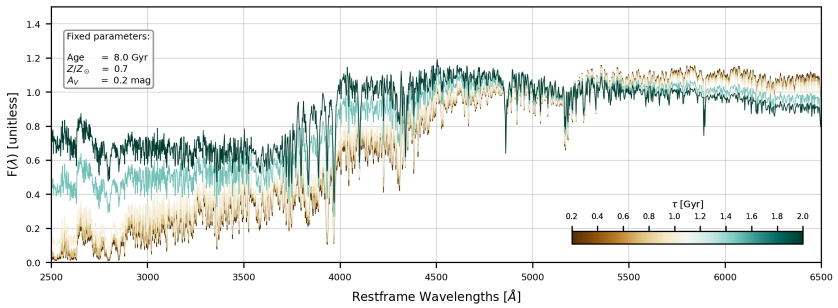

(d) Spectra models varying τ

Figure 3.1: Model spectra generated with `Bagpipes` to illustrate the effects of varying key parameters: age, metallicity, dust attenuation, and star formation timescale τ. All models are based on a common initial configuration (indicated in the top-left of each panel), with only one parameter allowed to vary at a time.

3.2 Full spectral fitting in SDSS BOSS

In Chapter 2, we described the procedure used to identify a golden sample of CC galaxies from the BOSS data, consisting of the most massive and passive systems with the highest SNR. The next step involved reconstructing the physical properties of the CC sample, such as stellar age, metallicity, and stellar mass. This was achieved by performing full spectral fitting on the combined spectroscopic and photometric data with the `Bagpipes` code.

To optimally reproduce the observed data, several tests were carried out using different model configurations. A major challenge in this process was the presence of degeneracies among several parameters, such as age, τ, A_V, and metallicity (see Sect. 3.1.3). The severity of these degeneracies strongly depends on factors such as the SNR, spectral resolution, and wavelength coverage of the data. Therefore, beyond exploring different priors on the model parameters, it was also necessary to account for these effects by configuring the fitting procedure to rely primarily on the most informative portions of the spectrum.

3.2.1 Exploring the Full Spectral Fitting setup

For each galaxy analyzed through full spectral fitting, we loaded the optical spectrum and the corresponding SDSS photometry in the five *ugriz* bands.

When loading the spectra, a series of masks was applied to exclude problematic wavelength regions from the fitting. We removed regions affected by strong sky residuals (e.g., around 5577 Å, 6300 Å, and 5890 Å) as well as those containing prominent stellar absorption features that could bias the continuum fitting (Na D and Mg b bands).

Furthermore, the analysis was restricted to a wavelength range that avoids the initial and final parts of the spectra, where the noise becomes significant toward the blue and red edges. In addition, only pixels with positive inverse variance were retained in the final mask. The photometric fluxes considered were derived from SDSS Petrosian magnitudes and converted into μJy units following standard relations. Their uncertainties were propagated from the magnitude errors, and a maximum SNR of 20 was imposed to avoid over-weighting the photometric points in the joint fit. As already anticipated, to properly configure the model components in `Bagpipes`, preliminary tests were conducted to explore the influence of different prior assumptions on key physical parameters such as stellar age, metallicity, SFH, and dust attenuation. These tests were carried out on a small sample of seven galaxies, aimed at examining the impact of different parameter configurations and prior constraints on the resulting fits. We analyzed the corresponding χ^2_{red} values and posterior distributions (via corner plots) to assess the goodness of fit and the behaviour of the parameters. The first tests were performed using the standard

`Bagpipes` setup, including the cosmological prior (which prevents stellar ages from exceeding the age of the Universe). In these initial runs, the spectra were fitted over a wide wavelength range (3600–8000 Å), without including the photometric data. To mitigate and break the degeneracies already discussed in Sect. 3.1.3, several alternative configurations were explored, involving the implementation of physically motivated priors on the fitted parameters, which are listed below:

- We tried to change the constraints on metallicity. The first critical point emerged from the fact that allowing it to vary uniformly up to $1.5\,Z_{\odot}$, the results often favoured unphysically high values due to the degeneracies discussed above. We therefore limited the upper bound to $0.7\,Z_{\odot}$ and $1.0\,Z_{\odot}$ in separate tests (following the constraints obtained on SDSS BOSS CC by Moresco et al., 2016), observing that lower metallicity limits led to systematically older best-fit ages. We also tested the effect of adopting a logarithmic prior (`log10`) instead of a uniform one, but it did not help to mitigate the effect of metallicities on the prior.

- We explored different upper limits for the SFH timescale parameter τ (0.15, 0.5, and 2.0 Gyr). The main effect was a correlated variation of the best-fit age, clearly revealing a very strong age–τ degeneracy.

- We varied the constraints on dust attenuation, testing upper limits of $A_V < 1.0$ and $A_V < 0.5$. However, the impact on the fits was found to be negligible.

For some objects, the results of these tests led to unrealistically low stellar ages, indicating potential issues with the fitting configuration. To address this, we took into account the fact that the spectral resolution of the models implemented in `Bagpipes` varies with wavelength and therefore we took the conservative choice of limiting the range of the fitted spectra between 3500–6500 Å.
However, as shown in Fig. 3.2, this will have an impact on the analysis since with increasing redshift the region of interest for the fit results inhomogeneous.

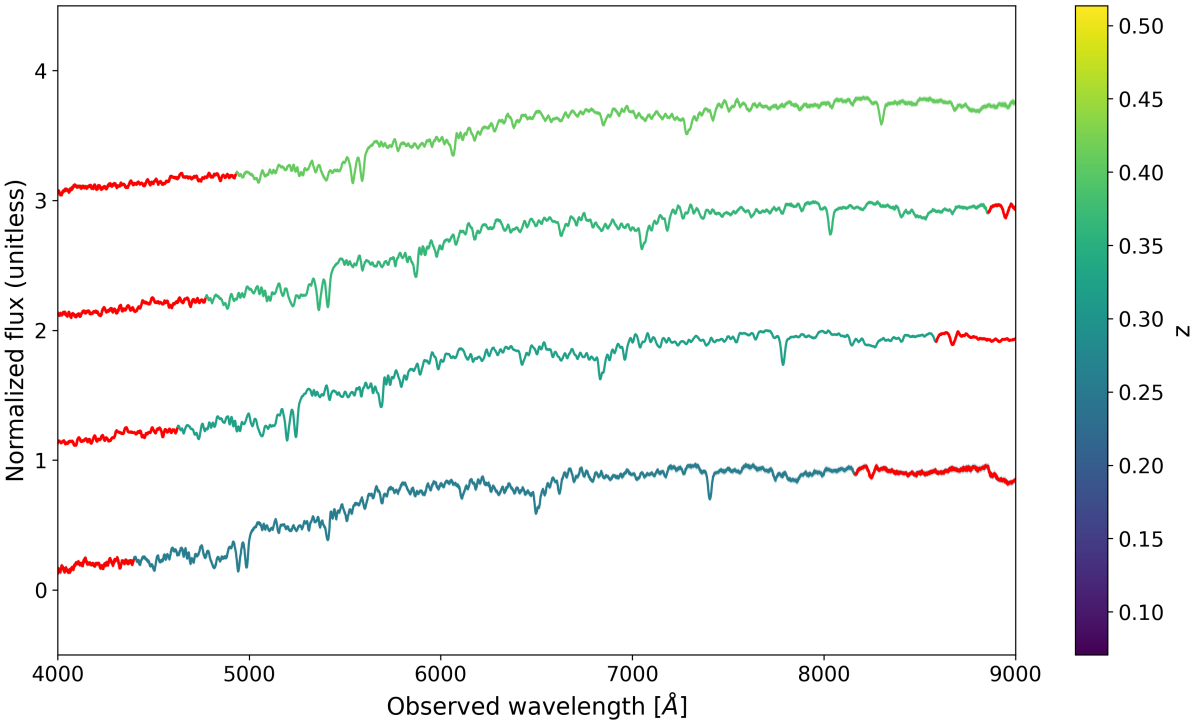

Figure 3.2: Stacked spectra of the CC sample in different redshift bins, color-coded according to the mean redshift of each bin. The shaded red regions mark the rest-frame wavelength intervals outside 3500–6500 Å, which were excluded from the full spectral fitting with `Bagpipes`.

In addition, we included the available photometry, even if its wavelength coverage was limited (Fig. 2.1), as this additional information could help constrain the models and reduce the degeneracies observed in the purely spectroscopic fits.

The inspection of the fits revealed the critical point represented by the degeneracies present within the parameters. Indeed, different combinations of parameters can produce spectra that are virtually indistinguishable within 1σ over the considered wavelength range, as illustrated in Fig. 3.3. This figure highlights the severity of the degeneracies, showing that the same spectrum can be reproduced by different combinations of key parameters such as age, τ, dust attenuation, and metallicity. Fig. 3.4 shows that extending the wavelength coverage toward the UV and IR could help alleviate these degeneracies. However, in our case the photometric data alone are of limited help, since, as shown in Fig. 2.1, they do not significantly extend the range of observed wavelengths.

These considerations led us to conclude that, to address this problem, the most viable path would be to adopt an approach commonly used in previous studies (e.g. de Graaff et al., 2025), by imposing physical upper limits on certain parameters, including metallicity, dust attenuation, and star formation rate supported by a robust and well-founded literature. These limits are justified by the physical properties predicted by the formation and evolution scenario of the objects under analysis, as described in Sect. 1.2.4.

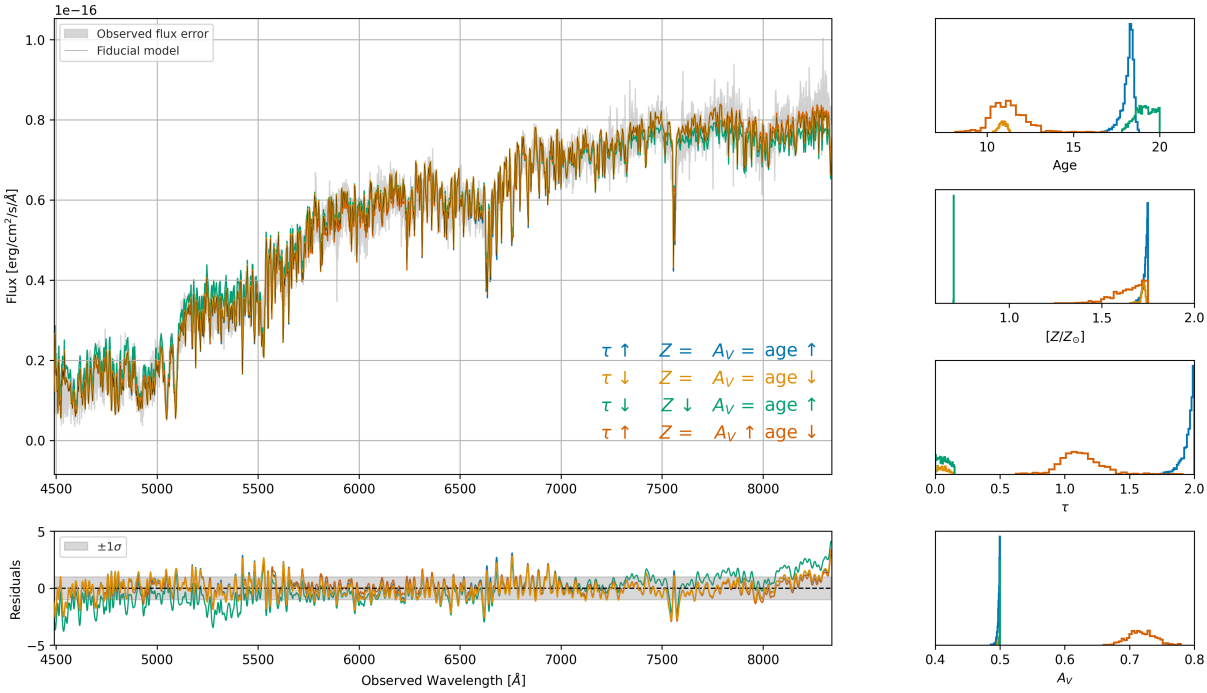

Figure 3.3: Zoomed-in fitted spectrum. *Left:* the upper panel shows the observed spectrum of one of the analyzed objects, compared with best-fit spectra obtained for illustrative purposes using different parameter combinations in `Bagpipes`, shown in various colors. The fiducial fit is shown in black. The lower panel displays the residuals, with the gray shaded area representing the 1σ observational uncertainty. *Right:* marginalized posterior distributions for the fitted parameters (τ, Z, A_V, and age).

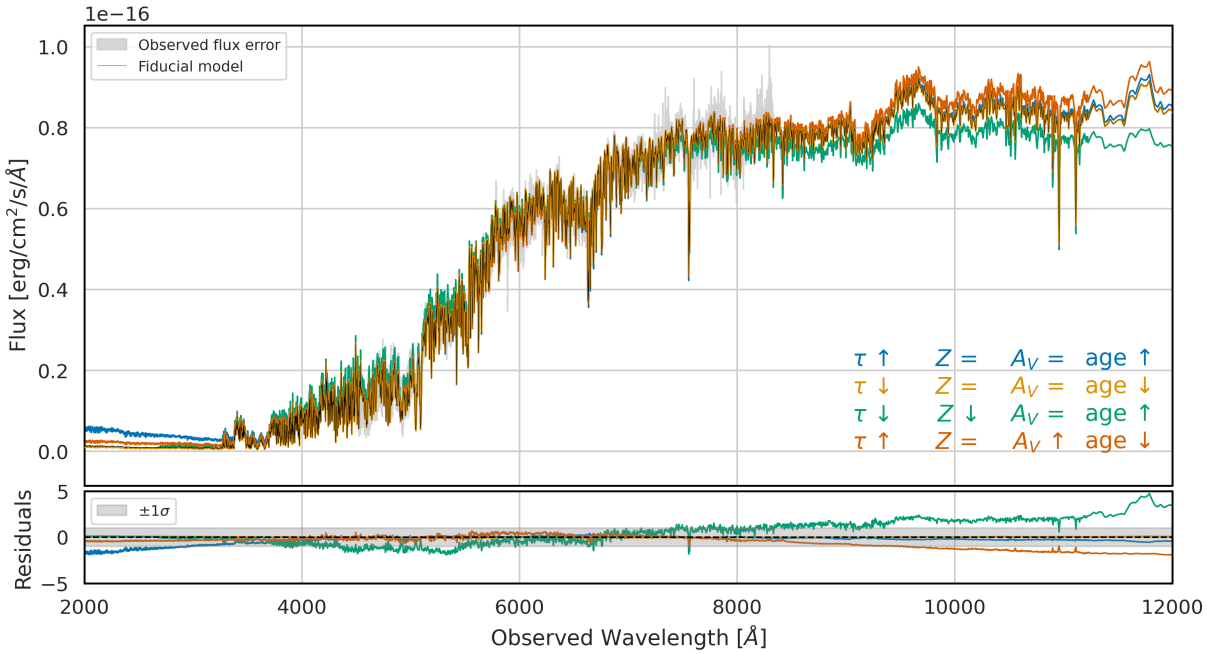

Figure 3.4: Same as Fig. 3.3 but over a wider wavelength range; from the figure it is clear how, with an extended coverage, it is possible to distinguish models with different parameters.

3.2.2 Tests on the golden sample and final setup

In order to proceed with the identification of the best setup to fit our galaxies, we analyzed several configurations, applied to the golden sample of CC, with the only difference in the choice of the upper limit on the prior for τ, by running the code multiple times. The analysis was conducted both in the case of the standard `Bagpipes` implementation, which uses the cosmological prior, and in a modified version where this prior was removed.
In particular, in the latter case, several constraints for the upper limit of τ (0.75, 1.0, 1.5, 1.75) were explored.

Configuration	**Range of τ**	**Cosmo prior**	**Good fits**
baseline	(0, 0.75)	OFF	69
baseline	(0, 0.75)	ON	67
baseline	(0, 1)	OFF	68
baseline	(0, 1.5)	OFF	67
baseline	(0, 2)	ON	68
baseline	(0, 2)	OFF	73

Table 3.2: Summary description of the different runs computed for the "golden sample" of the 84 galaxies. The last column represents the number of galaxies remaining after the visual inspection.

For the purposes of this work, we focused on the age–redshift relation, which was analyzed for each run described in Table 3.2 and shown in Fig. 3.5. Examining these plots, it is evident that the estimates of the absolute ages vary depending on the constraints applied to τ. In particular, the presence of a cosmological prior appears to be problematic with the aim of a cosmological application, as the corresponding age–redshift relation is found to strictly follow the imposed prior, as evident from Fig. 3.5. When this prior is removed and the age is allowed to vary freely between 0 and 20 Gyr, some fits yield ages exceeding the age of the Universe predicted by the standard ΛCDM model. Despite this, the global trend provides remarkable results, with a redshift evolution that remains consistent: ages decrease with increasing redshift. This confirms what was already inferred from the analysis of specific spectral features, and is in impressive agreement with the cosmological model despite having removed the cosmological prior.

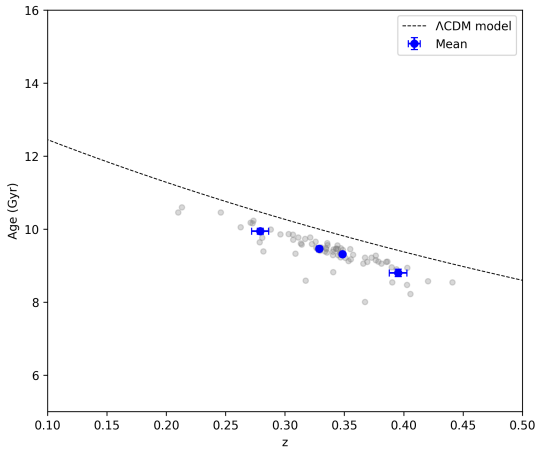

(a) Fixed cosmology, $\tau < 2.0$ Gyr

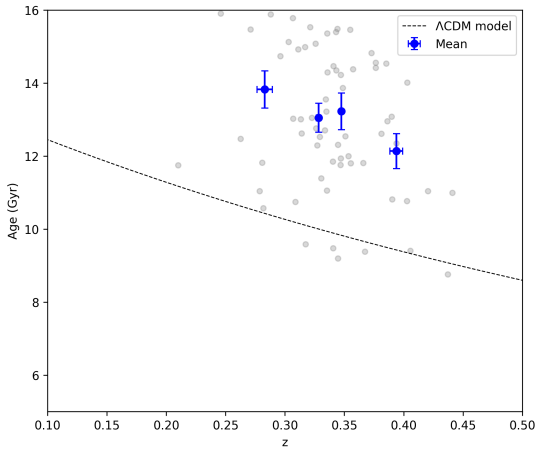

(b) Free cosmology, $\tau < 2.0$ Gyr

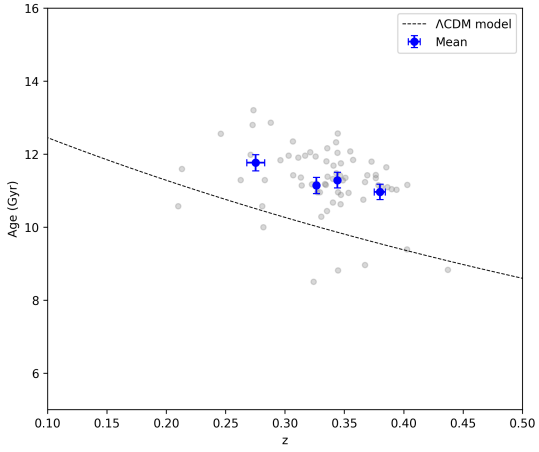

(c) Free cosmology, $\tau < 1.5$ Gyr

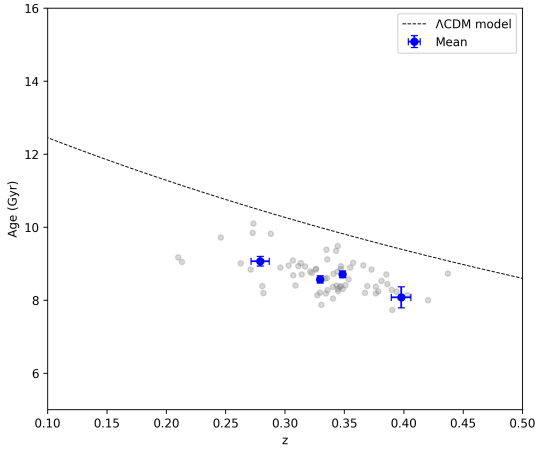

(d) Free cosmology, $\tau < 1.0$ Gyr

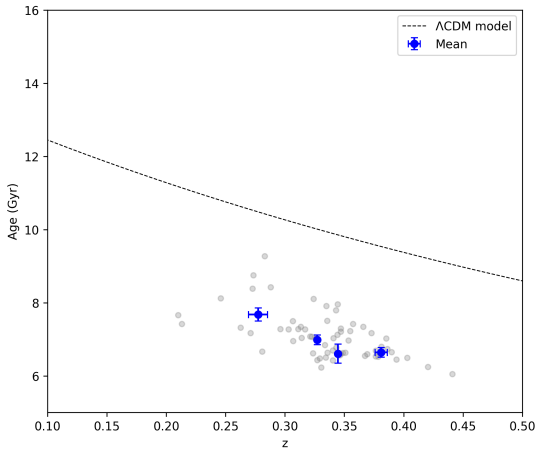

(e) Fixed cosmology, $\tau < 0.75$ Gyr

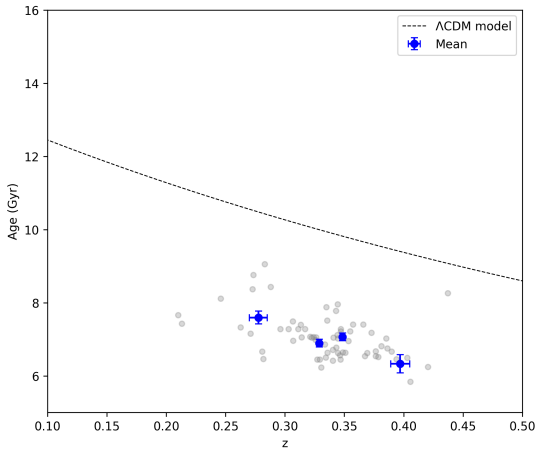

(f) Free cosmology, $\tau < 0.75$ Gyr

Figure 3.5: Age–redshift diagrams for the selected passive sample (grey dots). Blue dots indicate the mean age within each redshift bin. Ages were derived by fitting the spectra and photometry using `Bagpipes`. Results are shown for each trial, employing different constraints on τ, some with and some without the cosmological prior.

This represents a crucial point: even though, due to data limitations and parameter degeneracies, we cannot robustly constrain the absolute ages of these objects, their relative ages remain consistent across all tests. This demonstrates the strength of the CC selection and method, which, being based on differential age measurements, remains a valid and powerful cosmological tool.

These tests led us to adopt the final setup, $\tau < 1$ Gyr, a prior that is physically well supported by the literature for this population of objects. Remarkably, we note that with this prior, despite not having assumed any cosmological constraint, almost all derived ages remain below the expected ages at a given redshift. Following these tests, a specific configuration was selected as the baseline for our analysis:

- delayed SFH;
- dust attenuation described by (Calzetti et al., 2000a);
- fixed redshift to the spectroscopic redshift values provided by the BOSS survey;
- photometry provided by the SDSS survey, which follows the system *ugrzi*. As described in Sect. 3.1.2, to address the possible misalignment between photometric and spectroscopic data, we need to introduce a calibration component, which allows the model to correct for potential issues related to spectral calibration.

The values and priors for each parameter are reported in Table 3.3.

Component	Parameter	Symbol [unit]	Range	Prior	Hyperparameters
Global	velocity dispersion	σ_{vel} [km/s]	(250, 450)	uniform	–
	age	age [Gyr]	(0, 20)	uniform	–
SFH	formed mass	$M_{formed}/M_{\odot}$	(1, 10^{13})	uniform	–
	metallicity	$Z/Z_{\odot}$	(0, 1.75)	uniform	–
	SF duration	τ	(0, 1)	uniform	–
Dust	V-band attenuation	A_V [mag]	(0, 0.5)	uniform	–
Calib	first order	P_0	(0.1, 3.0)	Gauss	–
	second order	P_1	(-1, 1)	Gauss	$\mu = 0,\ \sigma = 0.25$
	third order	P_2	(-1, 1)	Gauss	$\mu = 0,\ \sigma = 0.25$
Noise	white noise	n	(1, 10)	uniform	–

Table 3.3: Summary of baseline configuration parameters and priors.

Among the different factors considered, a key aspect to highlight is that, with this configuration, galaxy ages were allowed to span up to 20 Gyr independently of redshift, thanks to a modification implemented in the `Bagpipes` code, previously tested and validated in Jiao et al. (2023) and Tomasetti et al. (2023). The removal of the cosmological prior on ages, typically adopted in galaxy evolution studies, ensures that the results are independent of any specific cosmological model.

Assessing the quality of the fit

The fitting procedure performed with `Bagpipes` produces as output the probability distributions for each fitted parameter, together with the corresponding 16th, 50th, and 84th percentiles, as well as the resulting photometry. These outputs allow us the reconstruction of the best-fit spectrum (shown in Fig. 3.6), along with the corresponding corner plot (Fig. 3.7), which displays both the posterior probability distributions of each parameter and their joint distributions. This representation enables visual inspection of the correlations among parameters and facilitates the identification of possible degeneracies.

The process of full spectral fitting does not always converge to robust results. In some cases, parameters may fail to converge, or the resulting spectra and photometry may not match the observed data. In such cases, the results cannot be considered valid. Therefore, at the end of each run, a visual inspection of the corner plots and the resulting best-fit spectra was performed for each galaxy to discard *bad fits*. In general, a fit was classified as poor if any of the following conditions were met:

- the posterior probability distribution of one or more parameters exhibited anomalies, such as multimodal profiles or an inadequate sampling of the parameter space that prevented the identification of a well-defined best-fit value;
- the resulting model spectrum showed clear discrepancies with respect to the observed data;
- the posterior distribution of the age parameter converged toward the boundary of its allowed range. This criterion, however, was not applied to parameters such as metallicity and τ, which, as discussed previously, were constrained within specific intervals to mitigate degeneracy effects.

For a sample of 84 galaxies, the size of our golden sample, a visual inspection is still feasible. However, as the sample size increases, it becomes impractical to perform a visual inspection to identify and discard potential outliers. Therefore, an automated procedure was implemented to remove outliers. This procedure relied on evaluating the $\chi^2_{\rm red}$ from the fit to the spectroscopic data, as well as comparing the best-fit velocity dispersion with the corresponding values catalogued in BOSS. Specifically, we retained only those objects with $0.8 < \chi^2_{\rm red} < 2.0$, and excluded galaxies for which either the best-fit velocity

dispersion or the BOSS catalogued value exceeded 440 km s^{-1}, since such high velocity dispersions are not physically plausible.

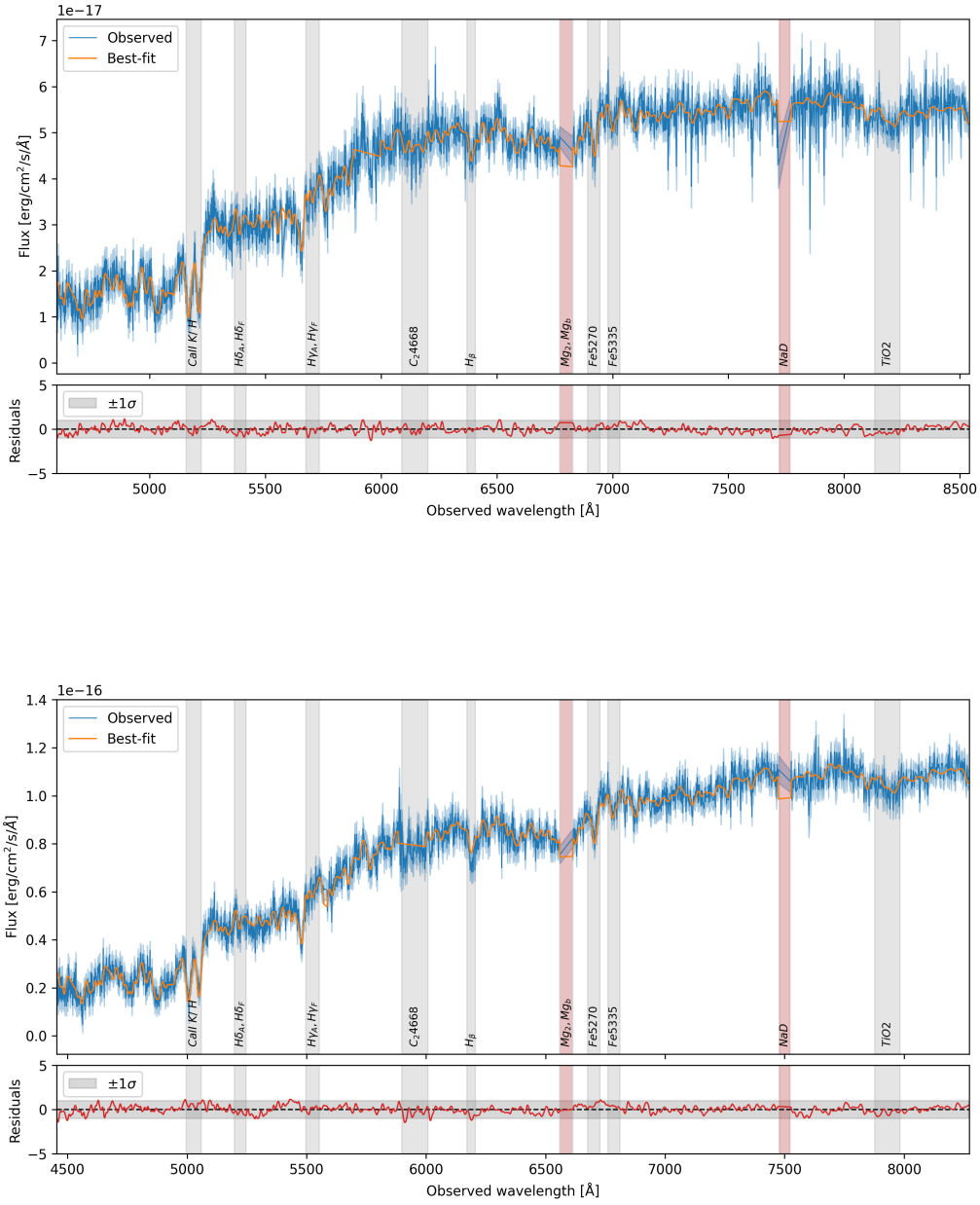

Figure 3.6: Examples of best-fit spectra for two of the analyzed galaxies. The shaded regions correspond to the wavelength ranges defined by the Lick indices, while the red shaded areas mark the spectral bands that were masked during the fitting process.

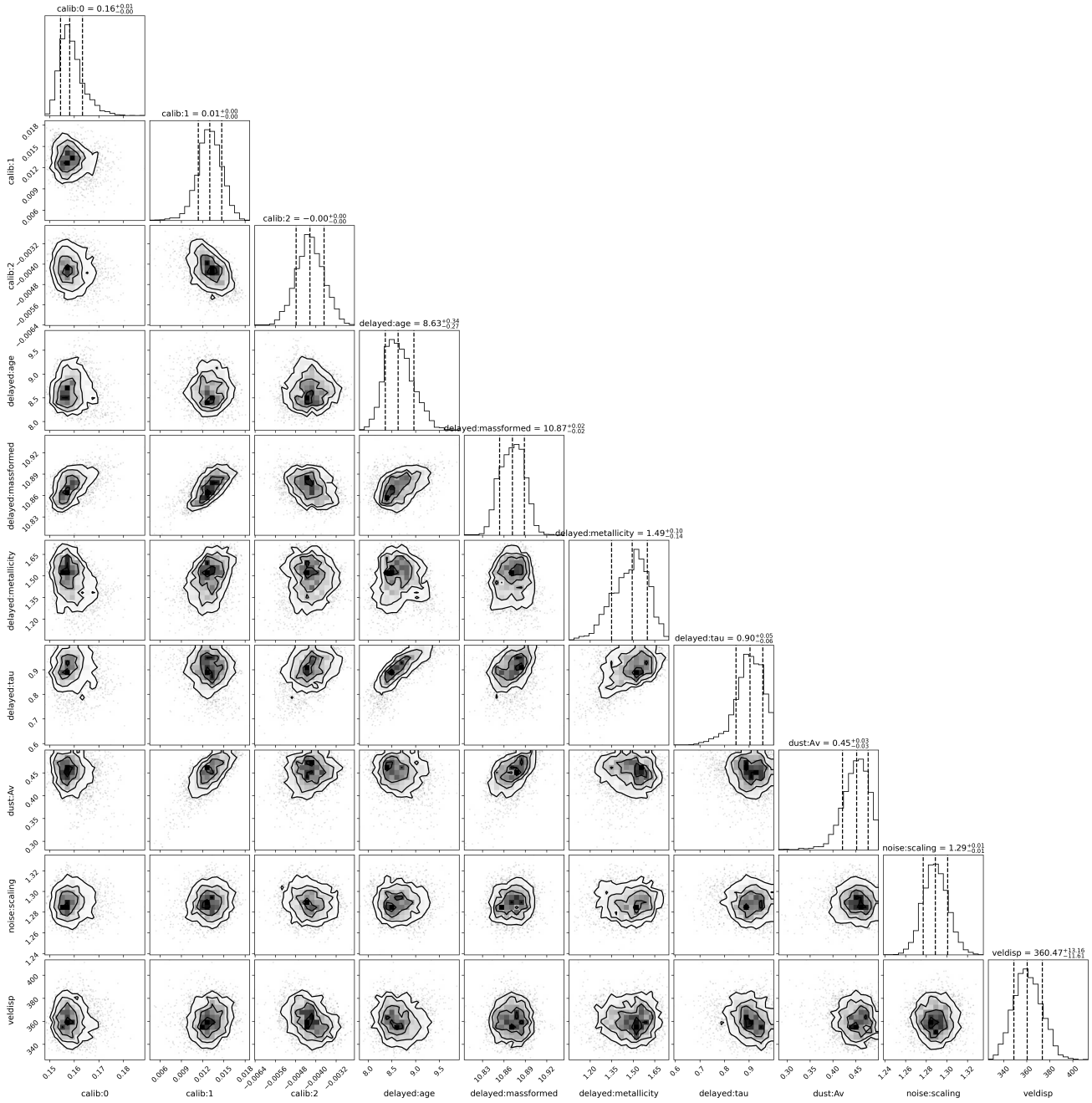

Figure 3.7: Example of a corner plot. The curves on the joint posteriors and the dashed lines on the marginalized posteriors represent the 16th, 50th and 84th percentiles.

Best-fit Parameters

After applying a visual selection, we analyzed the physical properties of the remaining galaxies in our golden sample by examining the output values of each fitted parameter. In particular, the median of the posterior distribution was adopted as the best-fit value for each parameter.

The distributions show that the CC sample exhibits physical properties consistent with the criteria applied during the selection:

- Very massive objects, as expected for passively evolving galaxies. In particular, the parameter used in `Bagpipes` is the total stellar mass formed by the galaxy from its formation up to the time at which it is observed:

$$M_{\rm form} = \int_0^t \mathrm{SFR}(t')\, dt'. \tag{3.10}$$

- Super-solar metallicities, in agreement with the results found by Moresco et al. (2016) for very massive galaxies in the redshift range $\sim 0.2 - 0.4$.

- Physically motivated constraints necessary to address the problem of degeneracies. Given that for this class of objects we expect a very short star formation phase (Thomas et al., 2010; Citro et al., 2017), along with a limited amount of dust, the choice of imposing upper limits on the priors related to τ and A_V is justified and explains the distribution of the resulting best-fit parameters.

3.3 Results

At this stage, we have established a baseline configuration, identified as the optimal setup for performing full spectral fitting on this type of data and validated on the golden sample. This configuration is now applied to a more extended sample, drawn from the preliminary selection described in Sect. 2.2.5, prior to the D4000-based selection.

3.3.1 Deriving the Age–z relation

The same analysis described in detail in Sect. 3.2.2 was carried out on a larger sample of 900 CCs. The increased sample size provided significantly improved statistics, allowing for more precise estimates when computing the mean values derived from the FSF process. As discussed previously, in this case it was not possible to perform a visual inspection to exclude poor fits; therefore, the automated procedure described earlier was applied.

For this sample, we explored again the two configurations with $\tau < 1.0$ and $\tau < 2.0$, both without applying the cosmological prior, as summarized in Table 3.4.

Configuration	**Range of τ**	**Cosmo prior**	**N° objects**
baseline	(0, 1)	OFF	837
baseline	(0, 2)	OFF	840

Table 3.4: Summary of the different runs computed for the *extended* sample of 900 galaxies.

This analysis once again confirmed the clear presence of degeneracy between the parameters τ and age, and revealed the expected decreasing trend of age with redshift, in agreement with the ΛCDM model as shown in Fig. 3.8. It is visually remarkable that despite an offset in age, the slope of the relation (hence the relative ages) appears fairly consistent, as it will be further proved and confirmed in Sect. 4.2.

This is an important result for the CC method, since it is purely based on the differential age evolution of the population, and not on the absolute ages derived.

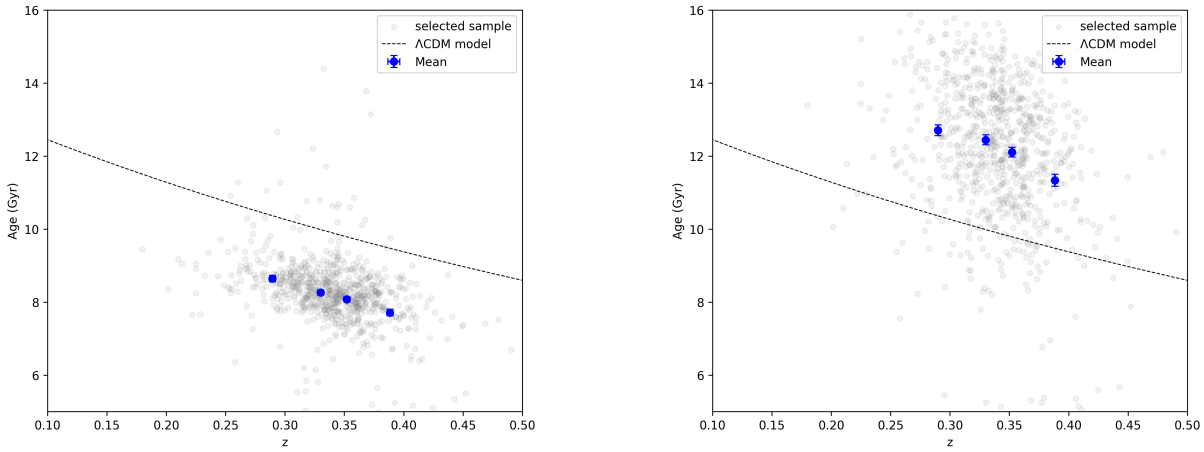

(a) Free cosmology, $\tau < 1.0$

(b) Free cosmology, $\tau < 2.0$

Figure 3.8: Age–redshift diagrams for the passive sample of 900 galaxies (grey dots). Blue dots indicate the mean age within each redshift bin. Ages were derived by fitting spectra and photometry with `Bagpipes`. Results are shown for each trial, using different constraints on τ.

The age estimates obtained from the FSF with the configuration $\tau < 1$, which serves as our baseline, are those used to apply the CC method in order to derive a new estimate of $H(z)$, as described in Sect. 3.3.3. Before proceeding with this, however, we explored different binning choices.

3.3.2 Investigating the impact of the binning choices

To mitigate the effects of potential variations in the star formation histories of the galaxies in this extended sample, we explored the impact of further dividing the data not only into redshift bins but also into bins of velocity dispersion σ (or, equivalently, stellar mass).

Initially, within each redshift bin, galaxies were subdivided into four σ bins based on the quartiles of the velocity dispersion distribution. This diagram, shown in Fig. 3.9c, reveal a clear separation in stellar mass among the galaxies; however, significant fluctuations within each σ bin are also evident. Such oscillations could represent a problem when applying the CC method to individual σ bins, since the main limitation arises from the fact that the method is based on computing a derivative. As a result, even small fluctuations in the data can have a pronounced effect on the slope estimation.

As an alternative approach, we divided the sample into only two subsamples: high-σ and low-σ, yielding a total of eight bins when combined with the redshift division. The corresponding age–z diagram is shown in Fig. 3.9b, where it can be seen that the slopes in the two σ bins are more stable. This improved stability suggests a more reliable attempt at estimating $H(z)$, as will be described below.

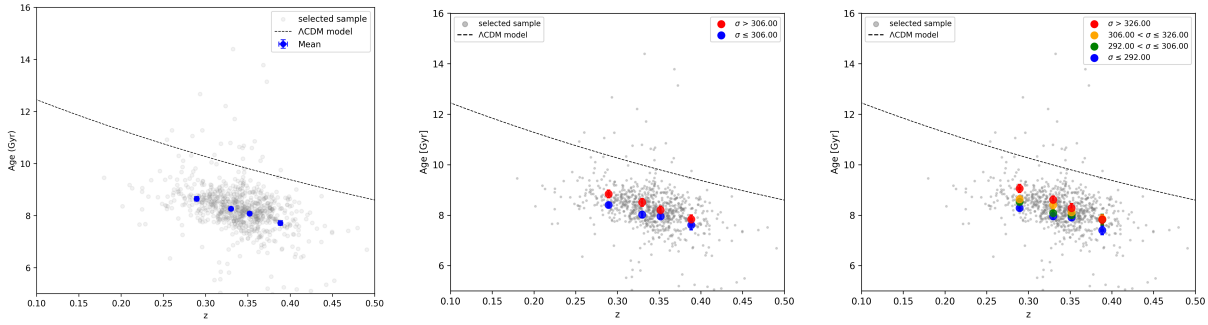

(a) $\tau < 1.0$, no bins of σ (b) $\tau < 1.0$, 2 bins of σ (c) $\tau < 1.0$, 4 bins of σ

Figure 3.9: Age–redshift diagrams for the passive sample of 900 galaxies (grey dots), shown with different binning schemes. (a) Original binning in redshift only; (b) division into two σ bins, representing the low- and high-σ subsamples. (c) division into four σ bins corresponding to the quartiles; Each point represents the mean value within each bin.

3.3.3 A new estimate of the expansion rate of the Universe

In this Section, we present how to derive constraints on the ages of massive and passive galaxies without any cosmological assumptions, which is at the basis of the CC method introduced in Sect. 1.3.

It is worth emphasizing again that the CC method offers a powerful, cosmology-independent tool to constrain the expansion history of the Universe by directly measuring the Hubble parameter through differential age dating of massive, passive galaxies. This method avoids extrapolations and relies solely on accurate relative age estimates. As discussed earlier, starting from the cosmological principle, general relativity, and adopting a FLRW metric, the Hubble parameter as a function of redshift can be expressed as:

$$H(z) = -\frac{1}{(1+z)}\frac{\mathrm{d}z}{\mathrm{d}t}. \tag{3.11}$$

Thus, starting from a sample of CCs, it is possible to estimate this parameter at the cosmic epoch corresponding to the galaxies in the sample, by computing the age variation $\mathrm{d}t$ and the corresponding redshift variation $\mathrm{d}z$. In other words, this requires estimating the derivative of the age–redshift relation $t(z)$, at the redshifts probed by the sample. To achieve this, a few crucial ingredients are needed:

- A sample of well-synchronized cosmic chronometers. Both the extended sample of 900 galaxies and the golden sample of 84 galaxies were selected to satisfy this requirement.

- An estimate of the differential age corresponding to a redshift interval sufficiently large compared to the error on individual age measurements, to obtain a robust estimate of the derivative $\mathrm{d}z/\mathrm{d}t$. To satisfy this condition, the derivative was computed by considering alternate points in the age–redshift diagram, ensuring they are separated by a sufficiently large redshift interval.

- Age uncertainties must be reasonably small to maximize the accuracy of the $\mathrm{d}z/\mathrm{d}t$ estimate. To satisfy this condition, the only viable approach is to increase the number of objects N within each bin, since the error on the mean age in each bin scales as $\mathrm{stdev}/\sqrt{N}$. This consideration motivated the extension of the analysis to the full sample of 900 galaxies.

The measurement of H(z), related to the choice of dividing the sample in redshift bins only, was computed by considering alternating redshift bins of the diagram age–z, obtaining two values of $H(z)$ and the associated errors in the following way;

$$H = -\frac{1}{1+z}\frac{z_1 - z_2}{t_1 - t_2} \tag{3.12}$$

$$H_{err} = \frac{|z_1 - z_2|}{1+z}\frac{\sqrt{t_{err,1}^2 + t_{err,2}^2}}{(t_1 - t_2)^2} \tag{3.13}$$

where (z_1, t_1) and (z_2, t_2) are the coordinates of the points corresponding to the mean value in age and redshift within each bin. The redshift associated with the measurement of H(z) was computed as the mean of the two considered points in Eq. 3.12. We then computed the weighted mean between the two values to carry out the final measurement of H(z).

In the case in which we divided the age–z diagram also in bins of σ, we derived $H(z)$ by applying Eq. 3.12 using the values from alternating redshift bins within each of the two σ bins. In this way, we obtained four estimates of the Hubble parameter: two for the low-mass subsample and two for the high-mass subsample. To derive a single value for each mass subsample, we computed the weighted mean of the two estimates corresponding to the same redshift bin. Finally, the overall value of $H(z)$ for the extended sample was obtained by taking the weighted mean of these two final values. The estimates of $H(z)$ obtained considering the two different binning choices are reported in Table 3.5.

Configuration	z	$H(z)$ [km/s/Mpc]	$\langle z \rangle$	$\langle H(z) \rangle$ [km/s/Mpc]	Fig.
$\tau < 1$, no bins of σ	0.32	82.3 ± 15.5	0.34	79.3 ± 11.1	3.9a
	0.36	76.3 ± 15.8			
$\tau < 1$, 2 bins of σ	0.31	63.2 ± 22.9	0.34	66.0 ± 18.3	3.9b
	0.37	71.0 ± 30.3			

Table 3.5: Measurements of the Hubble parameter $H(z)$ derived from the age–redshift analysis of the extended sample of 900 galaxies. The table reports the results obtained using both the redshift-only binning and the binning that also includes two σ bins. For each case, the values corresponding to the two redshift bins are listed, together with the weighted mean redshift $\langle z \rangle$ and the corresponding averaged estimate $\langle H(z) \rangle$. The last column provides the reference to the associated age–z figure.

The results obtained by dividing the sample into two σ bins are broadly consistent with those derived using the redshift-only binning approach. The value of the Hubble parameter, obtained as the weighted average of the two redshift bins, is in very good agreement with that derived from the more refined procedure involving an additional subdivision into σ bins. In this latter case, $H(z)$ was computed separately within each σ bin, then averaged at fixed redshift, and finally combined into a single estimate. The strong consistency between the two methods demonstrates that the selected sample is highly homogeneous, characterized by a synchronized star formation history, as expected for this class of galaxies.

This comparison between different binning strategies is particularly relevant, given that the CC technique relies on an accurate determination of the age–redshift relation. In other words, the fact that analyses based on velocity-dispersion bins yield results consistent with those obtained using redshift-only bins confirms the internal homogeneity of the sample and indicates that the method is robust across different binning choices.

For the final estimate, we therefore adopt the result obtained with the redshift-only binning. This choice provides a larger number of galaxies per bin, enhancing the statistical reliability of the mean age estimates and reducing the associated uncertainties. Hence, the value of the Hubble parameter, which is a remarkable outcome of this analysis, is:

$$H(z = 0.34) = 79.3 \pm 11.1 \text{ km s}^{-1} \text{ Mpc}^{-1},$$

as derived from the CC method applied to SDSS BOSS data. This result is shown in Fig. 3.10, compared with other results obtained with the CC approach.

The new value of $H(z)$ is used in the following Section to perform the cosmological analysis and to derive constraints on the main cosmological parameters through a Bayesian approach.

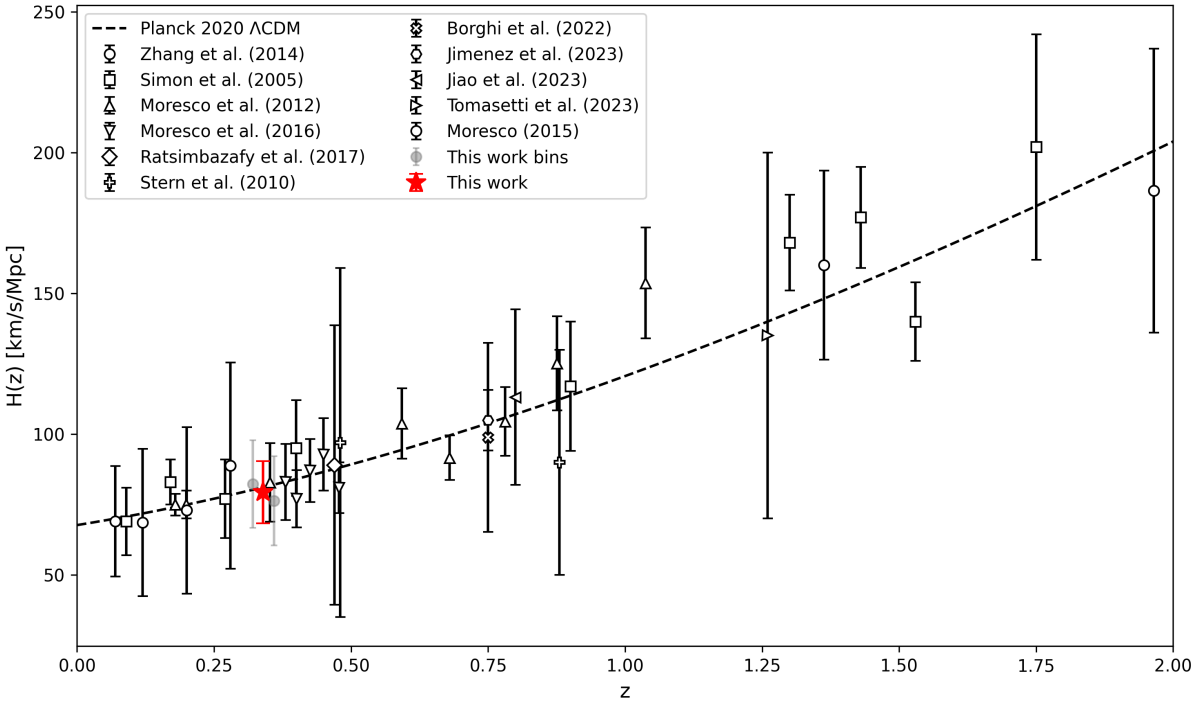

Figure 3.10: Measurements of the Hubble parameter obtained using the CC method. The results correspond to the configuration shown in 3.9a. The values obtained in this work for the two redshift bins are shown in gray, while the final value, calculated as the weighted mean of the gray points, is shown in red. For reference, the trend predicted by the ΛCDM model from (Aghanim et al., 2020) is also included.

3.4 Cosmological Analysis

Having obtained a new estimate of the Hubble parameter, we now present the methodology used to derive key cosmological parameters, specifically the Hubble constant H_0 and the present-day matter density parameter $\Omega_{m,0}$, based on the newly obtained measurement. The analysis is performed using a Python-based pipeline that assumes a spatially flat ΛCDM cosmological model and employs a *Markov Chain Monte Carlo* (MCMC) approach to explore the parameter space and derive posterior distributions. We chose to explore this simplest cosmological model to obtain a quantitative estimate of the impact of this new measurement on cosmological analyses, noting that in more complex scenarios the effect is expected to be smaller.

As introduced in Chapter 1.1.6, under the assumption of a flat ΛCDM universe, the Hubble parameter as a function of redshift can be expressed using a simplified form, which depends only on $\Omega_{m,0}$:

$$H(z) = H_0\sqrt{\Omega_{m,0}(1+z)^3 + (1-\Omega_{m,0})}, \tag{3.14}$$

which follows directly from the Friedmann equation under the assumption of spatial

flatness, i.e., $\Omega_{m,0} + \Omega_{\Lambda,0} = 1$.

3.4.1 Constraints on cosmological parameters

The parameters H_0 and $\Omega_{m,0}$ are estimated using an MCMC method, which allows us to fit the age–redshift relation and infer the underlying cosmological parameters. The MCMC approach is rooted in Bayesian inference: given prior knowledge of the parameter distributions and a likelihood function that quantifies the agreement between the model and the observational data, we obtain the posterior probability distribution of the parameters (see Sect. 3.1.1).

MCMC methods enable efficient sampling of the posterior distribution by constructing a stochastic chain of parameter vectors, which explores the space in such a way that regions of high posterior probability are more frequently sampled. This process allows the reconstruction of credible intervals and confidence contours for the parameters. The specific implementation used in this work relies on the `emcee` package (Foreman-Mackey et al., 2013), which employs an affine-invariant ensemble sampler. This algorithm evolves an ensemble of *walkers*, independent chains that move simultaneously through parameter space, leading to faster convergence and improved sampling efficiency, particularly in problems with correlated parameters or non-trivial posterior geometries.

Likelihood and Priors

The log-likelihood function is defined assuming a multivariate Gaussian form:

$$\ln \mathcal{L}(\mathbf{p}) = -\frac{1}{2} \left(\mathbf{H}^{\rm obs} - \mathbf{H}^{\rm model}(\mathbf{p})\right)^{\intercal} \mathbf{C}^{-1} \left(\mathbf{H}^{\rm obs} - \mathbf{H}^{\rm model}(\mathbf{p})\right), \tag{3.15}$$

where $\mathbf{p} = \{H_0, \Omega_{m,0}\}$.

A flat prior is imposed on both parameters:

$$50 < H_0 < 100 \ \mathrm{km\,s^{-1}Mpc^{-1}}, \qquad 0.01 < \Omega_{m,0} < 0.99.$$

A Gaussian prior on the matter density parameter, $\Omega_{m,0}$, may be optionally applied. It was not used in the main analysis but it can be enabled to include Planck18 constraints:

$$\ln \pi(\mathbf{p}) = -\frac{1}{2} \left(\frac{\Omega_{m,0} - \Omega_{m,0}^{\rm fid}}{\sigma_{\Omega_{m,0}}} \right)^2 .$$

MCMC Sampling

The posterior distribution is sampled using the affine-invariant ensemble sampler from the `emcee` package. We used 250 walkers and run 1000 steps, discarding the first 300 as

burn-in. Two runs were performed:

- With the full covariance matrix including systematics;
- With the diagonal-only (statistical) covariance.

Initial parameters are chosen as:

$$H_0 = 100, \quad \Omega_{m,0} = 0.5, \tag{3.16}$$

perturbed by small random noise to initialize the walkers.

This analysis led to the following results. The marginalized constraints (1σ) without systematic errors are:

$$\begin{aligned} H_0 &= 67.6^{+3.0}_{-3.0} \ \text{km s}^{-1}\,\text{Mpc}^{-1}, \\ \Omega_{m,0} &= 0.3^{+0.1}_{-0.1} \end{aligned}$$

Including the full systematic covariance as discussed in Moresco et al. (2020), we find:

$$\begin{aligned} H_0 &= 66.7^{+5.3}_{-5.3} \ \text{km s}^{-1}\,\text{Mpc}^{-1}, \\ \Omega_{m,0} &= 0.3^{+0.1}_{-0.1}. \end{aligned}$$

These results, shown in Fig. 3.11, are consistent with Planck18 within uncertainties, but they also highlight the importance of accounting for systematics in cosmic chronometers analyses. The inclusion of systematic errors in the CC covariance matrix leads to a broader uncertainty in the recovered parameters, as expected. This demonstrates the importance of carefully modeling all sources of error, especially when aiming to provide independent constraints on cosmological parameters. The results show good agreement with Planck18 values, supporting the reliability of the CC method as an independent cosmological probe.

In the literature, results obtained through the CC method applied to BOSS data are already available, for example in Moresco et al. (2016). In that analysis, the determination of galaxy ages was performed by exploiting the D4000 spectral break, as discussed in Sect. 1.3.2, and relying on a large sample of more than 130,000 objects. In contrast, in this work we present, for the first time, a re-analysis of the BOSS dataset in which the galaxy ages are estimated using a full spectral fitting approach, applied to a smaller and carefully selected subsample of about 900 galaxies. This alternative methodology allows us to derive the parameters required to apply the CC method through a more comprehensive treatment of the observed spectra, potentially reducing systematics and providing a complementary perspective with respect to previous works. The different sample sizes also explain why the overall constraining power of our analysis does not improve with respect to Moresco et al. (2016), since both studies are ultimately based on the same

underlying dataset.

In Fig. 3.12 we compare the results of the cosmological analysis obtained by including all measurements available up to 2023 with those derived when replacing the BOSS contribution of Moresco et al. (2016) with our new estimates. The comparison shows that the results remain fully consistent, thereby reinforcing the robustness of the CC approach. At the same time, this exercise highlights the importance of developing and employing independent techniques for the estimation of galaxy ages, as they provide crucial cross-checks and strengthen the reliability of cosmological constraints derived from the CC method. In this sense, the fact that an independent subsample analyzed with a different methodology yields fully compatible results is a particularly encouraging outcome.

The marginalized 1σ constraints, obtained from the dataset including the new $H(z)$ measurements derived in this analysis, and excluding those from Moresco et al. (2016), without accounting for systematic uncertainties, are:

$$\begin{aligned} H_0 &= 68.3^{+3.0}_{-3.0}\,\mathrm{km\,s^{-1}\,Mpc^{-1}}, \\ \Omega_{m,0} &= 0.3^{+0.1}_{-0.1}. \end{aligned}$$

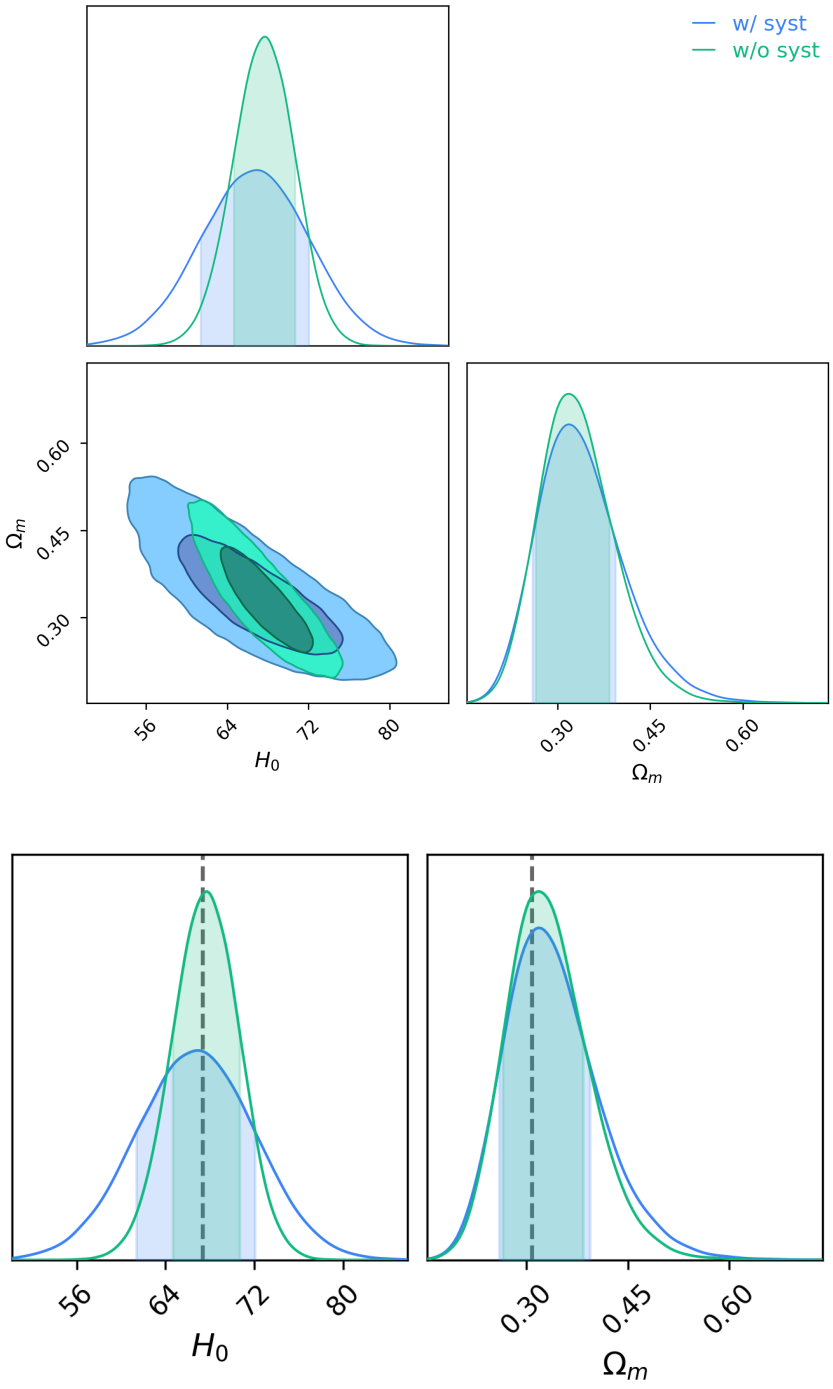

Figure 3.11: Comparison of cosmological parameter estimates including the effect of systematics. *Top panel:* Corner plot of the posterior distribution for H_0 and $\Omega_{m,0}$, showing the results with and without systematics. *Bottom panel:* Marginalized parameter distributions compared with Planck18 values (dashed lines), highlighting the impact of systematics and the agreement with independent cosmological measurements.

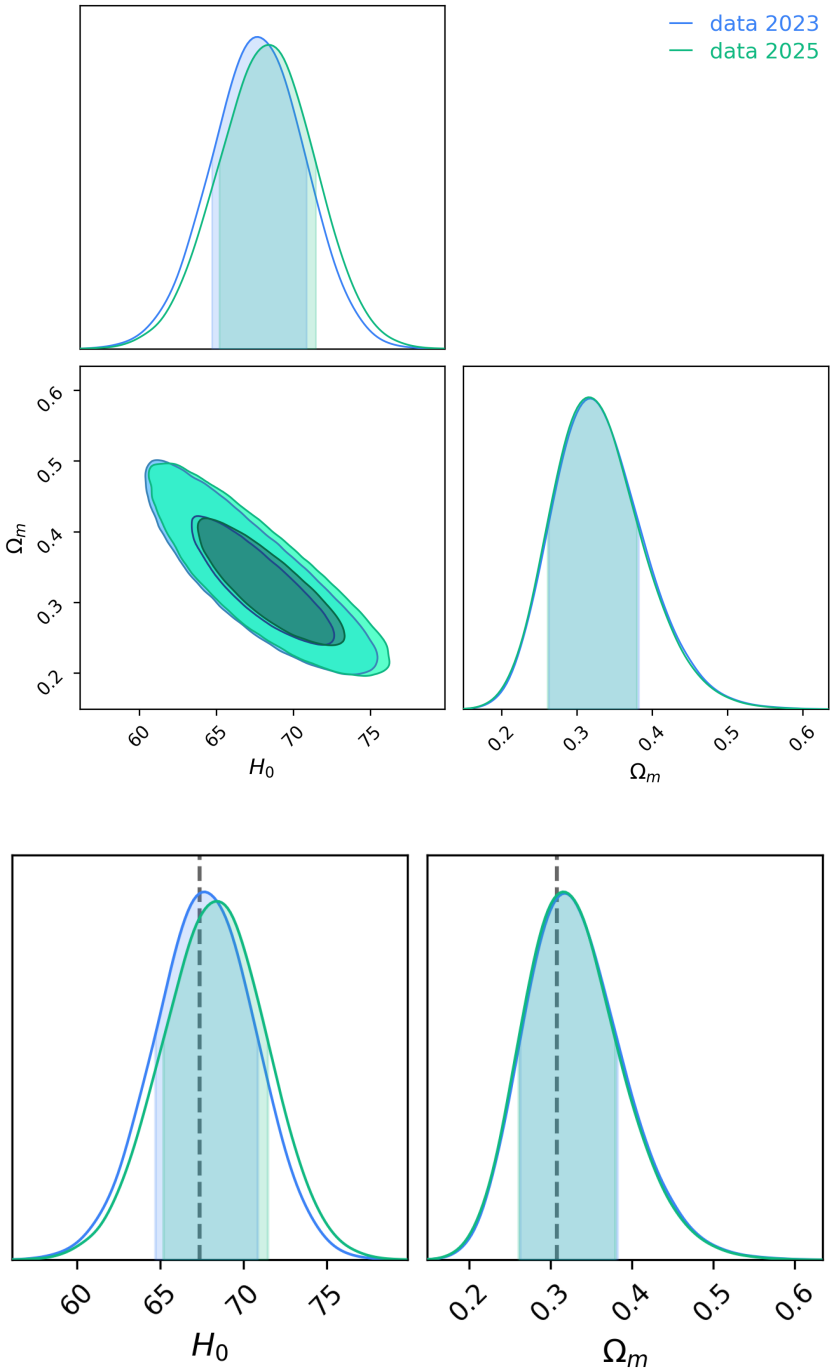

Figure 3.12: Comparison of cosmological parameter estimates including the new BOSS age determinations. *Top panel:* Corner plot showing the posterior distribution of H_0 and $\Omega_{m,0}$, comparing previous measurements with the results obtained in this work, where our BOSS estimates replace those from Moresco et al. (2016). *Bottom panel:* Marginalized posterior distributions compared with the Planck18 values (dashed lines), clearly illustrating the full consistency between the two results.

In light of the discussion so far, the emerging scenario suggests two main avenues for improving the results obtained from cosmic chronometers. On the one hand, increasing the statistical sample would enhance the robustness of the analysis; however, this depends on the upcoming data releases from new spectroscopic surveys. On the other hand, it is crucial to focus on addressing systematic uncertainties. In particular, in this work we expand the analysis by investigating, for the first time, the impact of different stellar population models on the age estimates obtained through FSF techniques.

Chapter 4

A new framework to characterize systematics for cosmic chronometers

As emphasized in previous chapters, one of the main challenges of the CC method is related to properly assessing systematic uncertainties. In this Chapter, we address the core of this open point by examining it in greater depth, aiming to quantify, for the first time, the impact of systematic uncertainties on age estimates derived from a full spectral fitting approach, thanks to a novel implementation of models within the `Bagpipes` code. To carry out this analysis, we developed modified versions of `Bagpipes` that allow us to investigate how variations in key model ingredients affect the results. In particular, we implemented new models based on the `FSPS` package (Conroy et al., 2009; Conroy & Gunn, 2010), which allowed us to test the effect of considering different SPS models (`BC16` and `FSPS`), different IMFs (Kroupa, Chabrier, and Salpeter), as well as different stellar libraries (`BaSeL` and `MILES`).

Thanks to this new implementation, we are able for the first time to associate a systematic error with the derived Hubble parameter obtained with FSF and the CC method, estimating the impact of each single component. In this way, we also provide a new measurement of the Hubble parameter from the SDSS BOSS survey, correctly accounting for both statistical and systematic errors. This is a significant first step to further enhance the robustness of this method and improve its performance.

4.1 Developing a new set of stellar grids

Different Stellar Population Synthesis codes are available in the literature, as already discussed in Sect. 1.2.2. The more widely used are the Bruzual & Charlot (2003) models (`BC03`, and its later development, `BC16`), the Flexible Stellar Population Synthesis models (`FSPS`, Conroy et al., 2009; Conroy & Gunn, 2010), the Binary Population and Spectral Synthesis models (`BPASS`, Eldridge et al., 2017), and the Maraston & Strömbäck (2011)

models (M11). Each one encompasses different recipes to build theoretical models from the ingredients discussed in Sect. 1.2.2. In this thesis, we focus in particular on FSPS, since it allows a versatility to easily build the variety of libraries needed in our work. Another key advantage of FSPS is that recent developments by Park et al. (2024) (α-MC) open up the possibility of including in this code also models with varying α/Fe ratios, crucial to properly model these galaxies in the future.

The FSPS package allows the computation of simple stellar populations across a range of initial mass functions and metallicities, while providing flexibility in modeling key evolutionary phases, including the horizontal branch morphology, blue straggler stars, post-AGB evolution, and the thermally pulsing asymptotic giant branch (TP-AGB) phase. From these SSP, the user can construct composite stellar populations corresponding to different star formation histories and dust attenuation prescriptions. The FSPS outputs include spectra and photometric magnitudes of SSP and CSP at arbitrary redshifts, enabling a detailed comparison with observational data.

In this work, we have produced custom libraries from FSPS, tailored to our needs, which are subsequently implemented within Bagpipes to perform full spectral fitting and derive stellar population parameters. This allowed us to easily explore a wide range of parameters, opening the possibility in the future also to expand the analysis by including models with varying [α/Fe]. The procedure for constructing the stellar libraries with FSPS is outlined as follows:

1. **Define the age grid.** We adopted the default age grid implemented in Bagpipes, which spans from 10^4 yr to 2×10^{10} yr using a non-uniform, logarithmically spaced sampling. This choice ensures sufficiently fine coverage to capture age-sensitive spectral features, while maintaining consistency with the stellar grids already available in Bagpipes.

2. **Define the metallicity grid.** We considered a set of metallicities Z in solar units, assuming $Z_\odot = 0.02$. Specifically, the adopted values are Z = [0.0001, 0.001, 0.01, 0.02, 0.03, 0.04]. In FSPS, these values must be converted to $\log_{10}(Z/Z_\odot)$, which is the parameterization used internally by the code.

3. **Loop over metallicities and ages.** For each metallicity, a SSP spectrum is generated. The models are computed assuming a single-burst star formation history, continuous interpolation in metallicity and the selected IMF (e.g. Kroupa).

4. **Generate spectra.** For each age in the defined grid, the corresponding spectrum is computed, producing an output containing the wavelength array and the associated flux in physical units.

5. **Save spectra.** Each spectrum is saved as a text file containing two columns: wavelength and flux.

In the context of this work, new libraries were generated using different assumptions for the IMF and stellar spectral libraries. Each of these libraries was implemented within a dedicated version of `Bagpipes`, allowing for a systematic investigation of how variations in these fundamental ingredients affect the derived stellar population properties. In order to employ the newly generated stellar grids within `Bagpipes`, it is essential to ensure that the relevant stellar population variables are correctly defined, so that the code can properly read and interpret the input spectra. For this purpose, we constructed a single multi-extension `FITS` file, which collects all the spectra corresponding to the full grid of ages and metallicities considered. This format provides an efficient and consistent way to organize the models, ensuring compatibility with the `Bagpipes` framework. Once the libraries have been created, the procedure was validated by comparing theoretical models generated using the standard `Bagpipes` setup, which employs the `BC16` stellar population model, with those produced using the new `FSPS`-based libraries. We verified that a model spectrum computed with identical input parameters in `FSPS` was fully consistent with that obtained by implementing the new `FSPS`-based grids within `Bagpipes`. In Fig. 4.1, the spectra generated by the `BC16` and `FSPS` models are shown for comparison, which were used to validate the adopted procedure.

The models created and used in this work are summarized in Table 4.1, along with others that are already available in the literature or may become available for future studies but are not yet publicly accessible. These customized libraries were then used as inputs for `Bagpipes` to perform full spectral fitting, enabling a controlled investigation of how variations in model assumptions, IMF, and stellar library affect the inferred stellar population parameters. The configuration adopted for the FSF corresponds to the baseline setup described in Table 3.3. The analysis presented in Chapter 3 was repeated independently for each version of `Bagpipes`. In each case, the procedure consisted of performing the FSF to derive estimates of the stellar population parameters, applying quality criteria to exclude unreliable fits, and dividing the resulting sample into redshift bins. From these bins, new age–redshift diagrams were constructed (Figs. 4.2, 4.4 and 4.5), from which updated estimates of $H(z)$ were derived.

4.1.1 Changing SPS Model

One of the key elements in constructing SSP is the choice of the SPS model. In this work, we focused on two widely adopted SPS models in galaxy evolution studies: `BC16` (Bruzual & Charlot, 2003) and `FSPS` (Conroy et al., 2009; Conroy & Gunn, 2010). The Bruzual & Charlot models are based on the isochrone synthesis technique and employ the `Padova` stellar evolutionary tracks (Alongi et al., 1993; Bressan et al., 1993; Fagotto et al.,

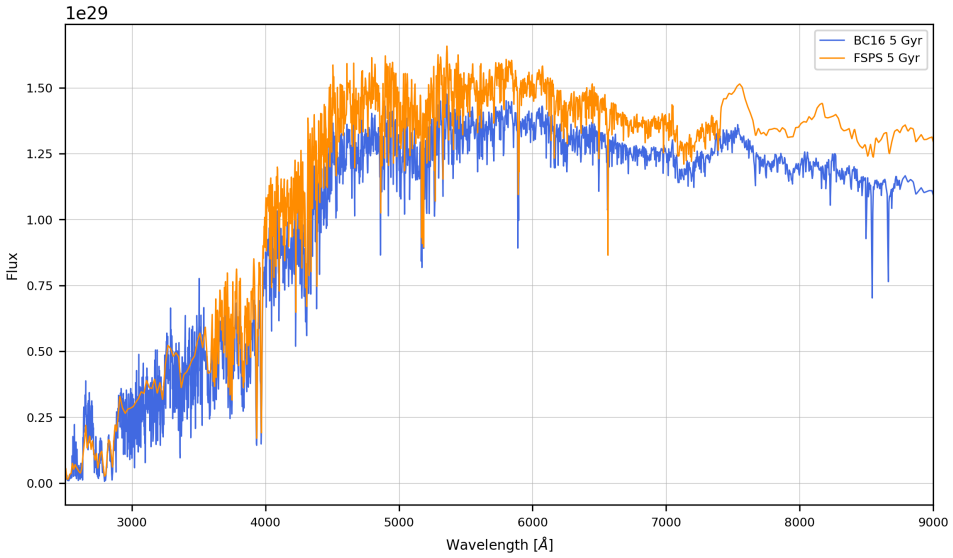

(a) Comparison between the `BC16` and `FSPS` models at an age of 5 Gyr.

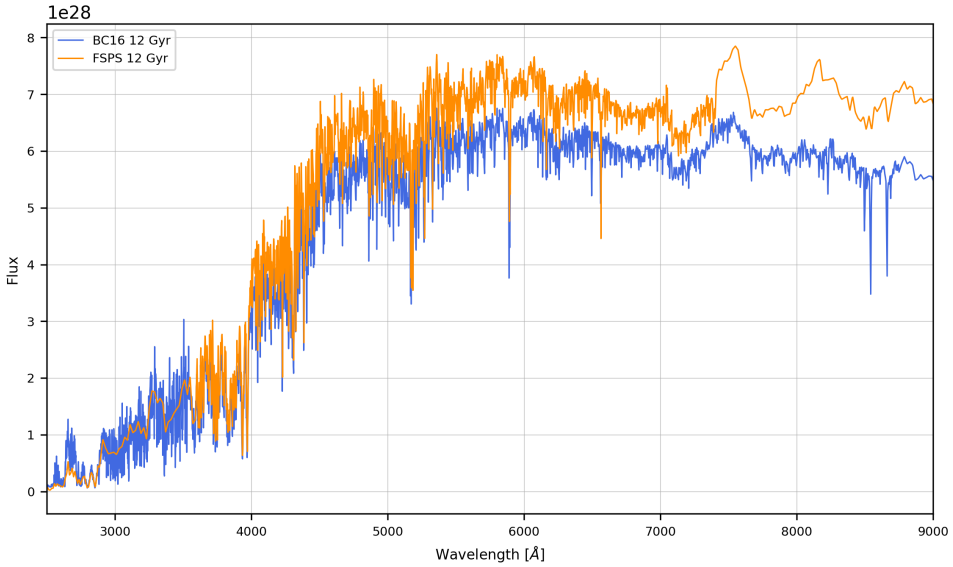

(b) Comparison between the `BC16` and `FSPS` models at an age of 12 Gyr.

Figure 4.1: Example of model spectra generated using the `BC16` and `FSPS` models, employed to validate the stellar grids generation procedure. The upper and lower panels show spectra corresponding to stellar populations with ages of 5 Gyr and 12 Gyr, respectively.

1994). The updated `BC16` models have been generated using different stellar libraries. In this study, we used the `BC16` implementation available in the standard version of `Bagpipes`, which adopts the `MILES` stellar library (with a spectral resolution of 2.3 Å; Bruzual & Charlot 2003) and assumes a Kroupa IMF (Kroupa, 2001). The `FSPS` models include thermally pulsing asymptotic giant branch (TP-AGB) phases following Lançon & Mouhcine (2002), and additionally account for circumstellar dust shells around AGB stars. For the `FSPS` models, `MILES` stellar library and `MIST` isochrones are adopted as fiducial

SPS Model	BC16	**FSPS**	*BPASS*	*M11*
IMF	**Kroupa**	**Chabrier**	**Salpeter**	
Stellar Library	**MILES**	**BaSeL**		
[α/Fe]	α-*MC* (Park et al., 2024)			

Table 4.1: Summary of the grid of models implemented within `Bagpipes`, separated for each component. Models already available are shown in normal text, the newly implemented in this study are shown in boldface, while the others that we plan to include in a future analysis are shown in italic.

model, and we further explore the impact of varying the stellar library by considering `BaSeL`, in combination with different IMFs (Chabrier, Kroupa, and Salpeter).

The results obtained changing SPS model (`BC16` and `FSPS`) are shown in Fig. 4.2 and reported in Table 4.2, allowing a direct comparison of the systematic effects introduced by varying this key model ingredient.

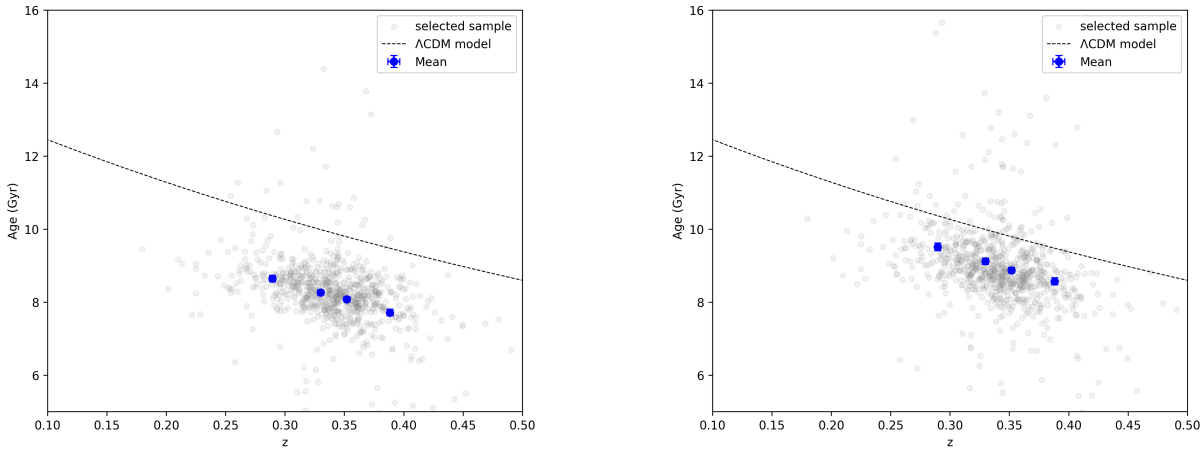

(a) `BC16` (b) `FSPS`

Figure 4.2: Comparison of age–redshift diagrams obtained with different SPS models: (a) `BC16` and (b) `FSPS`. The figure illustrates the impact of the SPS choice on the inferred stellar population parameters and on the resulting $H(z)$ estimates.

SPS Model	z	$H(z)$[km/s/Mpc]	$\langle z \rangle$	$\langle H(z) \rangle$ [km/s/Mpc]
BC16	0.32	82.3 ± 15.5	0.34	79.3 ± 11.1
	0.36	76.3 ± 15.8		
FSPS	0.32	72.3 ± 14.6	0.34	74.0 ± 11.3
	0.36	76.5 ± 17.8		

Table 4.2: $H(z)$ measurements derived from the age–redshift analysis for the two SPS models considered: BC16 and FSPS. For each SPS model, the table reports the values obtained in the individual redshift bins, as well as the weighted average redshift $\langle z \rangle$ and the corresponding averaged estimate $\langle H(z) \rangle$.

4.1.2 Changing IMF

The initial mass function was already introduced in Sec.1.2.2 as one of the main ingredients required to build an SSP. The shape of the IMF is observationally determined by studying individual stars in young stellar clusters and inferring their masses. Despite intrinsic uncertainties in this procedure, the IMFs derived from clusters in our Galaxy show a general similarity. However, it is not possible to resolve individual stars in clusters of external galaxies, except for very nearby systems such as the Large Magellanic Cloud. Consequently, it remains unclear to what extent the IMF is "universal". For instance, it may differ in starburst galaxies compared to quiescent and less dense environments, such as present-day galactic discs. In general terms, the IMF $\Phi(m)$, with m the stellar mass in units of the solar mass, quantifies the number of stars $\mathrm{d}N$ with masses between m and $m + \mathrm{d}m$. The first determination of the IMF was carried out by Salpeter (1955). The *Salpeter* IMF has the form of a single power law:

$$\mathrm{d}N = \Phi(m)\,\mathrm{d}m = \Phi_0\, m^{-2.35}\,\mathrm{d}m, \tag{4.1}$$

where Φ_0 is the normalization constant, chosen such that $\int_{0.1}^{100} \Phi(m) m\,\mathrm{d}m = 1$. For a Salpeter IMF, this gives $\Phi_0 \simeq 0.17$.

In subsequent decades, it has become clear that the IMFs of stellar clusters in the Milky Way typically depart from the Salpeter slope at the low-mass end. Several alternative formulations have therefore been proposed, including the two that we employ in this work.

The so-called *Kroupa* IMF (Kroupa, 2001) is described by three different power laws, each valid for a different mass range:

$$\Phi(m) = \begin{cases} 2.0\, m^{-1.3} & (0.08 \leq m < 0.5), \\ m^{-2.3} & (0.5 \leq m < 1), \\ m^{-2.3\,(-2.7)} & (m \geq 1), \end{cases} \tag{4.2}$$

where at high masses two possible slopes are given, though in practice the -2.3 slope is most commonly adopted.

The typical uncertainties associated with these slopes are ≈ 0.3, which indicates the intrinsic limitations of IMF determinations. The Kroupa IMF is the one adopted as our baseline in this work, as it is the default choice in `Bagpipes`. The *Chabrier* IMF, suggested by Chabrier (2003), is tailored to various Galactic environments. For disc stars (normalized at $m = 1$), the formulation reads:

$$\Phi(m) = \begin{cases} \mathrm{A}\,\dfrac{1}{m}\,\exp\left\{-\mathrm{B}\,\left[\log\left(\dfrac{m}{0.079}\right)\right]^2\right\} & (m < 1), \\ m^{-2.35\ (-2.3)} & (m \geq 1), \end{cases} \tag{4.3}$$

where A and B are normalization constants whose values differ between the 2003 and 2005 versions. The high-mass slope also varies accordingly, and both formulations are commonly used in the literature.

In comparison to other IMFs, the Salpeter IMF is considered *bottom-heavy*, where "bottom" refers to the low-mass end (typically $m \lesssim 1\,\mathrm{M}_\odot$) and "heavy" reflects the fact that the integrated mass of low-mass stars is maximised relative to the high-mass contribution. Conversely, an IMF that increases the relative contribution of high-mass stars with respect to low-mass stars (e.g., the Chabrier IMF compared to the Salpeter IMF) is referred to as *top-heavy*. A comparison among the three IMFs discussed above is presented in Fig. 4.3, where, for completeness, it is also included the Scalo IMF (Scalo, 1986). However, since it is not directly relevant to the scope of this work, we do not consider it further in our analysis.

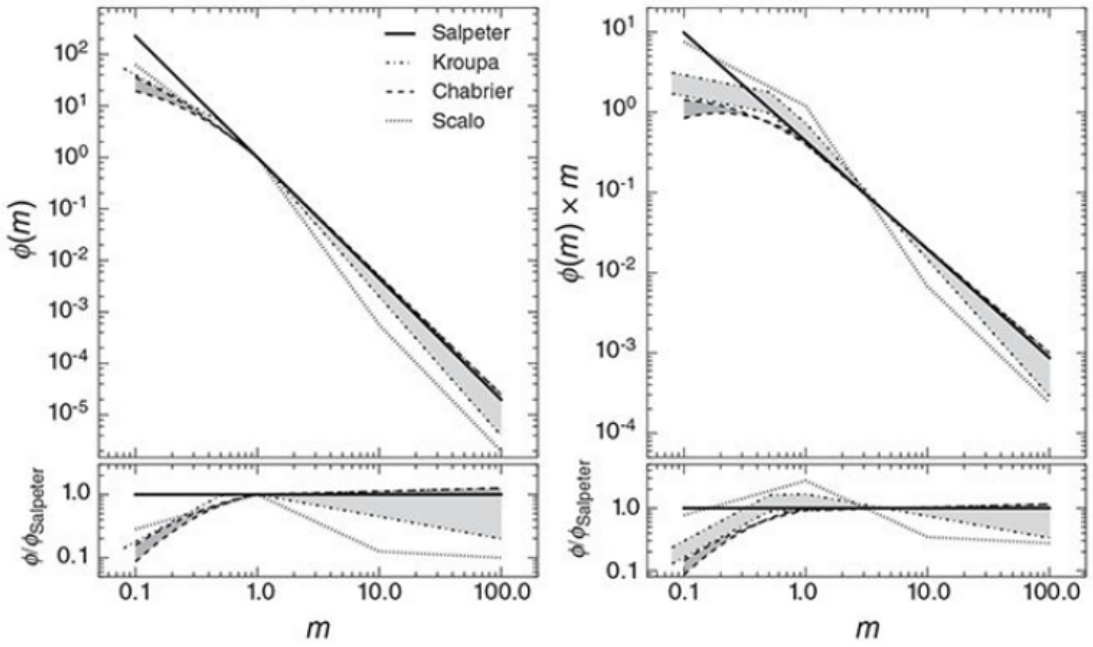

Figure 4.3: Comparison of the different initial mass function discussed in this work. *Top left panel:* IMFs expressed as a function of the number of stars, $\phi(m)$, indicating the number of stars in the mass interval m to $m + dm$, where $m = M/M_{\odot}$, normalized at $m = 1$. *Top right panel:* IMFs expressed in terms of stellar mass, representing the mass contained in the interval m to $m + dm$, normalized to the total mass integral between $m = 1$ and $m = 100$. In both panels, the two versions of the Kroupa IMF (light grey band) with different high-mass slopes (Eq. 8.88) and the Chabrier IMF (dark grey band) are shown. *Bottom panels:* Ratios of the various IMFs relative to the Salpeter IMF. (From Cimatti et al., 2019).

The results obtained for the different IMF assumptions are shown in Fig. 4.4 and reported in Table 4.3, allowing a direct comparison of the systematic effects introduced by varying this key model ingredient.

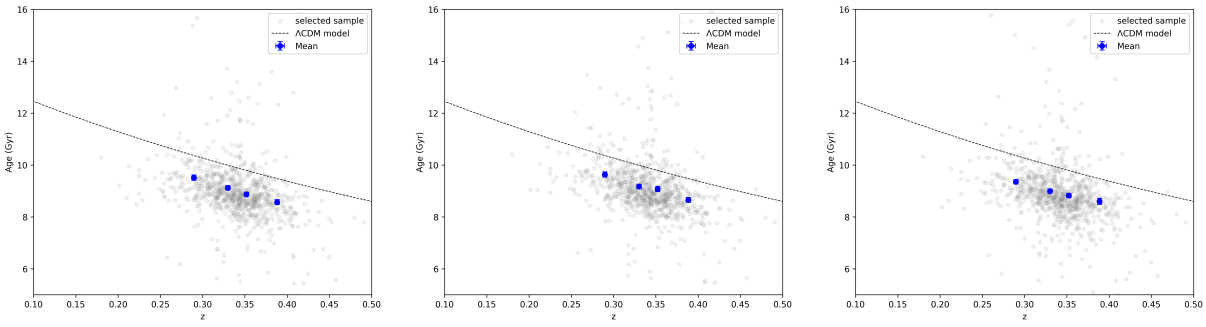

(a) Kroupa (b) Chabrier (c) Salpeter

Figure 4.4: Age–redshift diagrams obtained using three different initial mass functions: (a) Kroupa, (b) Chabrier, and (c) Salpeter. The comparison highlights the impact of the IMF choice on the derived stellar population properties and, in particular, on the estimates of $H(z)$.

IMF	z	$H(z)$[km/s/Mpc]	$\langle z \rangle$	$\langle H(z) \rangle$ [km/s/Mpc]
Kroupa	0.32	72.3 ± 14.6	0.34	74.0 ± 11.3
	0.36	76.5 ± 17.8		
Chabrier	0.32	83.0 ± 21.5	0.34	82.1 ± 14.9
	0.36	81.3 ± 20.6		
Salpeter	0.32	86.8 ± 19.8	0.33	100.0 ± 17.4
	0.36	105.5 ± 36.8		

Table 4.3: $H(z)$ measurements derived from the age–redshift analysis for different choices of the IMF: Kroupa, Chabrier, and Salpeter. For each IMF, the table reports the values obtained in the individual redshift bins, as well as the weighted average redshift $\langle z \rangle$ and the corresponding averaged estimate $\langle H(z) \rangle$.

4.1.3 Changing Stellar Libraries

In addition to testing different assumptions for the IMF, we also investigated the impact of changing the underlying stellar library in `FSPS`. As discussed in Sect. 1.2.2, stellar libraries represent a fundamental component of stellar population synthesis, as they provide the empirical or theoretical stellar spectra that are combined to construct simple stellar populations. The choice of library can significantly influence the resulting models, particularly in spectral regions where empirical coverage is limited or theoretical predictions are uncertain.

The default implementation of `Bagpipes` relies on the empirical `MILES` library (Sanchez-Blazquez et al., 2006; Falcón-Barroso et al., 2011a), which consists of medium-resolution optical spectra of nearly one thousand stars spanning a broad range of effective temperatures, surface gravities, and metallicities. Thanks to its empirical nature and relatively high spectral resolution, `MILES` provides robust predictions in the optical domain, especially for absorption-line features that are widely used in stellar population studies. However, its wavelength coverage is restricted to 3525–7500 Å, which limits its applicability when analyzing spectra that extend into the ultraviolet or near-infrared.

As an alternative, we employed the theoretical `BaSeL` library (Lejeune et al., 1998; Westera et al., 2002), which provides a much broader wavelength coverage, extending from the ultraviolet to the near-infrared. Although this extended range is not expected to play a major role in the specific full spectral fitting setup adopted in this work, it nevertheless constitutes a relevant difference with respect to `MILES`. The `BaSeL` models are derived from theoretical stellar atmosphere calculations, complemented by semi-empirical corrections to improve consistency with observed photometry. While their spectral resolution is lower and some absorption features are less accurately reproduced compared to empirical

libraries, BaSeL offers complete spectral energy distributions across a wide wavelength range, making it particularly valuable for applications requiring extended coverage. To quantify the effect of this choice, we repeated the procedure described above for generating stellar grids, this time adopting the BaSeL library in place of MILES. For consistency, this test was carried out only for the Kroupa IMF, assumed as our fiducial reference throughout this work. This allowed us to isolate the systematic differences in stellar population parameter estimation that arise purely from the choice of stellar library. The resulting fits were then analyzed following the same methodology applied to the MILES-based models, enabling a direct comparison of the inferred age-redshift relations and their impact on the derived values of $H(z)$.

The results obtained from the two stellar libraries implemented are shown in Fig. 4.5 and reported in Table 4.4, allowing a direct comparison of the systematic effects introduced by varying this key model ingredient.

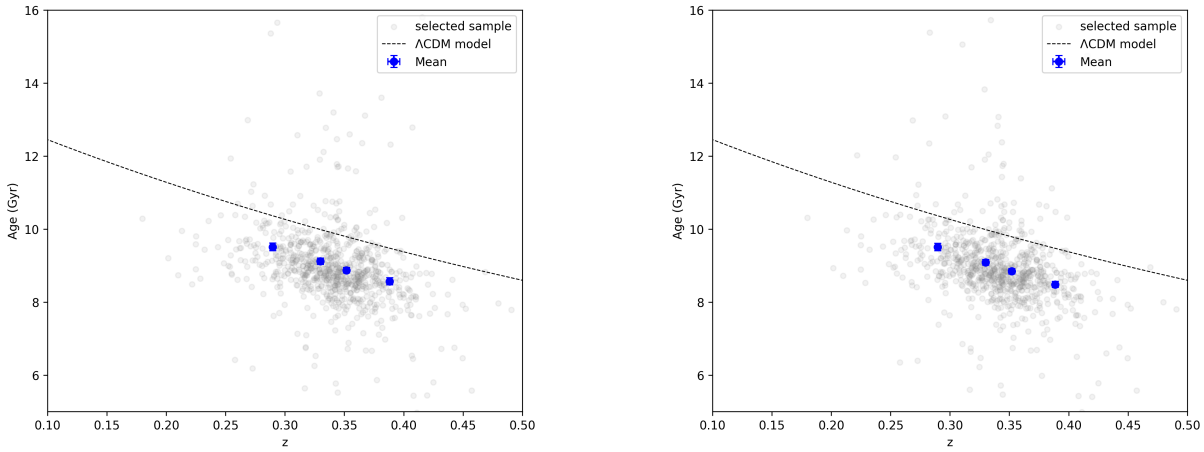

(a) MILES (b) BaSeL

Figure 4.5: Comparison of age–redshift diagrams obtained with different stellar libraries: (a) MILES and (b) BaSeL. The figure illustrates the impact of the stellar library choice on the inferred stellar population parameters and on the resulting $H(z)$ estimates.

Stellar libraries	z	$H(z)$[km/s/Mpc]	$\langle z \rangle$	$\langle H(z) \rangle$ [km/s/Mpc]
MILES	0.32	72.3 ± 14.6	0.34	74.0 ± 11.3
	0.36	76.5 ± 17.8		
BaSeL	0.32	69.7 ± 13.1	0.34	69.8 ± 9.3
	0.36	69.9 ± 13.1		

Table 4.4: $H(z)$ measurements derived from the age–redshift analysis for the two stellar libraries implemented: MILES and BaSeL. For each stellar library choice, the table reports the values obtained in the individual redshift bins, as well as the weighted average redshift $\langle z \rangle$ and the corresponding averaged estimate $\langle H(z) \rangle$.

4.2 Assessing the systematic effects on the expansion rate of the Universe

Once the estimates of $H(z)$ were obtained for each of the modified versions of `Bagpipes` described in the previous sections, we performed a series of controlled comparisons to quantitatively evaluate the impact of the systematic effects considered in this work. In particular, we investigated the role of three main sources of systematics by varying one component at a time while keeping the others fixed:

- **SPS model effect**. With the Kroupa IMF and the `MILES` stellar library fixed as fiducial assumptions, we compared the results obtained using the `BC16` and `FSPS` stellar population models.
- **IMF effect**. Adopting `FSPS` with the `MILES` stellar library, we explored the impact of varying the IMF by comparing the three cases considered: Kroupa, Chabrier, and Salpeter.
- **Stellar library effect**. Fixing `FSPS` and the Kroupa IMF, we tested the influence of the stellar library by comparing results obtained with `MILES` and `BaSeL`.

These combinations are summarized in Table 4.5, which schematically describes the baseline assumptions and the specific components varied in each case.

Baseline choice	**Varied component**	**Systematic Source**
Kroupa, MILES	BC16 vs. FSPS	SPS model
FSPS, MILES	Kroupa vs. Chabrier / Salpeter	IMF
FSPS, Kroupa	MILES vs. BaSeL	Stellar library

Table 4.5: Combinations of baseline assumptions and varied inputs used to estimate systematic uncertainties in the CC method based on full spectral fitting.

It is important to recall that each determination of $H(z)$ is derived using the CC method, which, as emphasized throughout this work, relies on estimating the slope of the age–redshift relation, i.e. the ratio $\mathrm{d}z/\mathrm{d}t$. Consequently, the accuracy and robustness of $H(z)$ measurements depend critically on the differential age estimates of the underlying galaxy populations. Since these ages are obtained through full spectral fitting, their values inevitably vary depending on the adopted assumptions for the SPS model, the IMF, or the stellar library implemented in `Bagpipes`. Even small differences in the recovered ages across these configurations propagate directly into differences in the estimated $\mathrm{d}z/\mathrm{d}t$,

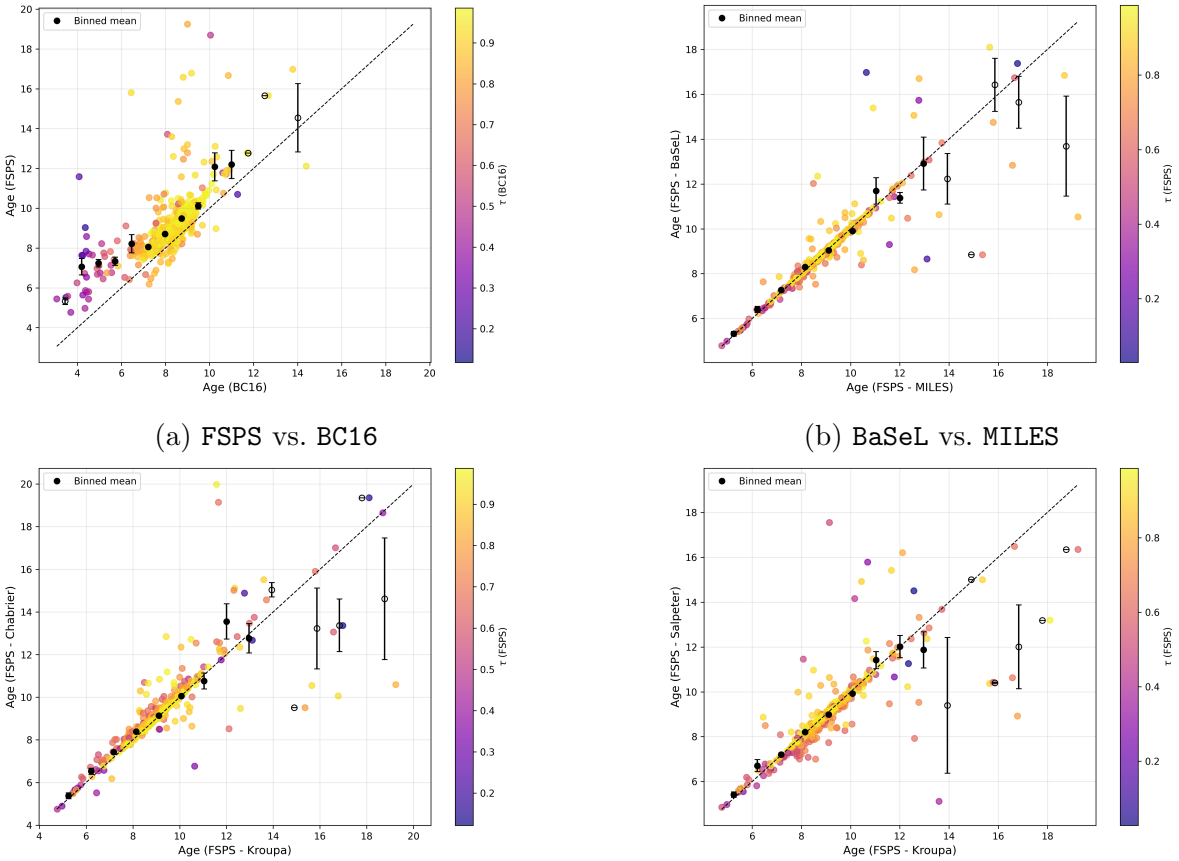

(a) `FSPS` vs. `BC16`

(b) `BaSeL` vs. `MILES`

(c) Chabrier vs. Kroupa

(d) Salpeter vs. Kroupa

Figure 4.6: Comparison of age–age relations obtained under different assumptions: (a) `FSPS` vs. `BC16`, (b) `BaSeL` vs. `MILES`, (c) Chabrier vs. Kroupa, and (d) Salpeter vs. Kroupa. Black circles show the binned averages, where empty points are reported in case the number of averaged objects is too low ($N < 5$).

and therefore into the inferred $H(z)$ values. A first qualitative representation of the changes in the slopes within the alternating bins of the age–z diagram, used to apply the CC method, is shown in Fig. 4.7. This effect can be more clearly appreciated from a quantitative perspective in the diagnostic diagrams presented in Figs. 4.6 and 4.8, where age and dt estimates obtained under different assumptions are directly compared. The main point, however, is that the dt estimates remain in remarkable agreement across the different models, highlighting the robustness of the CC approach. This study further highlights how systematic shifts in the recovered stellar population properties propagate into systematic variations in $H(z)$, emphasizing the importance of carefully assessing model dependencies when applying the CC method.

The Hubble parameter measurements, $H(z)$, obtained from the different configurations are shown in Fig. 4.9, grouped according to the specific systematic effect under consideration. This presentation allows for a direct comparison of the results and provides a clear visualization of how each systematic contribution has been evaluated.

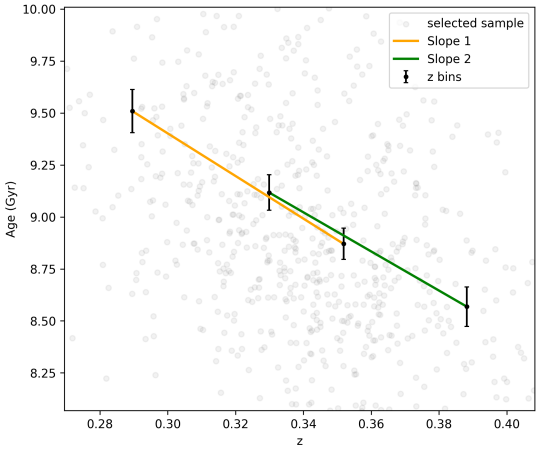

(a) **FSPS**, Kroupa, MILES

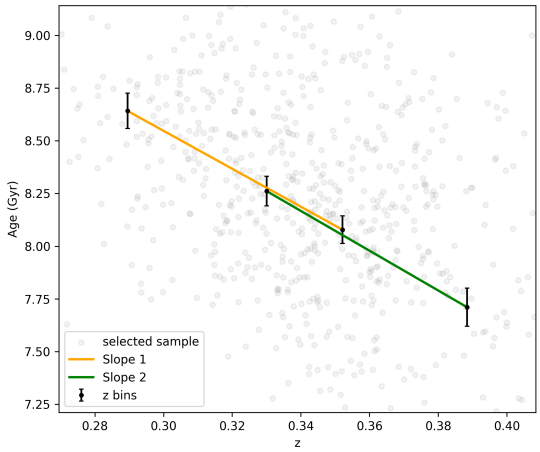

(b) **BC16**, Kroupa, MILES

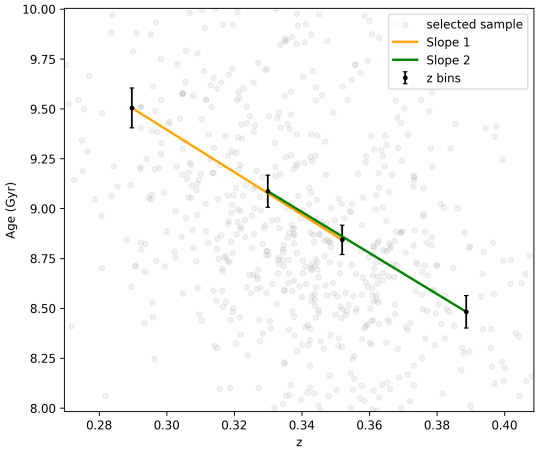

(c) FSPS, Kroupa, **BaSeL**

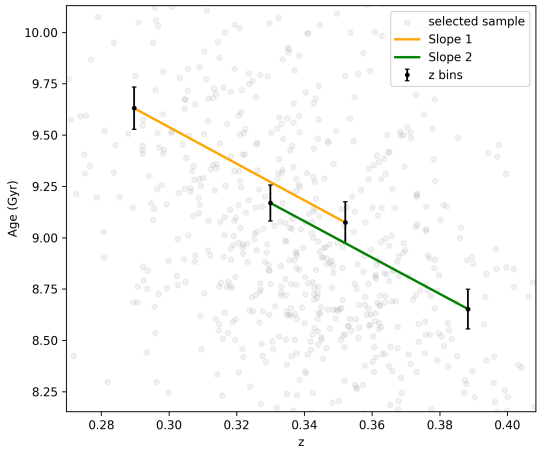

(d) FSPS, **Chabrier**, MILES

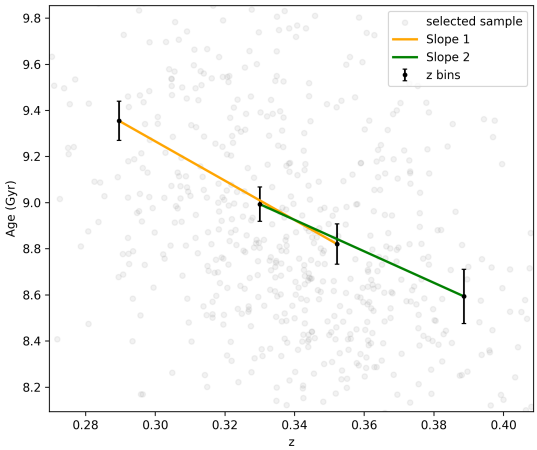

(e) FSPS, **Salpeter**, MILES

Figure 4.7: Qualitative comparison of the slopes derived from the age–redshift relations for different SPS models implemented in `Bagpipes`. Colored lines connect the alternating redshift bins used to compute dt, and the parameter investigated for systematic effects is highlighted.

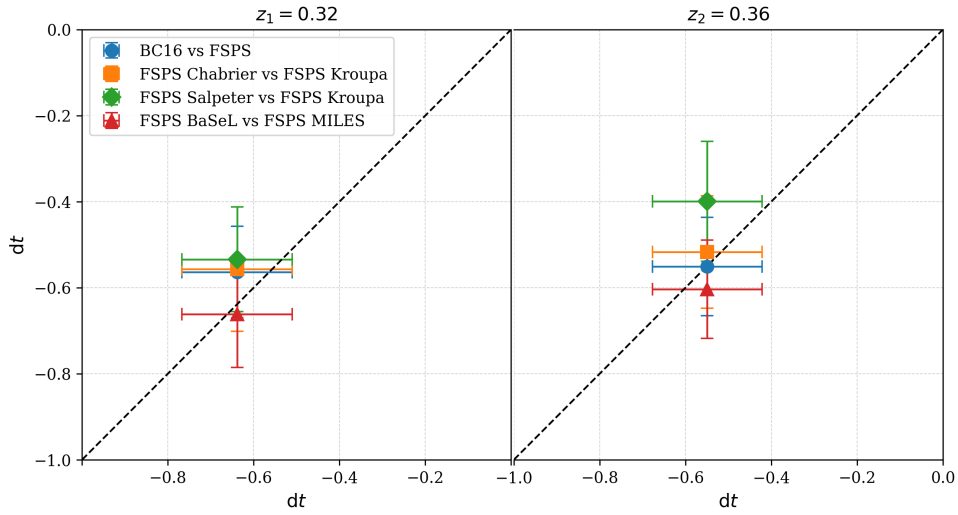

Figure 4.8: Comparison of dt values, in Gyr, for different model combinations, as indicated in the legend. Colors correspond to distinct combinations. *Left*: lower redshift bin ($z_1 = 0.32$). *Right*: higher redshift bin ($z_2 = 0.36$).

To move from a qualitative to a quantitative estimate of the systematics, we define the contribution of each source as the signed difference with respect to the fiducial configuration. Explicitly, the model effect is given by the difference between `FSPS` and `BC16` predictions (using the same IMF and stellar library), the IMF effect by the difference between Chabrier/Salpeter and Kroupa IMFs (within `FSPS+MILES`), and the stellar library effect by the difference between `BaSeL` and `MILES` libraries (within `FSPS`+Kroupa). The resulting average shifts are summarized in Table 4.6. These values represent the typical signed displacement in $H(z)$ that arises when changing one modeling ingredient at a time. The sign of the contribution indicates whether the systematic tends to increase (+) or decrease (−) the recovered value of $H(z)$.

Systematic Source	**Contribution** [$\mathbf{km\,s^{-1}\,Mpc^{-1}}$]
SPS model	−5.38
IMF	+12.6
Stellar library	−4.1

Table 4.6: Systematic contributions to the Hubble parameter estimate arising from different assumptions in SPS modelling, IMF choice, and stellar libraries. Each entry corresponds to the error associated with each systematic considered.

The individual shifts cannot be combined linearly, since they may have opposite signs and originate from independent sources. Therefore, in order to compute the overall systematic uncertainty, we treated each contribution as an independent error term and combine them in quadrature:

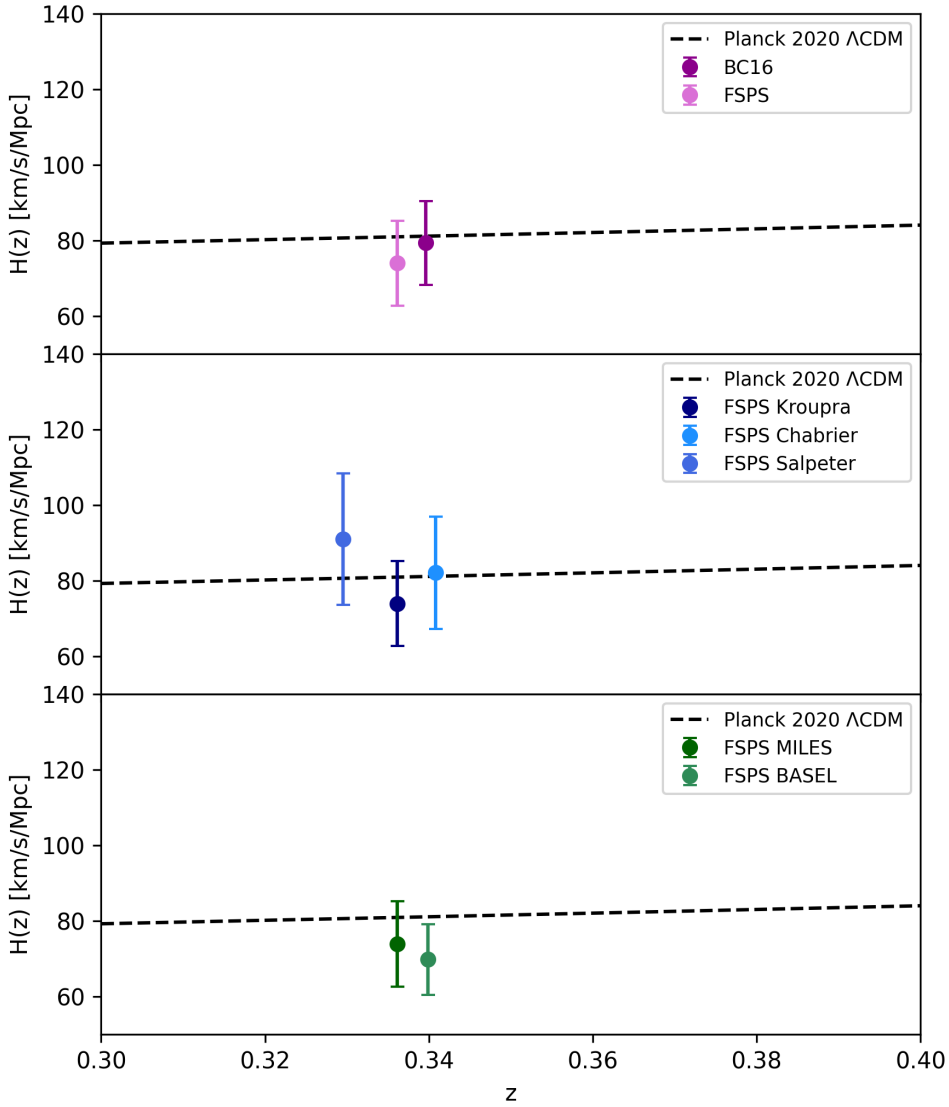

Figure 4.9: Estimates of $H(z)$ obtained from the different configurations reported in Tables 4.2, 4.3 and 4.4, grouped according to the three sources of systematic uncertainty considered in this work.

$$\sigma_{\rm sys} = \sqrt{\delta^2_{\rm SPS} + \delta^2_{\rm IMF} + \delta^2_{\rm lib}}. \tag{4.4}$$

This definition provides the systematic error budget associated with our measurements. However, since the signed contributions carry useful information about the direction of the shift, we also computed asymmetric systematic uncertainties by separately considering positive and negative terms:

$$\sigma^{+}_{\rm sys} = \sqrt{\delta^2_{\rm SPS,+} + \delta^2_{\rm IMF,+} + \delta^2_{\rm lib,+}}, \tag{4.5}$$

$$\sigma^{-}_{\rm sys} = \sqrt{\delta^2_{\rm SPS,-} + \delta^2_{\rm IMF,-} + \delta^2_{\rm lib,-}}, \tag{4.6}$$

where $\delta_{x,+}$ ($\delta_{x,-}$) denotes the positive (negative) component of each contribution. This approach allowed us to preserve information on whether $H(z)$ is systematically overestimated or underestimated under different assumptions. The final result, which includes the systematic uncertainty, is therefore:

$$H(z = 0.34) = 79.3 \pm 11.1\,(\text{stat})^{+12.6}_{-6.8}\,(\text{syst})\ \text{km}\,\text{s}^{-1}\,\text{Mpc}^{-1}.$$

Chapter 5

Conclusions and Future Prospects

In recent years, cosmology has progressed at an extraordinary pace, leading to the development of a widely accepted model, known as ΛCDM, which successfully accounts for most observational constraints (e.g., CMB, SNIa, BAO). Despite these achievements, several open issues remain, motivating further investigation into the nature of the Universe. In particular, one of the central topics of current scientific debate concerns the value of H_0, as measurements of the Hubble constant obtained with different methods yield results that differ at the level of 4-5 σ. Methods based on observations of the CMB radiation, measured with remarkable precision by the *Planck Collaboration* (Aghanim et al., 2020), and those relying on SNIa as standard candles calibrated using Cepheids (Riess et al., 2019), fail to converge on a single consistent value. This discrepancy, known as the *Hubble tension*, represents a major challenge that could lead to a profound revision of the theoretical framework describing the evolution and composition of the Universe, including the role of dark matter and dark energy.

In this context, it is essential to explore new probes beyond the standard ones, as well as to improve and refine innovative techniques that may prove useful in the near future (Moresco et al., 2022). Developing new probes with accuracies comparable to current standard methods is crucial, since combining multiple independent probes enhances the precision of cosmological constraints and helps control systematic uncertainties.

In this thesis, we employed the method of Cosmic Chronometers (Jimenez & Loeb, 2002), which provides a powerful, cosmology-independent approach to constraining the expansion history of the Universe by directly measuring the Hubble parameter through the differential age dating of massive, passive galaxies. However, since this method is still relatively young, applying it efficiently to future surveys (e.g., WST; Bacon et al., 2024) requires a thorough assessment of the systematic effects involved in measuring the expansion rate of the Universe. The study of systematics has so far been primarily focused on methods based on the D4000 index as an age indicator, while it remains limited for one of the most promising approaches, which relies on full spectral fitting. This technique

enables the derivation of differential ages through a statistical approach by combining the available spectroscopic and photometric data, thereby maximizing the information content and helping to break degeneracies between parameters.

In this work, we explored the constraints on cosmological parameters obtained by applying FSF to SDSS BOSS data for the first time, and implemented the possibility of varying models and ingredients within the fit, to achieve a robust and reliable estimation of systematic uncertainties.

The main results of this work are summarized below, following three main stages: (i) the definition of a procedure to select a reliable sample of CC; (ii) the application of FSF techniques to derive age estimates; and (iii) an investigation of the impact of systematic effects.

An optimal sample of Cosmic Chronometers

To apply the CC method, it is crucial to ensure the purity of the sample by combining different selection criteria to minimize contamination from young, star-forming outliers.

- **The selection process**. In this work, we explored and applied a combination of different indicators to minimize potential contamination by star-forming outliers. In particular, we imposed cuts based on $g-i$ color, [OII] λ3727, velocity dispersion, and SNR of the r band. This combined cuts allowed us to maximize the purity of our sample, selecting a final sample of 3,216 CC from the SDSS BOSS surve that spans the range $0.15 < z < 0.5$.

- **Measurement of absorption features and sample characterization**. We measured the Lick indices and other spectral features (Hδ, D4000, CaII H, CaII K, MgII, MgI, Mg b, BL3096, FeI) of the selected galaxies using the Python code `PyLick` (Borghi et al., 2022a), in order to study their evolution with redshift and their dependence on stellar mass. The analysis of these spectral features provided strong evidence of *mass downsizing* (Cowie et al., 1996; Cimatti et al., 2006; Thomas et al., 2010), with more massive galaxies exhibiting stronger age-sensitive indices. Moreover, the decreasing trend of D4000 with redshift represents a clear signature of the progressive aging of the stellar populations with cosmic time, while the absence of spectral features associated with ongoing star formation is consistent with the selection of galaxies that are very massive and passively evolving.

- **Definition of the samples.** We used these results to further refine the sample. In particular, we first selected only those objects belonging to the two highest mass bins and with a SNR > 60, obtaining a sample of 900 CCs. As a further step, we considered only galaxies with the largest D4000 values, known to be an established age indicator, resulting in a golden sample of 84 massive and passive galaxies, ideally

suited for the CC analysis.

Measuring the expansion rate of the Universe in SDSS BOSS

The physical properties of the CC sample (e.g., stellar ages, metallicities, and stellar masses) were reconstructed by performing FSF on combined spectroscopic and photometric data. For this purpose, we employed the public Python code `Bagpipes` (Carnall et al., 2018), which is based on a Bayesian MCMC framework to infer star formation histories and stellar population parameters.

- **Analysis setup.** We carefully explored the dependence of the results on physical parameters (e.g., metallicity, dust reddening, velocity dispersion), as well as on calibration parameters and priors, to assess the robustness of the estimates. A crucial feature of this analysis was that galaxy ages were allowed to extend up to 20 Gyr, independently of redshift, thanks to a modification of the `Bagpipes` code already tested and validated in Jiao et al. (2023) and Tomasetti et al. (2023). The removal of the cosmological prior on ages, commonly adopted in galaxy evolution studies, ensures that the results remain independent of any cosmological model. This allowed us to define a physically motivated set of priors that we applied as a baseline in our analysis. We also developed *ad-hoc* indicators to verify the goodness of our fit and select well-converged results. With this setup, we fitted both our golden sample and the sample of 900 CCs.

- **Derivation of the age–z relations.** From the ages derived through FSF, we obtained a mean age–redshift relation, which forms the basis for the measurement of dt. To evaluate the homogeneity of the sample and optimize the analysis, we investigated several binning configurations as functions of z and σ, confirming the stability and consistency of the resulting measurements. Ultimately, we selected as our final configuration the binning in redshift only, as this choice provides a larger number of galaxies per bin, enhancing the statistical reliability of the mean age estimates and reducing the associated uncertainties.

- **A new measurement of the Hubble parameter.** The data discussed above allowed us to derive a new measurement of the Hubble parameter from the SDSS-BOSS survey with FSF:

$$H(z = 0.34) = 79.3 \pm 11.1 \text{ (stat) km s}^{-1} \text{ Mpc}^{-1}.$$

- **Cosmological constraints** We performed a cosmological analysis with the new datapoint to estimate key parameters of the flat ΛCDM model, specifically the Hubble constant H_0 and the present-day matter density parameter $\Omega_{m,0}$. This was done using a Python-based pipeline employing an MCMC framework to explore

the parameter space and derive posterior distributions. By comparing the results obtained when including all CC measurements available up to 2023 with those obtained with our new estimates (replacing the BOSS $H(z)$ estimate performed with the D4000 approach by Moresco et al. (2016)), we verified that the constraints remain fully consistent, thereby reinforcing the robustness of the CC approach. At the same time, this result highlighted the importance of developing independent techniques for galaxy age-dating, which provide crucial cross-checks and strengthen the reliability of cosmological constraints from CC.

Assessing systematics uncertainties for CC: a new approach

A key goal of this project was to provide, for the first time, a new and detailed assessment of the systematic effects deriving from the differential age measurements in the CC method obtained from FSF. To do that, it was necessary to implement in `Bagpipes` new and different SPS models, to quantitatively assess the impact of stellar model assumptions on age measurements and, hence, on the derived Hubble parameter.

- **Implementation of new models in `Bagpipes`**. We developed a procedure, based on the `FSPS` package (Conroy et al., 2009), to generate new stellar grids to be integrated into `Bagpipes`, varying both the choice of the IMF (Kroupa, Chabrier, Salpeter) and the adopted stellar libraries (`MILES` and `BaSeL`). The stellar models generated with `FSPS` were then encapsulated in a single multi-extension `FITS` file so that `Bagpipes` could properly read the input spectra. This novel framework made it possible to measure the impact of three major sources of systematic uncertainty affecting age dating with FSF: the adoption of different SPS models, IMFs, and the stellar libraries.

- **Quantifying the impact of the different effects**. The same analysis, which applies the CC method to obtain an estimate of $H(z)$, was repeated for all the new configurations, and these values were then compared to quantify the systematic uncertainty associated with each component. We obtained errors on $H(z)$ of: -5.38 (SPS model), $+12.6$ (IMF), and -4.1 (stellar library) $\mathrm{km\,s^{-1}\,Mpc^{-1}}$. These signed contributions were then properly combined in quadrature to determine the final asymmetric systematic uncertainty associated with our $H(z)$ estimate.

- **The final $H(z)$ measurement**. Taking advantage of the high quality and statistical power of the sample and of our new developments, this study enabled a new and robust measurement of the Hubble parameter at redshift $z = 0.34$, while simultaneously addressing one of the key sources of uncertainty currently limiting the CC method:

$$H(z = 0.34) = 79.3^{+16.8}_{-13.0}\,(\mathrm{stat} + \mathrm{syst})\ \mathrm{km\,s^{-1}\,Mpc^{-1}}.$$

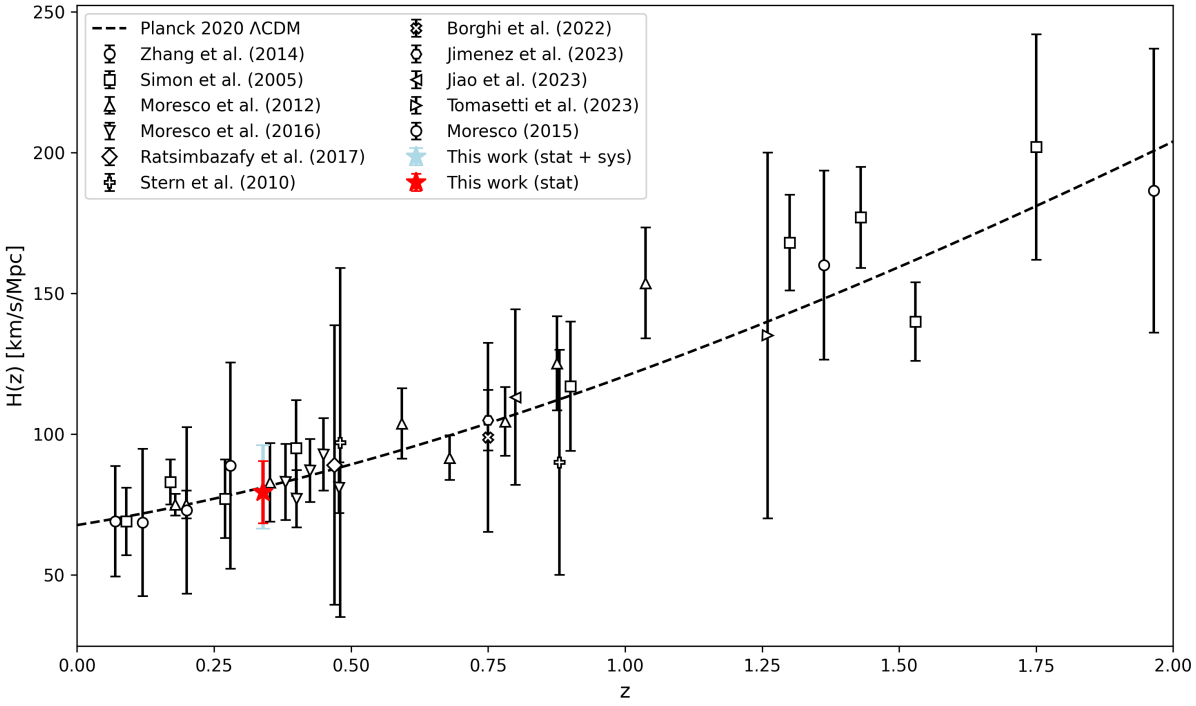

Figure 5.1: Measurements of the Hubble parameter $H(z)$ obtained using the cosmic chronometers method. The red star marks the estimate of $H(z)$ at $z = 0.34$ derived in this work. The light blue bar indicates the corresponding systematic uncertainty.

Figure 5.1 shows our new measurement, highlighting both statistical and systematic contributions to the error, compared with other $H(z)$ obtained in the literature with the CC method.

5.1 Future prospects

This work has yielded promising results in both the study of the physical properties of massive, passive galaxies and in the broader cosmological context. It provided a new estimate of the Hubble parameter while offering a more comprehensive exploration of the systematic uncertainties affecting the method. To this end, the analysis of systematic effects was performed by developing a methodology based on `FSPS`, which enables the construction of customized stellar population libraries in which the key ingredients of the SSP models can be modified and tested. Some possible directions for future work suggested by this study are outlined below.

- A natural continuation of this work will be to implement new stellar population models that account for α-enhancement, such as those presented by Park et al. (2024), as soon as they become available in `FSPS`. These α-MC models self-consistently include non-solar [α/Fe] abundances in both the isochrones and stellar spectra, and are expected to provide a more realistic description of the stellar populations in massive

and passive galaxies, where super-solar α/Fe ratios are commonly observed. Incorporating these models into the analysis would enable a more physically motivated characterization of such galaxies, allowing for a more accurate modeling of their stellar populations and, consequently, more reliable and precise age estimates derived from FSF techniques. This improvement would in turn increase the robustness of the CC method and further mitigate potential systematic uncertainties.

- One of the main limitations of this work was the photometry available for the BOSS galaxies, which proved to be rather limited and not fully consistent with the spectral coverage used in the analysis. A more homogeneous and extended wavelength coverage in the photometric data would therefore allow for better constraints on the stellar population properties and, consequently, improve the robustness of the FSF results. Moreover, in this analysis, we applied the condition of SNR > 10, which restricted the final sample to massive and passive galaxies at $z < 0.5$. Future work could therefore extend this analysis to higher-redshift galaxies.

- Throughout this work, we have emphasized that two main avenues emerge for improving the results obtained from cosmic chronometers. Beyond the uncertainties related to systematics, increasing the statistical sample would further enhance the robustness of the analysis; however, this requires the availability of new and higher-quality spectroscopic data, possibly extending to higher redshifts.
  With this purpose, it will be crucial to improve the sample quality at $z > 0.5$ in order to maximize the accuracy of the measurements across a broad redshift range. In this context, future analyses could take advantage of the upcoming datasets from both *Euclid* (Laureijs et al., 2011) and *James Webb Space Telescope* (JWST) (Gardner et al., 2006), which together offer a unique opportunity to enhance both the quality and the redshift coverage of passive galaxy samples.
  Euclid is designed to probe deeper into the Universe, reaching redshifts up to $z \sim 2$, significantly beyond the typical upper limit of BOSS ($z \leq 0.7$ for most of its galaxy samples). Although the mission is not primarily focused on detailed galaxy spectroscopy, it will extract spectra for all sources with $H < 26$ in the Deep Survey, enabling the detection of continuum features such as D4000 in a large number of massive passive galaxies. Nevertheless, the relatively low spectral resolution of Euclid ($R \sim 250$) may limit its ability to resolve finer spectral features, particularly at higher redshifts. To overcome this limitation, JWST offers an essential complement. With its higher spectral resolution and superior SNR in the infrared, JWST can provide detailed spectroscopic observations of galaxies at $z > 4$, revealing previously unobserved populations of massive and passive galaxies that can be studied in unprecedented detail through its advanced instruments.
  The synergy between Euclid's broad statistical coverage and JWST's high-resolution

spectroscopic capabilities will thus provide a powerful framework for studying the evolution of passive galaxies across cosmic time, improving the precision of cosmic chronometers measurements and refining cosmological constraints at redshifts previously inaccessible.

- Finally, one possibility to extend this project could be the prospect of combining multiple observational approaches, such as galaxy-based chronometers and standard sirens, to improve the accuracy and reliability of cosmological constraints. Indeed, as a rapidly developing field, gravitational waves astronomy holds great promise for the coming years, offering new opportunities to cross-check and enhance traditional measurements of the expansion history of the Universe.

Appendix A

Lick indices

Index	Blue continuum Å	Central band Å	Red continuum Å	Units
Hδ_A	4041.600 – 4079.750	4083.500 – 4122.250	4128.500 – 4161.000	Å
Hδ_F	4057.250 – 4088.500	4091.000 – 4112.250	4114.750 – 4137.250	Å
CN1	4080.125 – 4117.625	4142.125 – 4177.125	4244.125 – 4284.125	mag
CN2	4083.875 – 4096.375	4142.125 – 4177.125	4244.125 – 4284.125	mag
Ca4227	4211.000 – 4219.750	4222.250 – 4234.750	4241.000 – 4251.000	Å
G4300	4266.375 – 4282.625	4281.375 – 4316.375	4318.875 – 4335.125	Å
Hγ_A	4283.500 – 4319.750	4319.750 – 4363.500	4367.250 – 4419.750	Å
Hγ_F	4283.500 – 4319.750	4331.250 – 4352.250	4354.750 – 4384.750	Å
Fe4383	4359.125 – 4370.375	4369.125 – 4420.375	4442.875 – 4455.375	Å
Ca4455	4445.875 – 4454.625	4452.125 – 4474.625	4477.125 – 4492.125	Å
Fe4531	4504.250 – 4514.250	4514.250 – 4559.250	4560.500 – 4579.250	Å
$C_2$4668	4611.500 – 4630.250	4634.000 – 4720.250	4742.750 – 4756.500	Å
Hβ	4827.875 – 4847.875	4847.875 – 4876.625	4876.625 – 4891.625	Å
Fe5015	4946.500 – 4977.750	4977.750 – 5054.000	5054.000 – 5065.250	Å
Mg1	4895.125 – 4957.625	5069.125 – 5134.125	5301.125 – 5366.125	mag
Mg2	4895.125 – 4957.625	5154.125 – 5196.625	5301.125 – 5366.125	mag
Mg b	5142.625 – 5161.375	5160.125 – 5192.625	5191.375 – 5206.375	Å
Fe5270	5233.150 – 5248.150	5245.650 – 5285.650	5285.650 – 5318.150	Å
Fe5335	5304.625 – 5315.875	5312.125 – 5352.125	5353.375 – 5363.375	Å
Fe5406	5376.250 – 5387.500	5387.500 – 5415.000	5415.000 – 5425.000	Å
Fe5709	5672.875 – 5696.625	5696.625 – 5720.375	5722.875 – 5736.625	Å
Fe5782	5765.375 – 5775.375	5776.625 – 5796.625	5797.875 – 5811.625	Å
NaD	5860.625 – 5875.625	5876.875 – 5909.375	5922.125 – 5948.125	Å
TiO1	5816.625 – 5849.125	5936.625 – 5994.125	6038.625 – 6103.625	mag
TiO2	6066.625 – 6141.625	6189.625 – 6272.125	6372.625 – 6415.125	mag

Table A.1: List of the 25 Lick indices as revised by (Trager et al., 1998). For the Balmer indices H$\delta_{A,F}$ and H$\gamma_{A,F}$, the definitions from (Worthey & Ottaviani, 1997) are adopted.

Index	**Blue continuum** Å	**Red continuum** Å	**Reference**
D4000	3750 – 3950	4050 – 4250	(Bruzual A., 1983)
D_n4000	3850 – 3950	4000 – 4100	(Balogh et al., 2004)

Table A.2: Definition of the spectral regions for the D4000 and D_n4000 indices.

Bibliography

Abdalla E., et al., 2022, *Cosmology intertwined: A review of the particle physics, astrophysics, and cosmology associated with the cosmological tensions and anomalies*, Journal of High Energy Astrophysics, 34, 49

Adame A. G., et al., 2025, *DESI 2024 VI: cosmological constraints from the measurements of baryon acoustic oscillations*, J. Cosmology Astropart. Phys., 2025, 021

Aghanim N., et al., 2020, *Planck2018 results: VI. Cosmological parameters*, Astronomy & Astrophysics, 641, A6

Alongi M., Bertelli G., Bressan A., Chiosi C., Fagotto F., Greggio L., Nasi E., 1993, *Evolutionary sequences of stellar models with semiconvection and convective overshoot. I. Z=0.008.*, A&AS, 97, 851

Arnouts S., et al., 2013, *Encoding of the infrared excess in theNUVrKcolor diagram for star-forming galaxies*, Astronomy & Astrophysics, 558, A67

Bacon R., et al., 2024, *WST – Widefield Spectroscopic Telescope: Motivation, science drivers and top-level requirements for a new dedicated facility* (arXiv:2405.12518), https://arxiv.org/abs/2405.12518

Balogh M., et al., 2004, *Galaxy ecology: groups and low-density environments in the SDSS and 2dFGRS*, Monthly Notices of the Royal Astronomical Society, 348, 1355–1372

Benson A. J., 2010, *Galaxy formation theory*, Phys. Rep., 495, 33

Borghi N., Moresco M., Cimatti A., Huchet A., Quai S., Pozzetti L., 2022a, *Toward a Better Understanding of Cosmic Chronometers: Stellar Population Properties of Passive Galaxies at Intermediate Redshift*, ApJ, 927, 164

Borghi N., Moresco M., Cimatti A., 2022b, *Toward a Better Understanding of Cosmic Chronometers: A New Measurement of H(z) at $z \sim 0.7$*, The Astrophysical Journal Letters, 928, L4

Bressan A., Fagotto F., Bertelli G., Chiosi C., 1993, *Evolutionary Sequences of Stellar Models with New Radiative Opacities. II. $Z = 0.02$*, A&AS, 100, 647

Bressan A., Marigo P., Girardi L., Salasnich B., Dal Cero C., Rubele S., Nanni A., 2012, *PARSEC: stellar tracks and isochrones with the PAdova and TRieste Stellar Evolution Code*, MNRAS, 427, 127

Bruzual G., Charlot S., 2003, *Stellar population synthesis at the resolution of 2003*, MNRAS, 344, 1000

Bruzual A. G., 1983, *Spectral evolution of galaxies. I. Early-type systems.*, ApJ, 273, 105

Burstein D., Faber S. M., Gaskell C. M., Krumm N., 1984, *Old stellar populations. I. A spectroscopic comparison of galactic globular clusters, M 31 globular clusters, and elliptical galaxies.*, ApJ, 287, 586

Calzetti D., Armus L., Bohlin R. C., Kinney A. L., Koornneef J., Storchi-Bergmann T., 2000a, *The Dust Content and Opacity of Actively Star-forming Galaxies*, ApJ, 533, 682

Calzetti D., Armus L., Bohlin R. C., Kinney A. L., Koornneef J., Storchi-Bergmann T., 2000b, *The Dust Content and Opacity of Actively Star-forming Galaxies*, ApJ, 533, 682

Cappellari M., 2016, *Improving the full spectrum fitting method: accurate convolution with Gauss–Hermite functions*, Monthly Notices of the Royal Astronomical Society, 466, 798–811

Cardelli J. A., Clayton G. C., Mathis J. S., 1989, *The Relationship between Infrared, Optical, and Ultraviolet Extinction*, ApJ, 345, 245

Cardiel N., 2010, *indexf: Line-strength Indices in Fully Calibrated FITS Spectra*, Astrophysics Source Code Library, record ascl:1010.046

Carnall A. C., McLure R. J., Dunlop J. S., Davé R., 2018, *Inferring the star formation histories of massive quiescent galaxies with bagpipes: evidence for multiple quenching mechanisms*, Monthly Notices of the Royal Astronomical Society, 480, 4379–4401

Carnall A. C., et al., 2019, *The VANDELS survey: the star-formation histories of massive quiescent galaxies at 1.0¡=z¡=1.3*, Monthly Notices of the Royal Astronomical Society, 490, 417–439

Carson D. P., Nichol R. C., 2010, *The age-redshift relation for luminous red galaxies in the Sloan Digital Sky Survey*, MNRAS, 408, 213

Chabrier G., 2003, *Galactic Stellar and Substellar Initial Mass Function*, PASP, 115, 763

Charlot S., Fall S. M., 2000, *A Simple Model for the Absorption of Starlight by Dust in Galaxies*, The Astrophysical Journal, 539, 718–731

Charlot S., Longhetti M., 2001, *Nebular emission from star-forming galaxies*, MNRAS, 323, 887

Chavez M., Bertone E., Buzzoni A., Franchini M., Malagnini M. L., Morossi C., Rodriguez-Merino L. H., 2007, *Synthetic Mid-UV Spectroscopic Indices of Stars*, The Astrophysical Journal, 657, 1046–1057

Chevallard J., Charlot S., 2016, *Modelling and interpreting spectral energy distributions of galaxies with beagle*, Monthly Notices of the Royal Astronomical Society, 462, 1415–1443

Choi J., Conroy C., Moustakas J., Graves G. J., Holden B. P., Brodwin M., Brown M. J. I., van Dokkum P. G., 2014, *The Assembly Histories of Quiescent Galaxies since z = 0.7 from Absorption Line Spectroscopy*, ApJ, 792, 95

Choi J., Dotter A., Conroy C., Cantiello M., Paxton B., Johnson B. D., 2016, *Mesa Isochrones and Stellar Tracks (MIST). I. Solar-scaled Models*, ApJ, 823, 102

Cid Fernandes R., Mateus A., Sodré L., Stasińska G., Gomes J. M., 2005, *Semi-empirical analysis of Sloan Digital Sky Survey galaxies - I. Spectral synthesis method*, MNRAS, 358, 363

Ciddor P. E., 1996, *Refractive index of air: new equations for the visible and near infrared*, Appl. Opt., 35, 1566

Cimatti A., Daddi E., Renzini A., 2006, *Mass downsizing and "top-down" assembly of early-type galaxies*, Astronomy & Astrophysics, 453, L29–L33

Cimatti A., Fraternali F., Nipoti C., 2019, *Introduction to Galaxy Formation and Evolution. From Primordial Gas to Present-Day Galaxies* (arXiv:1912.06216), https://arxiv.org/abs/1912.06216

Citro A., Pozzetti L., Quai S., Moresco M., Vallini L., Cimatti A., 2017, *A methodology to select galaxies just after the quenching of star formation*, Monthly Notices of the Royal Astronomical Society, 469, 3108–3124

Conroy C., 2013, *Modeling the Panchromatic Spectral Energy Distributions of Galaxies*, ARA&A, 51, 393

Conroy C., Gunn J. E., 2010, *The FSPS: Flexible Stellar Population Synthesis Code*, Astrophysics Source Code Library

Conroy C., Gunn J. E., White M., 2009, *The Propagation of Uncertainties in Stellar Population Synthesis Modeling. I. The Relevance of Uncertain Stellar Evolutionary Phases*, The Astrophysical Journal, 699, 486

Cowie L. L., Songaila A., Hu E. M., Cohen J. G., 1996, *New Insight on Galaxy Formation and Evolution From Keck Spectroscopy of the Hawaii Deep Fields*, AJ, 112, 839

Daddi E., et al., 2005, *Passively Evolving Early-Type Galaxies at 1.4 ¡˜z ¡˜2.5 in the Hubble Ultra Deep Field*, ApJ, 626, 680

Eldridge J. J., Stanway E. R., Xiao L., McClelland L. A. S., Taylor G., Ng M., Greis S. M. L., Bray J. C., 2017, *Binary Population and Spectral Synthesis Version 2.1: Construction, Observational Verification, and New Results*, Publications of the Astronomical Society of Australia, 34

Estrada-Carpenter V., et al., 2019, *CLEAR. I. Ages and Metallicities of Quiescent Galaxies at 1.0¡=z¡=1.8 Derived from Deep Hubble Space Telescope Grism Data*, The Astrophysical Journal, 870, 133

Faber S. M., 1973, *Variations in Spectral-Energy Distributions and Absorption-Line Strengths among Elliptical Galaxies*, ApJ, 179, 731

Fagotto F., Bressan A., Bertelli G., Chiosi C., 1994, *Evolutionary sequences of stellar models with new radiative opacities. III. Z=0.0004 and Z=0.05*, A&AS, 104, 365

Falcón-Barroso J., Sánchez-Blázquez P., Vazdekis A., Ricciardelli E., Cardiel N., Cenarro A. J., Gorgas J., Peletier R. F., 2011a, *An updated MILES stellar library and stellar population models*, A&A, 532, A95

Falcón-Barroso J., Sánchez-Blázquez P., Vazdekis A., Ricciardelli E., Cardiel N., Cenarro A. J., Gorgas J., Peletier R. F., 2011b, *An updated MILES stellar library and stellar population models*, A&A, 532, A95

Ferreras I., Charlot S., Silk J., 1999, *The Age and Metallicity Range of Early-Type Galaxies in Clusters*, ApJ, 521, 81

Foreman-Mackey D., Hogg D. W., Lang D., Goodman J., 2013, *emcee: The MCMC Hammer*, PASP, 125, 306

Fukugita M., Ichikawa T., Gunn J. E., Doi M., Shimasaku K., Schneider D. P., 1996, *The Sloan Digital Sky Survey Photometric System*, AJ, 111, 1748

Gallazzi A., Charlot S., Brinchmann J., White S. D. M., Tremonti C. A., 2005, *The ages and metallicities of galaxies in the local universe*, MNRAS, 362, 41

Gardner J. P., et al., 2006, *The James Webb Space Telescope*, Space Sci. Rev., 123, 485

Gavazzi G., Bonfanti C., Sanvito G., Boselli A., Scodeggio M., 2002, *Spectrophotometry of Galaxies in the Virgo Cluster. I. The Star Formation History*, ApJ, 576, 135

Girardi L., Bressan A., Bertelli G., Chiosi C., 2000, *Evolutionary tracks and isochrones for low- and intermediate-mass stars: From 0.15 to 7 M_{sun}, and from Z=0.0004 to 0.03*, A&AS, 141, 371

Heavens A. F., Jimenez R., Lahav O., 2000, *Massive lossless data compression and multiple parameter estimation from galaxy spectra*, Monthly Notices of the Royal Astronomical Society, 317, 965–972

Heavens A., Panter B., Jimenez R., Dunlop J., 2004, *The star-formation history of the Universe from the stellar populations of nearby galaxies*, Nature, 428, 625–627

Hubble E., 1929, *A Relation between Distance and Radial Velocity among Extra-Galactic Nebulae*, Proceedings of the National Academy of Science, 15, 168

Ilbert O., et al., 2013, *Mass assembly in quiescent and star-forming galaxies since z 4 from UltraVISTA*, Astronomy & Astrophysics, 556, A55

Iyer K. G., Pacifici C., Calistro-Rivera G., Lovell C. C., 2025, *The Spectral Energy Distributions of Galaxies* (arXiv:2502.17680), https://arxiv.org/abs/2502.17680

Jiao K., Borghi N., Moresco M., Zhang T.-J., 2023, *New Observational H(z) Data from Full-spectrum Fitting of Cosmic Chronometers in the LEGA-C Survey*, The Astrophysical Journal Supplement Series, 265, 48

Jimenez R., Loeb A., 2002, *Constraining Cosmological Parameters Based on Relative Galaxy Ages*, ApJ, 573, 37

Kennicutt R. C., 1998, *STAR FORMATION IN GALAXIES ALONG THE HUBBLE SEQUENCE*, Annual Review of Astronomy and Astrophysics, 36, 189–231

Koleva M., Prugniel P., Bouchard A., Wu Y., 2009, *ULySS: a full spectrum fitting package*, Astronomy & Astrophysics, 501, 1269–1279

Kroupa P., 2001, *On the variation of the initial mass function*, MNRAS, 322, 231

Lançon A., Mouhcine M., 2002, *The modelling of intermediate-age stellar populations. II. Average spectra for upper AGB stars, and their use*, A&A, 393, 167

Laureijs R., et al., 2011, *Euclid Definition Study Report* (arXiv:1110.3193)

Le Borgne J. F., et al., 2003, *STELIB: A library of stellar spectra at R ~2000*, A&A, 402, 433

Le Cras C., Maraston C., Thomas D., York D. G., 2016, *Modelling the UV spectrum of SDSS-III/BOSS galaxies: hints towards the detection of the UV upturn at high-z*, Monthly Notices of the Royal Astronomical Society, 461, 766–793

Lee H., Worthey G., 2005, *-Enhanced Integrated Lick/IDS Spectral Indices and Milky Way and M31 Globular Clusters and Early-Type Galaxies*, The Astrophysical Journal Supplement Series, 160, 176–198

Lejeune T., Cuisinier F., Buser R., 1998, *A standard stellar library for evolutionary synthesis. II. The M dwarf extension*, A&AS, 130, 65

Lemaître G., 1927, *Un Univers homogène de masse constante et de rayon croissant rendant compte de la vitesse radiale des nébuleuses extra-galactiques*, Annales de la Société Scientifique de Bruxelles, 47, 49

Magris C. G., Binette L., Bruzual A. G., 2003, *ADEMIS: A Library of Evolutionary Models for Emission-Line Galaxies. I. Dust-free Models*, The Astrophysical Journal Supplement Series, 149, 313–326

Maraston C., Strömbäck G., 2011, *Stellar population models at high spectral resolution*, MNRAS, 418, 2785

Maraston C., Nieves Colmenárez L., Bender R., Thomas D., 2008, *Absorption line indices in theUV: I. Empirical and theoretical stellar population models*, Astronomy & Astrophysics, 493, 425–444

Masters K. L., et al., 2011, *The morphology of galaxies in the Baryon Oscillation Spectroscopic Survey*, MNRAS, 418, 1055

McDermid R. M., et al., 2015, *The ATLAS3D Project – XXX. Star formation histories and stellar population scaling relations of early-type galaxies*, Monthly Notices of the Royal Astronomical Society, 448, 3484–3513

Mignoli M., et al., 2009, *The zCOSMOS redshift survey: the three-dimensional classification cube and bimodality in galaxy physical properties*, A&A, 493, 39

Moresco M., 2024, *Measuring the expansion history of the Universe with cosmic chronometers*, arXiv e-prints, p. arXiv:2412.01994

Moresco M., Jimenez R., Cimatti A., Pozzetti L., 2011, *Constraining the expansion rate of the Universe using low-redshift ellipticals as cosmic chronometers*, Journal of Cosmology and Astroparticle Physics, 2011, 045–045

Moresco M., et al., 2012, *Improved constraints on the expansion rate of the Universe up to z 1.1 from the spectroscopic evolution of cosmic chronometers*, Journal of Cosmology and Astroparticle Physics, 2012, 006–006

Moresco M., et al., 2013, *Spot the difference. Impact of different selection criteria on observed properties of passive galaxies in zCOSMOS-20k sample*, A&A, 558, A61

Moresco M., et al., 2016, *A 6*

Moresco M., Jimenez R., Verde L., Pozzetti L., Cimatti A., Citro A., 2018, Setting the Stage for Cosmic Chronometers. I. Assessing the Impact of Young Stellar Populations on Hubble Parameter Measurements*, The Astrophysical Journal, 868, 84*

Moresco M., Jimenez R., Verde L., Cimatti A., Pozzetti L., 2020, Setting the Stage for Cosmic Chronometers. II. Impact of Stellar Population Synthesis Models Systematics and Full Covariance Matrix*, The Astrophysical Journal, 898, 82*

Moresco M., et al., 2022, Unveiling the Universe with emerging cosmological probes*, Living Reviews in Relativity, 25, 6*

Oser L., Ostriker J. P., Naab T., Johansson P. H., Burkert A., 2010, THE TWO PHASES OF GALAXY FORMATION*, The Astrophysical Journal, 725, 2312–2323*

Pacifici C., et al., 2016, THE EVOLUTION OF STAR FORMATION HISTORIES OF QUIESCENT GALAXIES*, The Astrophysical Journal, 832, 79*

Park M., Conroy C., Johnson B. D., Leja J., Dotter A., Cargile P. A., 2024, α-MC: Self-consistent α-enhanced stellar population models covering a wide range of age, metallicity, and wavelength*, arXiv e-prints, p. arXiv:2410.21375*

Perlmutter S., et al., 1999, Measurements of and from 42 High-Redshift Supernovae*, The Astrophysical Journal, 517, 565–586*

Pietrinferni A., Cassisi S., Salaris M., Percival S., Ferguson J. W., 2009, A LARGE STELLAR EVOLUTION DATABASE FOR POPULATION SYNTHESIS STUDIES. V. STELLAR MODELS AND ISOCHRONES WITH CNONa ABUNDANCE ANTI-CORRELATIONS*, The Astrophysical Journal, 697, 275–282*

Ratsimbazafy A. L., Loubser S. I., Crawford S. M., Cress C. M., Bassett B. A., Nichol R. C., Väisänen P., 2017, Age-dating luminous red galaxies observed with the Southern African Large Telescope*,* MNRAS*, 467, 3239*

Riess A. G., et al., 1998, Observational Evidence from Supernovae for an Accelerating Universe and a Cosmological Constant*,* AJ*, 116, 1009*

Riess A. G., Casertano S., Yuan W., Macri L. M., Scolnic D., 2019, Large Magellanic Cloud Cepheid Standards Provide a 1

Salpeter E. E., 1955, *The Luminosity Function and Stellar Evolution.*, ApJ, 121, 161

Sanchez-Blazquez P., et al., 2006, *Medium-resolution Isaac Newton Telescope library of empirical spectra*, Monthly Notices of the Royal Astronomical Society, 371, 703–718

Scalo J. M., 1986, *The Stellar Initial Mass Function*, Fund. Cosmic Phys., 11, 1

Schlegel D., White M., Eisenstein D., 2009, *The Baryon Oscillation Spectroscopic Survey: Precision measurements of the absolute cosmic distance scale* (arXiv:0902.4680), https://arxiv.org/abs/0902.4680

Sersic J. L., 1968, *Atlas de Galaxias Australes*

Stoughton C., et al., 2002, *Sloan Digital Sky Survey: Early Data Release*, AJ, 123, 485

Thomas D., Maraston C., Korn A., 2004, *Higher-order Balmer line indices in α/Fe-enhanced stellar population models*, MNRAS, 351, L19

Thomas D., Maraston C., Schawinski K., Sarzi M., Silk J., 2010, *Environment and self-regulation in galaxy formation*, MNRAS, 404, 1775

Thomas D., Maraston C., Johansson J., 2011, *Flux-calibrated stellar population models of Lick absorption-line indices with variable element abundance ratios*, MNRAS, 412, 2183

Tojeiro R., Heavens A. F., Jimenez R., Panter B., 2007, *Recovering galaxy star formation and metallicity histories from spectra using VESPA: Recovering galaxy histories using VESPA*, Monthly Notices of the Royal Astronomical Society, 381, 1252–1266

Tomasetti E., et al., 2023, *A new measurement of the expansion history of the Universe at $z = 1.26$ with cosmic chronometers in VANDELS*, A&A, 679, A96

Trager S. C., Worthey G., Faber S. M., Burstein D., Gonzalez J. J., 1998, *Old Stellar Populations. VI. Absorption-Line Spectra of Galaxy Nuclei and Globular Clusters*, The Astrophysical Journal Supplement Series, 116, 1–28

Tripicco M. J., Bell R. A., 1995, *Modeling the LICK/IDS Spectral Feature Indices Using Synthetic Spectra*, AJ, 110, 3035

Verde L., Treu T., Riess A. G., 2019, *Tensions between the early and late Universe*, Nature Astronomy, 3, 891–895

Westera P., Lejeune T., Buser R., Cuisinier F., Bruzual G., 2002, *A standard stellar library for evolutionary synthesis. III. Metallicity calibration*, A&A, 381, 524

Wilkinson D. M., Maraston C., Goddard D., Thomas D., Parikh T., 2017, *firefly (Fitting IteRativEly For Likelihood analYsis): a full spectral fitting code*, Monthly Notices of the Royal Astronomical Society, 472, 4297–4326

Williams R. J., Quadri R. F., Franx M., van Dokkum P., Labbé I., 2009, *DETECTION OF QUIESCENT GALAXIES IN A BICOLOR SEQUENCE FROMZ= 0-2*, The Astrophysical Journal, 691, 1879–1895

Worthey G., 1994, *Comprehensive Stellar Population Models and the Disentanglement of Age and Metallicity Effects*, ApJS, 95, 107

Worthey G., Ottaviani D. L., 1997, *H and H Absorption Features in Stars and Stellar Populations*, The Astrophysical Journal Supplement Series, 111, 377

York D. G., et al., 2000, *The Sloan Digital Sky Survey: Technical Summary*, AJ, 120, 1579

de Graaff A., et al., 2025, *Efficient formation of a massive quiescent galaxy at redshift 4.9*, Nature Astronomy, 9, 280

van Dokkum P. G., Franx M., Fabricant D., Illingworth G. D., Kelson D. D., 2000, *Hubble Space TelescopePhotometry and Keck Spectroscopy of the Rich Cluster MS 105403: Morphologies, Butcher-Oemler Effect, and the Color-Magnitude Relation atz= 0.83*, The Astrophysical Journal, 541, 95–111